ABSTRACT

Title of Document: METHODS AND MODELS FOR ASSESSING SOLDER INTERCONNECT RELIABILITY OF CONTROL BOARDS IN POWER ELECTRONIC SYSTEMS

David William Squiller, Master of Science, 2013

Directed By: Associate Professor F. Patrick McCluskey
Department of Mechanical Engineering

Over the past 20 years, power electronic systems have been increasingly required to operate in harsh environments including automotive, deep-well drilling and aerospace applications. In parallel, the higher power densities and miniaturization of the power switching module result in elevated stress levels on the control circuitry. The objective of this study was to develop methods and models for assessing the interconnect reliability of components used in the control circuitry for power electronic systems. Physics-of-Failure modeling and a series of thermal and reliability simulations were conducted on a 2.2 kW variable-frequency drive to evaluate the susceptibility of system level and component level failure mechanisms. Assessment methods consisted of developing CalcePWA simulation models of the primary subassemblies and constructing a power cycling apparatus to perform accelerated testing of the drive.

METHODS AND MODELS FOR ASSESSING SOLDER INTERCONNECT RELIABILITY OF CONTROL BOARDS IN POWER ELECTRONIC SYSTEMS

By

David William Squiller

Thesis submitted to the Faculty of the Graduate School of the
University of Maryland, College Park, in partial fulfillment
of the requirements for the degree of
Master of Science
2013

Advisory Committee:
Dr. F. Patrick McCluskey, Chair, Associate Professor of Mechanical Engineering
Dr. Michael Pecht, Professor of Mechanical Engineering & Director of CALCE
Dr. Bongtae Han, Professor of Mechanical Engineering & Leader of EPS Division

Dedication

To my family, friends and all those who have supported me.

Acknowledgements

This project experienced many highs and lows and without the help of numerous individuals “Ashes, Burned and Broken” would be the title of this thesis.

I would first like to thank Dr. McCluskey for accepting me into his research group and providing me the exciting opportunity to learn from my mistakes. Without your patience, understanding and mentorship, I would still be lost in a sea of confusion. I very much look forward to the next (hopefully) three years working under your direction.

I would also like to thank Hannes, Ali, Sumeer, Chandra and the rest of Dr. McCluskey’s research team. Your feedback was integral throughout this project and the office laughter provided much needed comic relief during this time. I would like to especially thank Hannes for breaking down power electronics, induction motors and three-phase electricity. Your “back-of-the-envelope” diagrams served me well and I wish you the best of luck with your future in academia.

Finally, I would like to acknowledge my loving family and friends who were my backbone during this project. Without your support, none of this would be possible.

Table of Contents

Table of Figures

Table of Tables

Chapter 1: Introduction

The study of power electronics is concerned with controlling and converting electrical energy. Power is typically generated and transmitted at a fixed frequency and arrives to the load at a fixed voltage. However, the load often times operates under different power levels or frequencies, thus precise control and conversion of the incoming power is imperative to meet specific application requirements [1].

Operated under the guidance of control circuitry, a matrix of power semiconductor switching devices resides at the core of any power electronic system [1]. The types of power electronic systems can be classified according to their function which include rectifiers (AC-to-DC), choppers (DC-to-DC), inverters (DC-to-AC), AC power controllers (constant frequency) and cycloconverters (AC frequency converter), but most power conversion systems utilize more than one type [1]. The control hardware processes information from the source, load and application to determine how the switches should operate in order to achieve the desired power conversion [2]. These control circuits are typically constructed using low-power analog and digital elements and operate under significantly less power than the power converter. Figure 1 depicts the basic elements of a power electronic system, wherein the power electronic circuit may contain subsystems other than the semiconductor switching module such as magnetic transformers, capacitors and inductors [3].

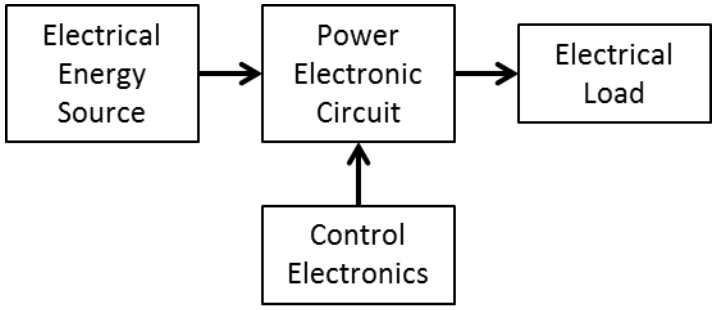

Figure 1 Elements of a basic power electronic system [3]

The past three decades have been characterized by numerous improvements of these systems with respect to size, weight, performance and reliability allowing extensive growth in applications involving industrial, commercial, residential, aerospace, military, utility, and transportation environments [4]. The gamut of applications involving power electronics is wide, and Figure 2 shows some of the key areas.

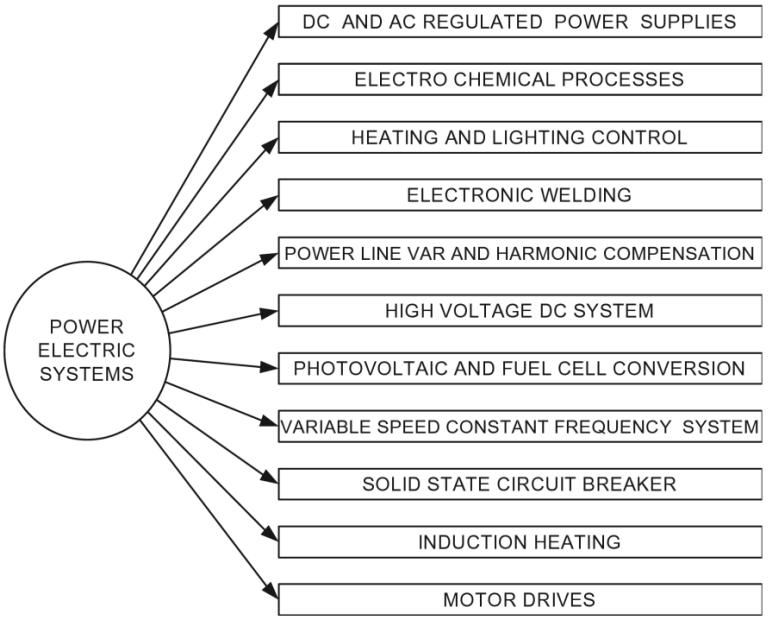

Figure 2 Spectrum of applications involving power electronics [4]

As power electronic systems spread into these various application fields, much attention has been directed towards reliability. Due to the fact that most power electronic systems are not equipped with redundancy mechanisms [5] any fault that occurs in any one

subsystem may lead to a catastrophic system shutdown. Not only could this present significant safety concerns in mission-critical applications, but system operation costs would increase as well. One of the primary benefits of using power electronic converters is for their high-efficiency switching mechanism [2]. If much time is spent repairing systems and replacing faulty components, the benefits of using power electronic converters would be redundant. For example, in a photovoltaic energy generation system, the cost of inverter related failure is equal to the cost of replacing and repairing parts plus the cost of the wasted energy that would be generated during the system down time [5][6]. This fact is not limited to photovoltaic systems, but also applies to other applications such as wind energy conversion systems. According to the U.S. Department of Energy, a major roadblock in achieving 20% wind power generation by 2030 depends upon the improved reliability and operation of the power electronics within the wind energy conversion system [7].

1.1 Variable Frequency Drives

Variable frequency drives (VFDs) are electronic controllers typically used in electromechanical drive systems to control the speed of electric motors through modulating incoming power. The conversion of incoming power may take place in the form of adjusting the voltage or the frequency [8]. Power electronic converters, along with their respective control circuits and energy storage subsystems, are at the heart of all VFDs due to the necessary power conversion process that must take place. Prior to the implementation of VFDs in electromechanical drive systems, motors were typically powered by fixed AC lines and controlled through a complex series of belts and pulleys

[9]. A typical motor drive system, shown in Figure 3 contains a power source, a power electronic converter, a transmission mechanism, a load, and various types of control systems.

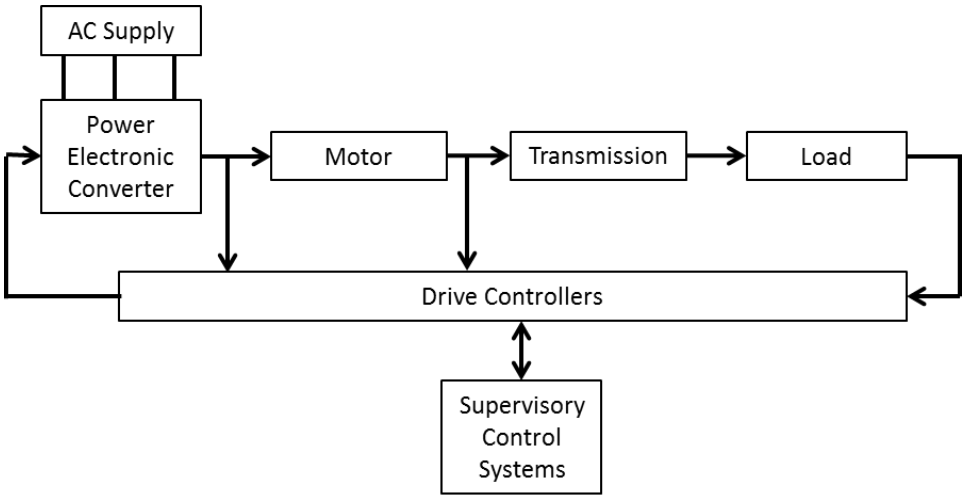

Figure 3 Typical electromechanical drive system [2]

The AC supply is connected directly to the power electronic converter which contains the fundamental semiconductor switching elements and a variety of passive energy storage components. The drive controllers may be integrated into the power electronic converter, as seen with recent trends in power electronic system packaging [10], or may function autonomously and interact with other system level controllers. The ranges of power, speed and torque of AC induction motors vary heavily depending upon the load and application. For example, high-power motor drives (usually on the order of multi-megawatts) are required if the application involves a ship propulsion system or rolling mills [4]. Medium-range motor drives, those whose power requirements fall within a few kilowatts to a couple megawatts, are seen in applications involving transportation, wind generation, pumps and starter-generators [4]. Computer and residential applications typically require low-power motor drives, those whose power requirements are less than

a couple hundred watts [4]. While the fundamental components and subsystems of VFDs are seen across all power ranges, the rest of this section will investigate the power converter and ancillary subsystems within a three-phase 2.2 kW motor drive.

1.1.1 ACS355 Variable Frequency Drive

The VFD model used in this study is an ACS355-03E-05A6-4 manufactured by ABB. Table 1 depicts the general specifications of the drive, while Figure 4 Top and side view of the motor drivedisplays the top and side views of the drive.

Table 1 ABB ACS355-03E-05A6-4 specifications

Nominal Power	2.2 kW (3 HP)
Input Voltage (U1)	3~ 380…480 VAC
Input Current (I1)	9.6 A
Input Frequency (f1)	48…63 Hz
Output Voltage (U2)	3~ 0…U1
Output Current (I2)	5.6 A (150% for 6 seconds)
Output Frequency (f2)	0…600 Hz

Figure 4 Top and side view of the motor drive

Located at the front of the drive are the various ports, shown in Figure 5, for connecting the motor, the AC power source, the control cables and the braking resistor. There exist three methods for controlling the motor drive: using analog and digital signals, using

external devices via embedded fieldbus or fieldbus adapter, or through a control panel that also allows for USB connection to a computer. For this project, only the last method was used.

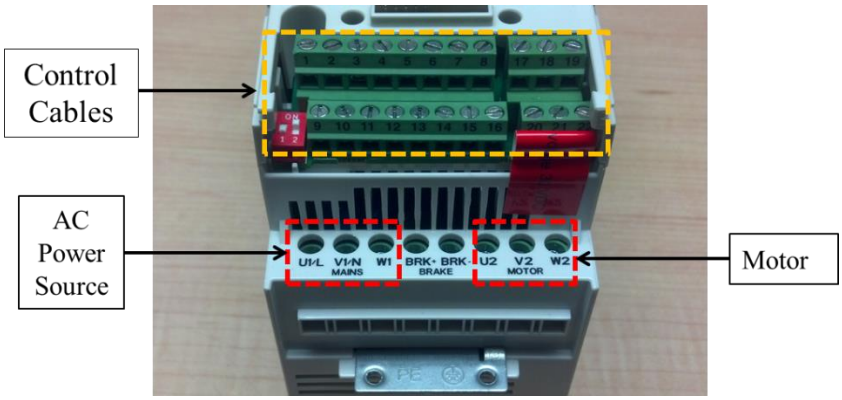

Figure 5 Ports for connecting motor, AC power source, control cables and braking resistor

Referred to as local control (as opposed to remote control which involves the external devices and fieldbus adapters) the control panel provides a means for the user to operate the drive. Specifically, the user is able to set the frequency at which the motor is to be run and monitor various parameters such as current, torque from the load, DC bus voltage and power output. Figure 6 shows both the control panel and USB port used to interface with the motor drive.

Figure 6 User interface - USB (left), control panel (right)

Once connected to the computer the drive can be monitored and operated through DriveWindow Light, a software tool developed by ABB. This program allows the user to monitor and record input and output signals, operate the drive from a PC or network, provide an avenue for PID control and allow the user to create and edit custom sequence programs.

1.1.2 Control Board

One of the major subsystems in the motor drive is the control board. This board contains the primary gate-driver components that direct the operation of the power switching module. Located just underneath the top casing of the motor drive, this assembly houses the brains of the power electronics system. Figure 7 shows the top and bottom views of the board along with the orientation within the motor drive.

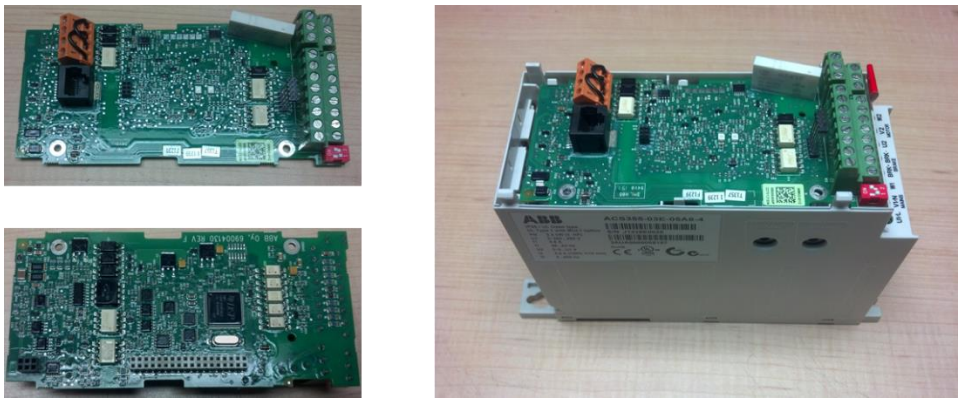

Figure 7 Control board - top side (upper right), bottom side (lower left)

The primary function of this subsystem is to provide the switches inside the power switching module with signals that control the power conversion process. This board operates under significantly less power than the rest of the board, but contains the largest number of components making it the most complex subsystem within the drive.

1.1.2 Power Switching Module – Diodes and IGBTs

The simplest of all power switching devices is the diode [2]. Comprised of two terminals, one referred to as the anode while the other referred to as the cathode, this device functions as a one way valve for electricity. If the potential at the anode is greater than the potential at the cathode, the switch is in a forward bias allowing current to flow through the switch. However, if the potential at the cathode is greater than the potential at the anode, the device is said to be in reverse bias and does not conduct electricity. However, there does exist a small amount of current, known as leakage current, which continues to flow through. Often times in power electronics applications the leakage current as well as the forward voltage drop are ignored and the diode is treated as an ideal switch [2].

An IGBT is a power semiconductor switch comprised of three terminals used to control electrical energy. Prior to the early 1980's when IGBTs were introduced, metal oxide field effect transistors (MOSFETs) and bipolar junction transistors (BJTs) were the primary switching devices used in high-frequency and low to medium power applications [2]. While BJTs have good on-state conduction characteristics [2], they have long switching times and increased power loss. This is because they are current-controlled devices and require complicated base-drive circuits [2]. Conversely, MOSFETs are voltage-driven devices requiring much simpler gate-drive requirements, allowing the device to operate at much higher switching speeds [2]. However, the major drawbacks of MOSFETs are that as the voltage rating increases, the intrinsic conduction characteristics degrade and higher switching losses occur which generates significant heat [2]. The

IGBT combines the superior on-state conduction characteristics of the BJT with the simple gate-drive requirements of the MOSFET, producing a device with medium-range switching speeds and medium to high-range voltage and current ratings.

In the ACS355 the power switching module is the SKiiP 11NAB065V1 manufactured by Semikron, shown in Figure 8. The module is comprised of a three-phase bridge rectifier, a brake chopper and a three-phase bridge inverter. A combination of IGBTs and diodes [11], also shown in Figure 8, form the matrix of power semiconductor switches.

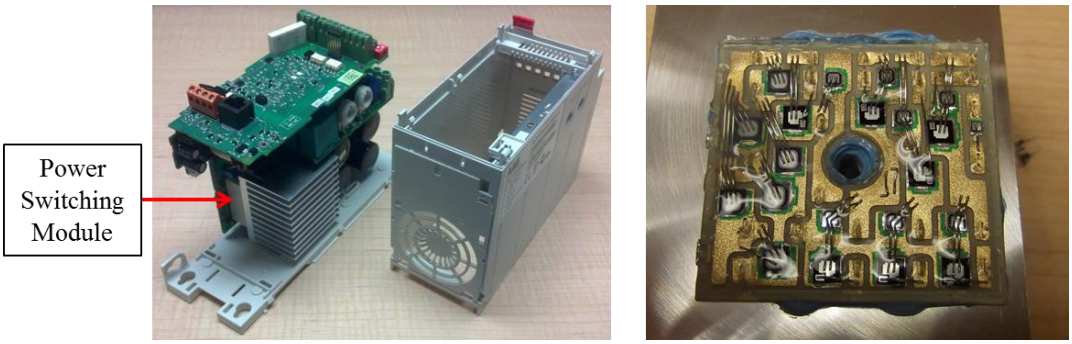

Figure 8 Power switching module (left), IGBTs and diodes within module (right)

While the power switching module is rated for a maximum operating temperature of 150°C and produces a system fault at 135°C, a thermal management system is implemented to maintain the temperatures well below these levels. Also shown in Figure 8 is the heat sink which the power switching module is attached to by means of thermal paste. A fan is also located near the heat sink which transfers warm air inside the system to the ambient at a mass flow rate of 0.0114 kg/s. Although the power switching module generates significant heat, there exist a number of other components that require cooling such as the digital signal processor (DSP) located on the control board, a MOSFET also attached to the heat sink, surface mount technology (SMT) rectifiers, voltage regulators and various SMT passive devices.

1.1.3 Energy Storage Elements

A power electronic system contains various components for energy storage often in the form of electrolytic capacitors, film capacitors, inductors, transformers and chokes. In the ACS355, these elements are divided up among two different printed circuit boards (PCBs). One of the PCBs will be denoted as the "connector board" as it contains the I/O connections for the motor and AC power source while the other PCB will be denoted the "power board" as it houses the power switching module. Figure 9 displays the power board outlined in yellow and the connector board outlined in red.

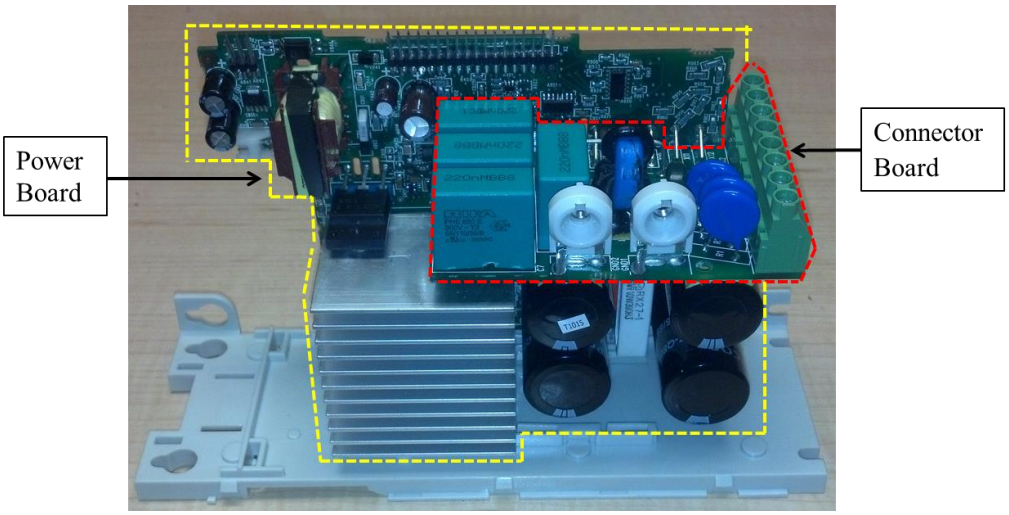

Figure 9 Power board (yellow), connector board (red)

The power board contains four large electrolytic capacitors, four smaller electrolytic capacitors and one transformer all displayed in Figure 10.

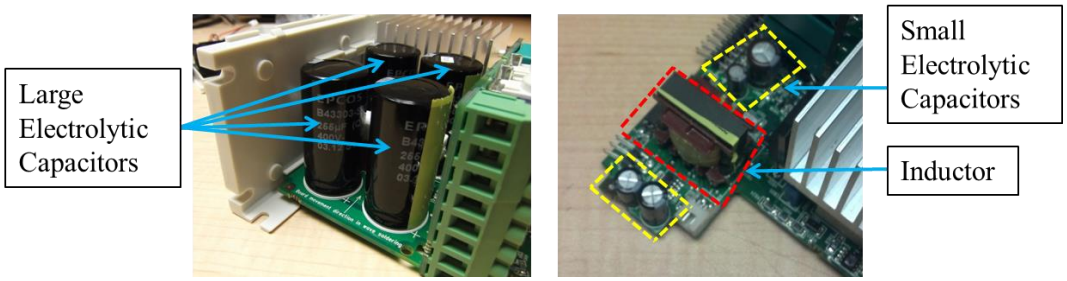

Figure 10 Electrolytic capacitors and transformer on power board

The connector board contains four film capacitors, a choke, a rectifier diode and four metal oxide varistors, all shown in Figure 11.

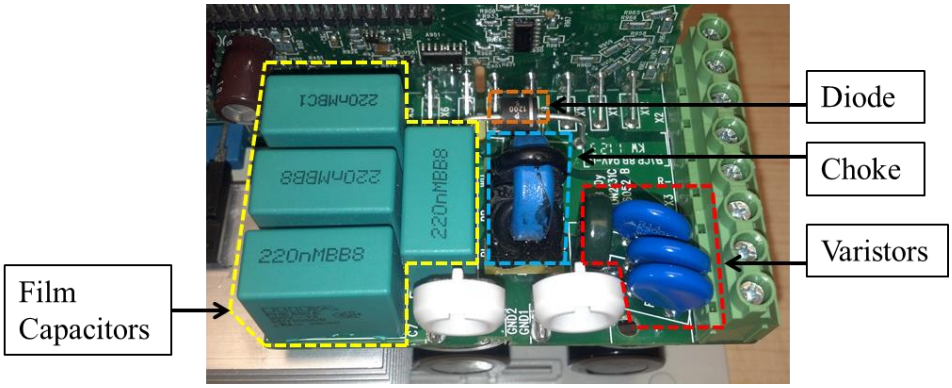

Figure 11 Components on connector board

While the operation of these components is important with regards to power electronic system design, the specific topology of this setup and how each component interacts with one another falls outside the scope of this research project. There exists much literature [1][2][3][4][12] which discusses in detail the electrical engineering theory behind variable frequency drives and power electronic converter topologies.

1.2 Physics-of-Failure (PoF) Approach

Reliability can be defined as the ability of a part or product to perform its intended function, without fail and within operating limits, over a period of time through its life cycle application environment [13]. Traditionally, reliability predictions of electronic parts and systems have been conducted using U.S. military standards (MIL-217 Handbook) which relies on fitting failure data from the field to mathematical curves in order to determine failure rates of individual components. Once these individual component rates are determined, the failure rate of the entire system is computed by adding up all the individual failure rates. However, this method predicting reliability has

inherent faults, such as producing failure rate curves that are independent of component manufacturer and incorrectly assuming that the failure rate of each component is constant over time [14]. For this reason, manufacturers many years ago moved towards the PoF approach [14].

The PoF approach for assessing reliability is founded on the concept that fundamental processes, whether mechanical, electrical, chemical, radiological or thermal, are responsible for the failure of electronic parts and systems. Through identifying these processes and understanding the mechanisms through which they induce failure, specific models can be created which compute various times-to-failure values. The end result is an accurate reliability prediction technique giving engineers the ability to design more reliable products by avoiding known modes of failure [14].

1.3 Research Motivation

Throughout the past decade, there has been a widespread push for developing reliable Silicon Carbide (SiC) and Gallium Nitride (GaN) based devices to improve upon the limitations presented by traditional silicon based switching devices [15]. Wide-bandgap semiconductor devices can operate at temperatures exceeding 500°C, while silicon devices can generally operate at temperatures up to 200°C, with some exceptions. By surpassing the longstanding temperature boundary imposed by silicon devices, power electronics systems are now able to enter into a variety of high-temperature and extreme-environment applications.

For example, in order to reduce the complexity of various systems found in aircrafts, manufacturers are moving towards a “more electric architecture”, which attempts to use only electrical systems [16]. In order to attain sufficient efficiency, power electronic converters should be placed as close as possible to the actuators they control. This may require placing the power electronic systems near the jet engines which may have a temperature range from -55°C to 225°C with multiple temperature cycles per day [16][17].

Another example of power electronic systems entering extreme applications is space exploration. The Venusian atmosphere is highly concentrated with sulfuric acid, while the surface of the planet exhibits temperatures exceeding 460°C with pressures of 92 bars [15]. Although this is a niche application, the same technology could spread into other areas such as the automotive industry and deep oil and gas drilling, where corrosive environments and extreme temperatures exist [16].

While the actual power semiconductor switching devices may be suitable and reliable for these high-temperature and extreme environment applications, the entire power electronic system contains multiple subsystems, all of which must be suitable for the type of application. With smaller and more modular packaging techniques, such as the predicted drive towards integrated power electronics modules (IPEMs) [10][18][19], the control circuitry will experience significant residual heating from the power semiconductor switches. In addition to the extreme environment, the control circuitry will experience

additional heating from the conduction and switching losses that occur at elevated power levels.

This research will focus on developing a PoF-based approach for assessing the reliability of the control circuitry for power electronic systems using the ACS355 variable frequency drive. While the power switching module and other energy storage devices are integral in assessing system reliability, they will not be the focus of this research.

Chapter 2: Literature Review

This section will begin with a survey of previously conducted research pertaining to power electronic system reliability. Three fundamental topics will be covered in this section: research relating to the power switching modules, system-level reliability prediction methods and variable-frequency drive reliability assessment methods. The aim of this study was to develop a reliability assessment method of a particular subsystem. Literature review indicated that the control circuitry is rarely the focus of power electronic system reliability research. Many component-specific studies indicated that other components and subsystem are likely to fail first, usually the power switching module or the electrolytic capacitors [5]. As such, the control circuitry was often times included as an ancillary subsystem in the reviewed reliability assessment methods.

2.1 Power Electronic Modules

A congruency found among power electronic system reliability assessment efforts was that many studies focus on individual component reliability and the respective failure mechanisms of those components. Field observations reveal that the power switching module is most susceptible to failure and thus much interest has been directed towards studying the various failure mechanisms present in these devices [5].

McCluskey discusses the dominant failure mechanisms, specifically those related to interconnects within the module, substrates, die attach and planar interconnects [20]. Figure 12 shows the various building blocks that make up a typical power-switching

module. They consist of silicon dies, direct bond copper substrates, a copper heat-spreader, aluminum wires to electrically connect the dies, solder and die attach [20].

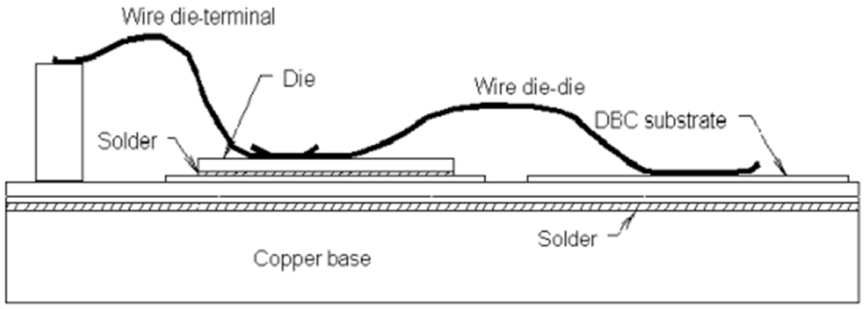

Figure 12 Components of a typical power switching module [20]

Under thermal cycling, significant thermomechanical stress is induced in each component due to the CTE mismatch of adjacent parts. Traditionally, bond wire failure has been the dominant failure mode seen within power modules, shown in Figure 13. Significant research has been conducted to compare the performance of copper to that of the traditionally used aluminum in bond wires [21][22]. These studies have suggested that copper would be more resistant to shear failure due to its higher yield strength. Furthermore, less thermomechanical stress would be induced in the bond wires due to the lower CTE mismatch between the copper and the die. Thus it can be concluded that PoF studies have successfully indicated the most appropriate materials for traditionally unreliable constituents.

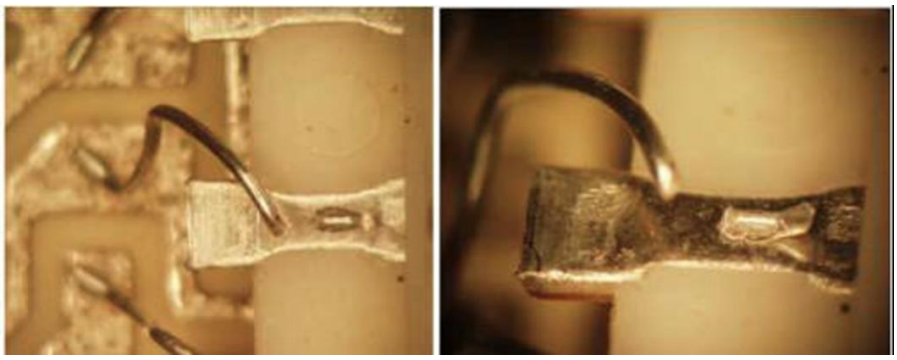

Figure 13 Failures in bond wires [20]

Other studies have been conducted that combine numerical analysis with experimental testing to identify the root cause of failure in power electronic modules. Bailey et. al. [23] uses a PoF approach to predict solder fatigue and wire bond lift off based upon various load applications. A finite element model was created by identifying the geometries and materials of each component. Information regarding the temperature profile experienced at varying load levels provided the necessary information to conduct computer-aided simulations. The analysis was run based upon the life cycle operating conditions. Miner's lifetime accumulation rule was implemented in order to calculate the number of cycles to failure. The result of this study was a relationship between solder thickness and time-to-failure at varying power levels.

In another study, the reliability of an IGBT power electronic module exposed to thermal cycling from -40°C to 120°C with 15 minute ramp times was predicted [24]. Similar to the study conducted by Bailey et. al. [23], a finite element model was created. Four components were analyzed for failure including the busbar, bond wire, chip solder, and substrate solder. Metrics were also established that defined failure criteria. In this study failure in the busbar was defined when 50% of the solder area delaminated, while 20% solder area delamination defined failure in the chip and substrate solder. Lastly, wire bond failure was defined when a 90% reduction in shear strength was observed. The results of this study indicated the number of thermal cycles that would cause each constituent to fail.

2.2 Variable Frequency Drive Reliability

Lorenz explains that “a key dimension for the future of motor drives is to make them reliable, value-added parts of a system [25].” Furthermore, Wikström et. al. states that “it is repeatedly found that users of variable-speed drive systems (VSDS’s) are placing reliability on top of the wish list [26].” These statements are largely based on the facts that VFDs are heavily used in safety critical and high-cost applications, such as transportation, manufacturing, pumping and cooling, where a system-level failure would be detrimental [27].

In [27] a procedure for assessing the reliability of induction motor drives operating under field-oriented conditions is developed. The process begins by identifying the failure modes and failure rates of individual components and subsystems. Next, a VFD simulation was created using MATLAB and Simulink to provide a safe environment for the most extreme faults that were tested in this study. Using the motor-drive simulation model, a parametric analysis was conducted that related various faults to changes in system dynamics. A number of performance-based metrics were used to determine whether or not the changes in system dynamics yielded a system-level failure. The study concluded with the formation of a Markov Model in order to calculate the overall drive reliability.

Markov Models, also discussed in [5] and [27], allow for the integration of a number of redundancy structures at each level of system hierarchy. For example, in additional to series level redundancy, wherein the failure of one component leads to a system level

failure, a number of parallel-structured redundancy mechanisms have been incorporated as well. While this approach provides a method to dynamically assess system performance given component or subsystem failure, constant failure rates were assumed in order to develop the Markov Model. As such, the true accuracy of may be compromised.

2.3 Experimental Selection

Literature review indicated that there exists little work using PoF-based system level reliability assessment methods for power electronic systems. While there has been extensive work regarding PoF simulations and reliability estimations of the power switching module, the control circuitry has rarely been the focus of research efforts. The primary mention of system level assessment methods that include the control circuitry utilize constant failure rates [26][27].

Furthermore, as load levels on the VFD increase the amount of heat dissipated from the power switching module increases as well. The nature of motor-drive packaging causes the dissipated heat to affect the temperatures of the components on the control board. The non-PoF based reliability assessment methods reviewed in literature generally did not take into account the heat dissipation from neighboring subsystems, specifically the power switching module.

This study will develop a PoF-based simulation model of the control circuitry found within the motor drive. Furthermore, the PoF-based failure prediction of the control

hardware will take into account the additional heating produced by nearby subsystems. This study will conclude by validating the PoF-based reliability model through accelerated testing.

Chapter 3: Simulated Assisted Reliability Assessment Approach

Developed by the Center for Advanced Life Cycle Engineering (CALCE), the Simulated Assisted Reliability Assessment (SARA) approach combines PoF based principles and software to assess whether or not a component, part or system can meet specified life cycle conditions [28]. The software allows the user to create a computer model of the component, part or system allowing designers to assess the model for weakness and overall reliability prior to fabrication.

3.1 CalcePWA Overview

CalcePWA is a simulation tool that conducts failure assessments of printed wiring assemblies (PWAs), including thermal and vibration analysis [29]. Maintained by the Electronic Products and Systems Consortium (EPSC) division of CALCE, this software implements failure algorithms based upon existing scientific knowledge that has been published in journal articles, reviewed in textbooks and developed through research conducted at CALCE [29].

Thermal analysis is conducted using control volume theory and a finite element approach and allows the user to determine steady state temperatures of each component on the assembly. Five different modes of analysis are offered including conduction, natural convection (both horizontal and vertical orientation), forced convection, radiation and air cooled cold plates [29]. Vibration analysis, although not conducted in this study, allows for a dynamic characterization of PWA up to the first six mode shapes and fundamental

frequencies. The user can specify the type of boundary clamping condition and can perform analysis using either random vibration or shock inputs [29].

A component-level failure assessment is conducted based upon the component geometries, materials, operating power levels, thermal (and vibration) results and defined loading conditions. Based on these user defined inputs, the software calculates individual failure sites and mean time-to-failure estimations [29]. Furthermore, the failure assessment is conducted in accordance to specific failure mechanisms which extract necessary data from the PWA model and the loading conditions. The failure mechanisms included in the failure assessment that are relevant to this study are package-to-board interconnect failure due to temperature cycling and plated-through-hole (PTH) failure due to temperature cycling.

3.2 Building the CalcePWA Model

All three printed circuit boards (PCBs) in the motor drive were modeled in CalcePWA. Although the focus of this study is primarily on the control board and standard components on the power board, both the connector board and power board were modeled completely in order to formulate a complete model of the system. The rest of this section will discuss the fundamental constituents of the CalcePWA model including materials, types of components and basic geometries. While this section will describe many of the essential parameters used, a complete list of all parameters is listed in the appendix.

3.2.1 Printed Circuit Boards

The control board was modeled as a nine layer board: two thin protective layers, four copper trace layers, and three FR4 epoxy layers. Figure 14 shows a schematic of the PCB cross-section, with each layer numbered 1 through 9.

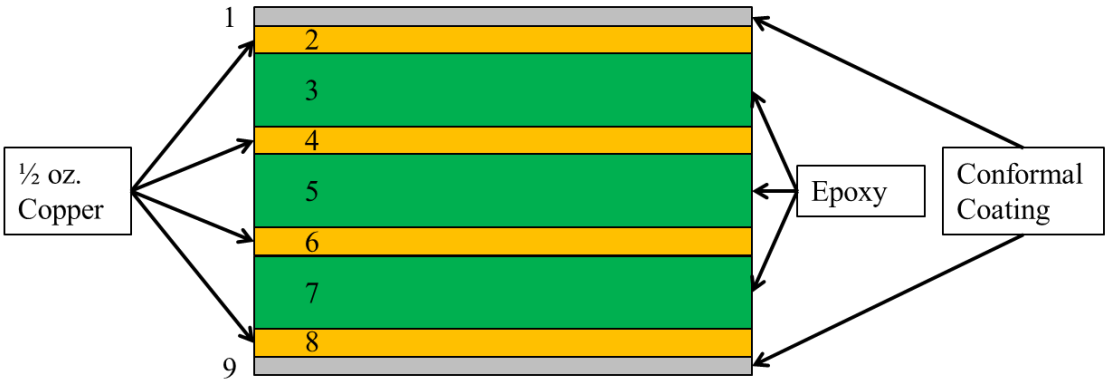

Figure 14 Schematic of control board cross-section (not to scale)

The two outer layers (layers 1 and 9) consist of a 0.1 mm thick paralene conformal coating. Conformal coatings are thin protective layers designed to protect circuit boards and assemblies from failure, especially under harsh environmental conditions. They particularly provide protection against moisture, dirt, chemicals, organic solvents and other forms of contamination [30]. Layers 2, 4, 6 and 8 are modeled as ½ oz. copper. Copper is conventionally measured in ounces, which represents the weight of copper that is spread over one square foot. ½ oz. copper converted to SI units yields a thickness of 0.018 mm. Copper layers 2 and 8 are modeled to contain 25% metallization while copper layers 4 and 6 are modeled to contain 60% metallization. Percent metallization is a way to model the percentage of the layer area that is covered by traces. The numbers chosen, 25% for layers 2 and 8 and 60% for layers 4 and 6, were based on the assumption that the two inner layers are used more for grounding purposes while the outer two layers are

used more for tracing between components. Layers 3, 5 and 7 are modeled as 0.5 mm thick FR4 epoxy. The total thickness of the board is 1.772 mm.

The power board was also modeled also as a nine layer board and Figure 14 can also be used to represent a schematic of the cross-section. Like the control board, the two outer layers of the power board (layers 1 and 9) were modeled as a 0.1 mm thick paralene conformal coating. However, instead of ½ oz. copper layers the power board was assumed to contain four 2 oz. (0.0696 mm) copper layers. This assumption was based on the fact that the power board would operate at significantly higher current levels than the control board and would require thicker copper traces to prevent against trace failure. All four copper layers were modeled to contain 50% metallization. The three FR4 copper layers between the copper layers were modeled to be 0.62 mm thick, yielding a total board thickness of 2.34 mm.

Lastly, the connector board was modeled as a five layer board, shown in Figure 15. Due to the fact that this board contains components on one side, only two 2 oz. copper layers are necessary, one for traces and the other for grounding. Like the Power board, the connector board will operate at significantly higher power levels than the control board, thus requiring thicker copper traces. The two outer layers consist of a 0.1 mm thick conformal coating and the FR4 epoxy layer between the two copper layers is 2.008 mm thick. Both copper layers are modeled with 50% metallization.

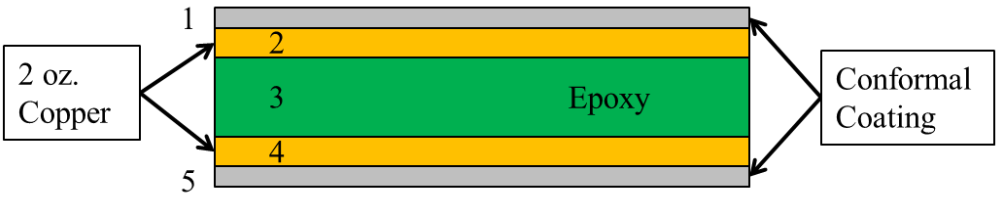

Figure 15 Schematic of connector board cross-section (not to scale)

3.2.2 Passive Surface Mount Devices

Both the control and power boards contain numerous surface mounted devices (SMD) of varying sizes. In order to simplify the model, resistors and capacitors smaller than the standard 1206 size (3.2 mm x 1.6 mm) [31] were not included. Figure 16 shows examples of SMD resistors and capacitors that were included in the CalcePWA model. The resistors and capacitors enclosed in yellow were included but the others, such as those in the lower right hand corner of the image, were not included.

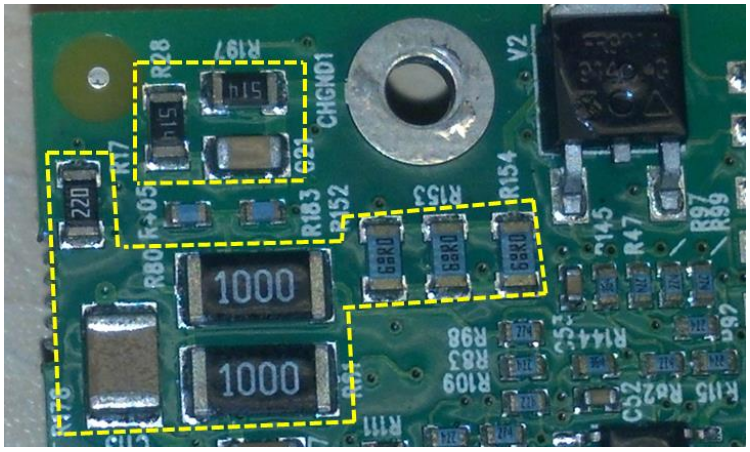

Figure 16 Sizes of SMD components included in model

Modeling these components in CalcePWA required a series of parameter inputs. Table 2 lists the parameters required for the SMD resistors and capacitors.

Table 2 Parameters for SMD resistors and capacitors

Part Length	Max I/O	Thermal Resistance
Part Width	Standoff Height	Nominal Power Dissipation
Part Thickness	Solder Height	Solder Material
Substrate Material	Solder Joint Bond Area	Part Outline Type
Part Weight	Max. Rated Temperature	

Many of these parameters were found in generic manufacturer provided datasheets. Estimations, assumptions and caliper measurements were used to determine those parameters that were not found in datasheets. For example, Aluminum Oxide (Al_2O_3) was used to model the substrate material for all SMD resistors while Barium Titanate ($BaTiO_2$) was used to model the substrate material for all SMD capacitors. There also exist two glass body diodes, shown in Figure 17, that were modeled using soda glass as the base material with tungsten end caps. Several tantalum capacitors also exist on the control board, also shown in Figure 17. Furthermore, standard SAC305 solder was used as the solder for all components on all boards.

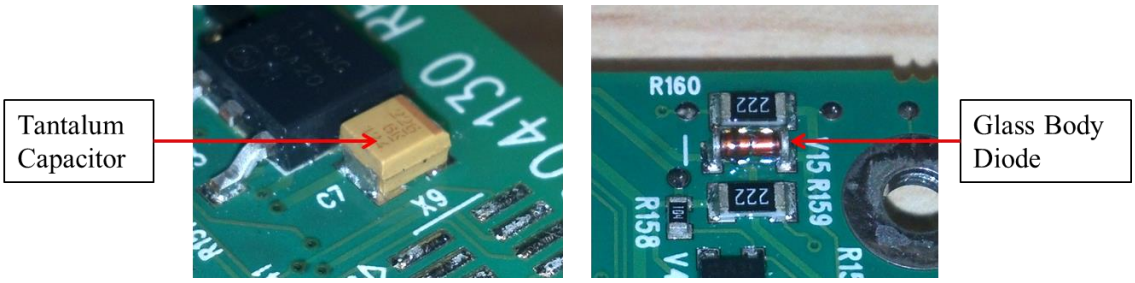

Figure 17 Tantalum capacitor (left), glass body diode (right)

3.2.3 Plastic Encapsulated Microcircuits

Plastic encapsulated microcircuits (PEMs) exist both on the control and power boards. These types of components encapsulate a silicon die with an epoxy-based material to

protect the active device from environmental hazards. Figure 18 displays examples of PEMs that were included in the CalcePWA model.

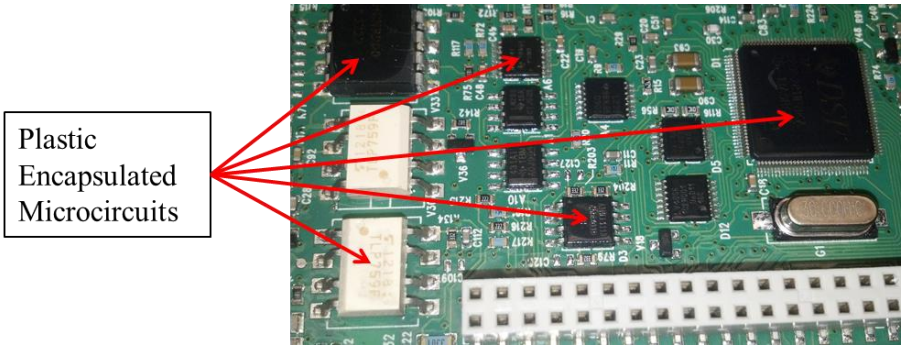

Figure 18 Examples of PEMs included in CalcePWA model

Table 3 lists the parameters required to create a PEM device in the CalcePWA model.

Table 3 Parameters required for PEM devices

Part Length	Interconnect Span	Interconnect Pitch	Interconnection Type
Part Width	Part Outline Type	Max I/O	Standoff Height
Part Thickness	Lead Material	Solder Height	Max. Rated Temp.
Package Material	Gullwing Geometries	Solder Joint Area	Thermal Resistance
Die Pad Position	Die Pad Length	Die Pad Width	Internal Pressure

All PEM devices in the model utilized gullwing leads to interface with the PCBs. Unlike passive SMDs, which only use the solder joint bond area parameter to define the device interface, these devices require a number of geometry parameters to define the gullwing interconnect. Figure 19 shows a screen shot of the CalcePWA gullwing definition parameters.

Lead Material Reference :	lead.C197	
Gullwing length between case and bend :	0.25	mm
Gullwing radius of first bend :	0.5	mm
Angle of Incline (A2) :	10	degrees
Gullwing length between first bend and transition :	0.15	mm
Gullwing length after transition :	0.15	mm
Gullwing radius of second bend :	0.5	mm
Gullwing foot length :	0.5	mm
Gullwing width prior to transition :	0.41	mm
After transition width :	0.41	mm
Gullwing thickness :	0.22	mm

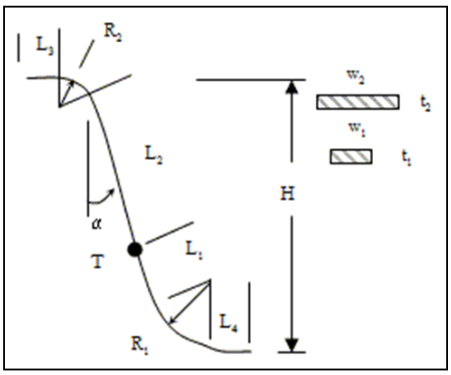

Figure 19 Gullwing definition parameters

Although many of these parameters could be defined based upon information from component data sheets, parameters that could not be found in datasheets were estimated based upon similarly defined components and caliper measurements. Table 4 lists all assumptions made with respect to modeling the PEM devices. All parameter data along with any variation to these assumptions can be found in the Appendix.

Table 4 Assumption for PEM modeling

Thickness of Solder Under Lead	0.1 [mm]
Lead Material (small, thin, low profile)	Alloy 42
Lead Material (larger PEMs)	Copper Alloy 197
Mold Material	Epoxy Biphenol
Internal Package Pressure	1 [atm]
Permeation Constant	1
Die Pad Position [mm]	(1/2)*(package thickness) – 0.1
Die Pad Length [mm]	(1/3)*(package length)
Die Pad Width [mm]	(1/2)*(package width)

3.2.4 Connectors

The control and connector boards house the connection components which interface with the rest of the motor drive system. While the connector board contains the AC source and motor connectors, the control board contains the connections modules used for control

wires, an Ethernet port and two female connector modules that interface with the power board.

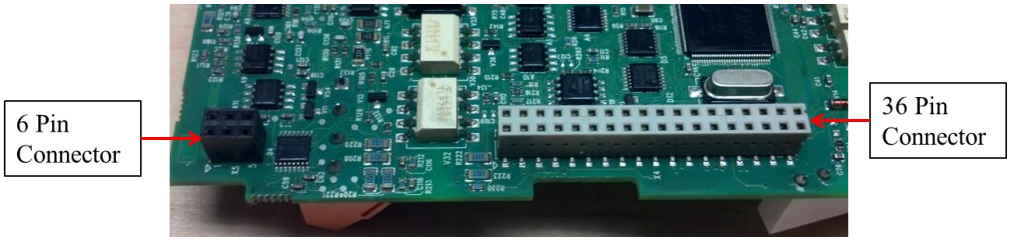

Figure 20 Connectors interfacing with power board

Likewise, there exist three male connector modules on the power board, a 6-pin and 36-pin connector to match those described in Figure 20, and a 2-pin connector in which the fan is plugged into. These three connectors are shown in Figure 21.

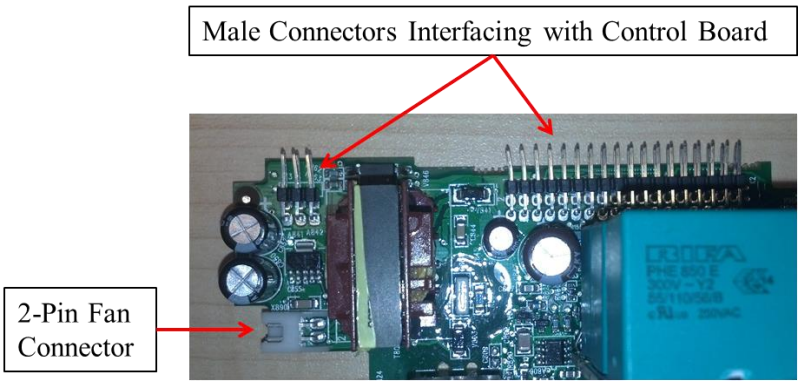

Figure 21 Male connectors on power board

All female connectors, the Ethernet port the connector modules for the control cables and connector modules for the AC power source and motor, were modeled as either a liquid crystal polymer or a 30% glass filled polyetherimide (Ultem30). Furthermore, all connectors were either modeled with gullwing style leads, or through-hole style leads. Figure 22 shows a screen shot of the CalcePWA through-hole style parameter definitions. Two assumptions universally made for all components utilizing through-hole style leads are that the solder area is 3 mm^2 and that the solder height is 1 mm.

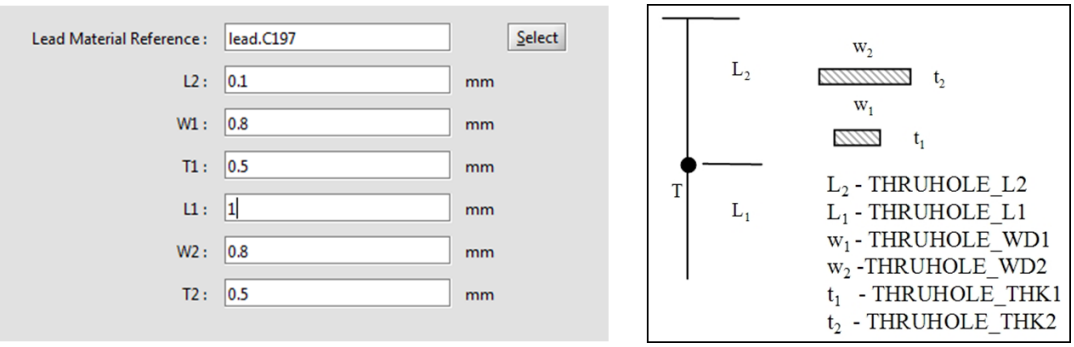

Figure 22 Screen shot of CalcePWA through-hole lead definition

3.2.5 Customized Components

On all boards, there existed a number of components that were required to be custom-made. In order to model these components and include them in the reliability analysis, generic blocks were created which captured the overall geometry of the device along with the specific interconnect type (gullwing, or through-hole). Corresponding materials, including the packaging and lead frame materials, were specified as well. This allowed a failure assessment to be performed in relation to the solder joints. These components include the IGBT, relays, LEDs, crystal, film and electrolytic capacitors, transformer, choke, meal oxide varistors, silicon rectifier diode and ceramic cased wirewound resistor. All parameters for each of the customized components are included in the Appendix of this report.

3.2.6 Final CalcePWA Model

A side-by-side comparison of the CalcePWA model to the actual motor drive assemblies is displayed. Figure 23 shows the comparison of the control board to the CalcePWA model, while Figure 24 and Figure 25 show the comparison of the power board and

connector board respectively. The large heat sink in the power board is left out of this comparison for display purposes.

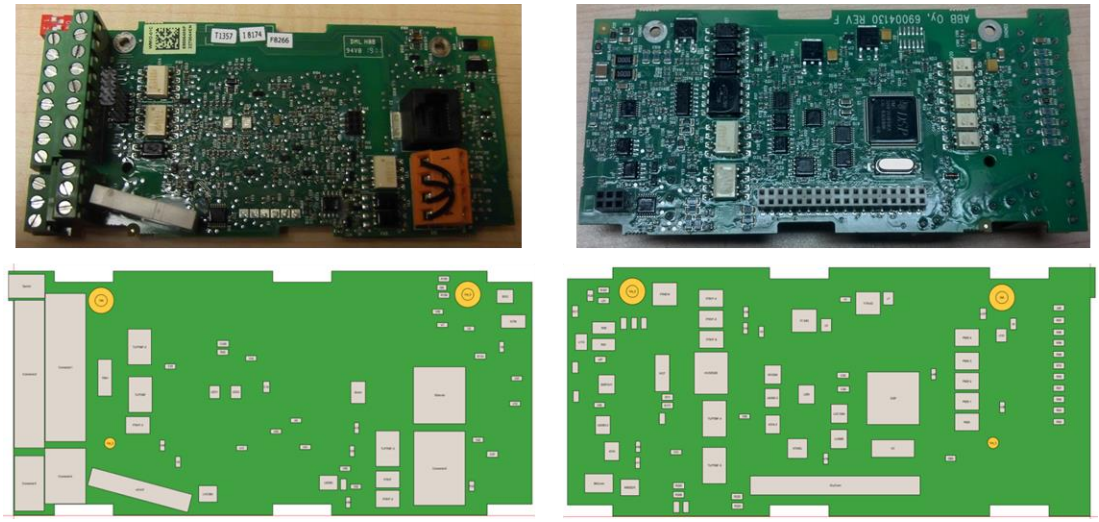

Figure 23 Comparison of control board to CalcePWA model – top side (left), bottom side (right)

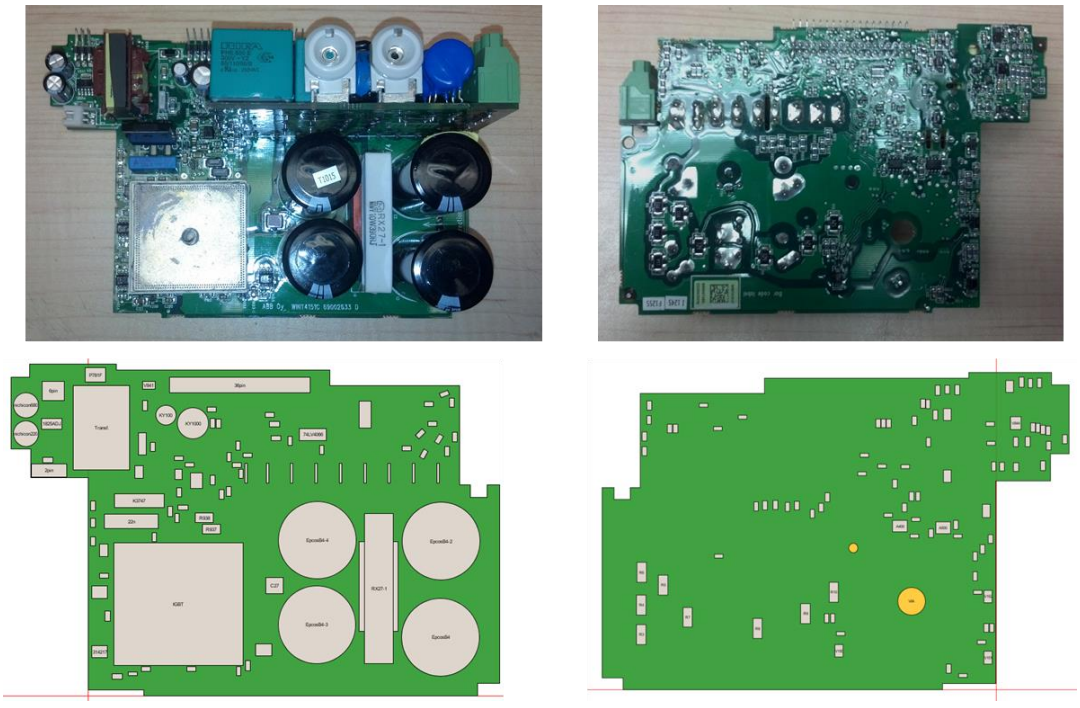

Figure 24 Comparison of power board to CalcePWA model - Top side (left), bottom side (right)

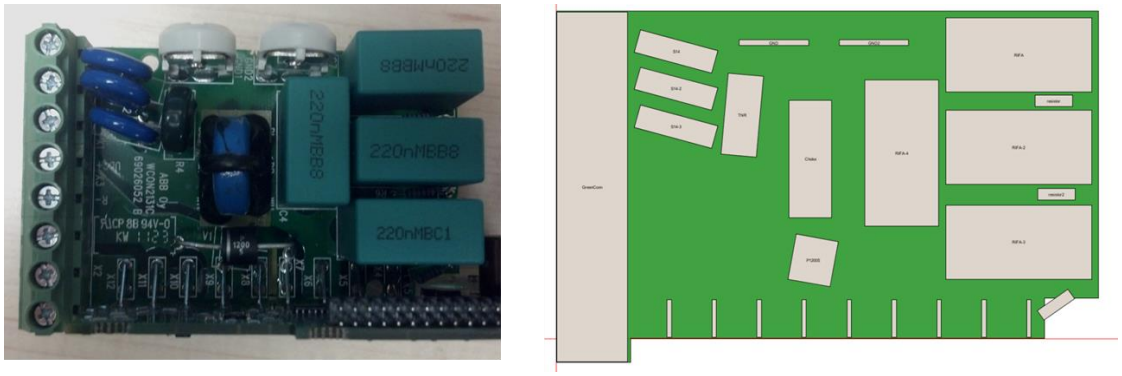

Figure 25 Comparison of connector board to CalcePWA Model

3.3 Discussion and Analysis of CalcePWA Model

A total of 323 components were included in the CalcePWA model. The process of gathering parameter data for each component consisted of searching through manufacturer provided data sheets to get the geometries and materials of the packages. There were a large number of assumptions made primarily relating to materials and lead geometries. While the assumptions included in the model are stated in this report, further studies will be required to determine the sensitivity that CalcePWA has to small variations in these parameter.

CalcePWA best models assemblies that contain standard parts such as surface mounted passive devices, plastic encapsulated microcircuits, connectors and generically modelled blocks. To develop a complete model, a number of components such as the film and electrolytic capacitors, the power switching module, the inductor and the metal oxide varistors (along with many more) were created by redefining the parameters of generic blocks according to the specific component material and geometrical properties. This

allowed all parts to be included in the model along with their respective interconnect properties.

Overall, CalcePWA provides a method to simplify a complex assembly which allows for a first order reliability analysis to be performed on the interconnects. Although the actual construction of the model takes time to build (this is due to the complexity of modelling 323 components), CalcePWA allows for quick thermal and reliability analysis of the assembly. While other software programs utilizing a complete FEM approach may take hours to run a simulation, this software performs a simplified simulation in seconds.

Chapter 4: Load Generating Test Setup

A magnetic brake, also known as an eddy-current brake or electromagnetic brake, was used to generate a load on the motor drive. Other load-generating mechanisms were investigated such as dynamometers and coupling the motor to an identical motor driven in reverse. However, researching all possible methods indicated that the magnetic brake proved to be the most cost-effective and appropriate solution for this application. This section will discuss the fundamental components of the test setup along with the system construction. The section will then conclude by discussing preliminary benchmark testing of the entire electromechanical drive system.

4.1 Three-Phase Induction Motor

The variable frequency drive is directly connected to and controls a three-phase induction motor, shown in Figure 26.

Figure 26 Three-phase induction motor

The specifications of this motor are displayed in Table 5.

Table 5 Three-phase induction motor specifications

Manufacturer	Leeson
Model Number	C6T34DB17D
Horsepower	3
RPM	3450
Voltage	208 - 230 / 460
Full Load Amps (FLA)	8.4 - 7.6 / 3.8
Safety Factor Amps (SFA)	9.4 – 8.6 / 4.3

4.2 Magnetic Brake

Magnetic brakes operate under the principle of energy conversion, specifically converting kinetic (rotational) energy into heat. Conventional friction brakes, such as the disc brakes in cars, operate under a similar principle wherein a rotating disc is slowed down by an opposing friction force created by the a braking pad. A schematic of the friction brakes that exists in cars is shown in Figure 27 Conventional disc friction brake.

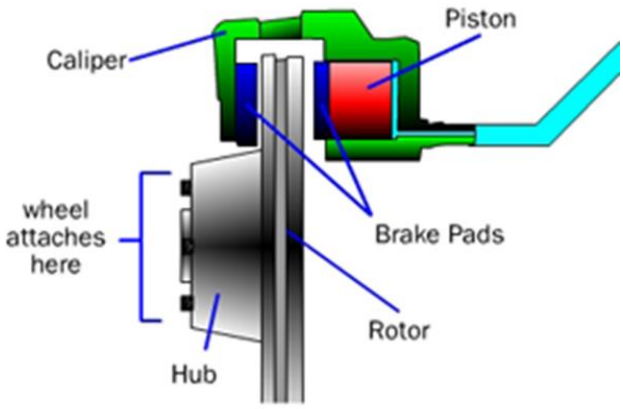

Figure 27 Conventional disc friction brake

However, unlike friction brakes magnetic brakes do not physically contact the rotating part thus damage and wear are less likely to occur. They operate according to the principle of eddy current generation. Eddy currents are generated when a conductive material moves through a time-varying magnetic field [32]. Lenz's Law states that when a change in a magnetic field occurs, an opposing electric field is generated [33]. This

opposing electric field is often times referred to as a “back-EMF” and is responsible for the braking that occurs within a magnetic brake.

In the magnetic brake used in this study, a magnetic field is generated by a large coil that is electrically activated through a number of remote power supplies and a controller. A three-phase induction motor, driven by the VFD, is mechanically coupled to the shaft of the magnetic brake. The shaft is also attached to the impeller and drag ring shown in Figure 28. As the motor rotates, the drag ring rotates through the magnetic field. Eddy currents are generated, according to Lenz’s Law, and create an opposing force in the opposite direction of the shaft’s rotation. This opposing force is in essence a torque on the motor and functions as the load through which the motor drive must operate under. The amount of torque applied to the motor can be altered by changing the strength of the magnetic field. The user controls the amount of current entering the controller. The controller dictates the strength and time-varying properties of the magnetic field in the brake in order for eddy currents to be generated. While there are numerous types of electromagnetic brakes, this description should roughly cover the fundamental principles of operation.

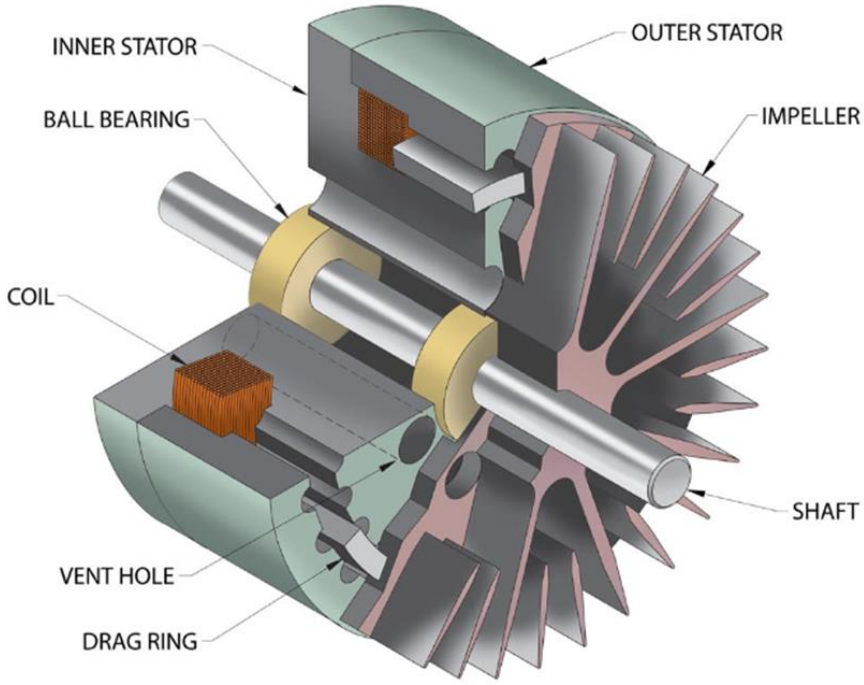

Figure 28 Schematic of magnetic brake [34]

This setup used the MBL-8.7 magnetic brake system manufactured by *Magnetic Brake Systems*, a division of *Technical Film Systems*. An image of the brake is shown in Figure 29, while a schematic of the brake is shown in the Appendix.

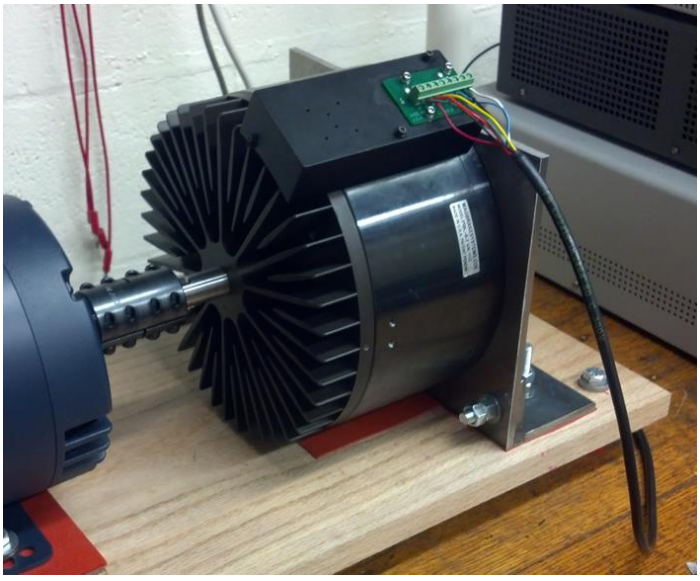

Figure 29 MBL-8.7 magnetic brake system

The amount of torque generated by the brake is linear and proportional to an analog voltage signal the user sends to the controller [34]. The control unit processes the analog signal and governs the amount of current sent to the brake for torque generation. The MBL-8.7 is designed so that the relationship between the current sent to the brake and the torque produced have relatively little hysteresis [34]. This relationship is shown in Figure 30.

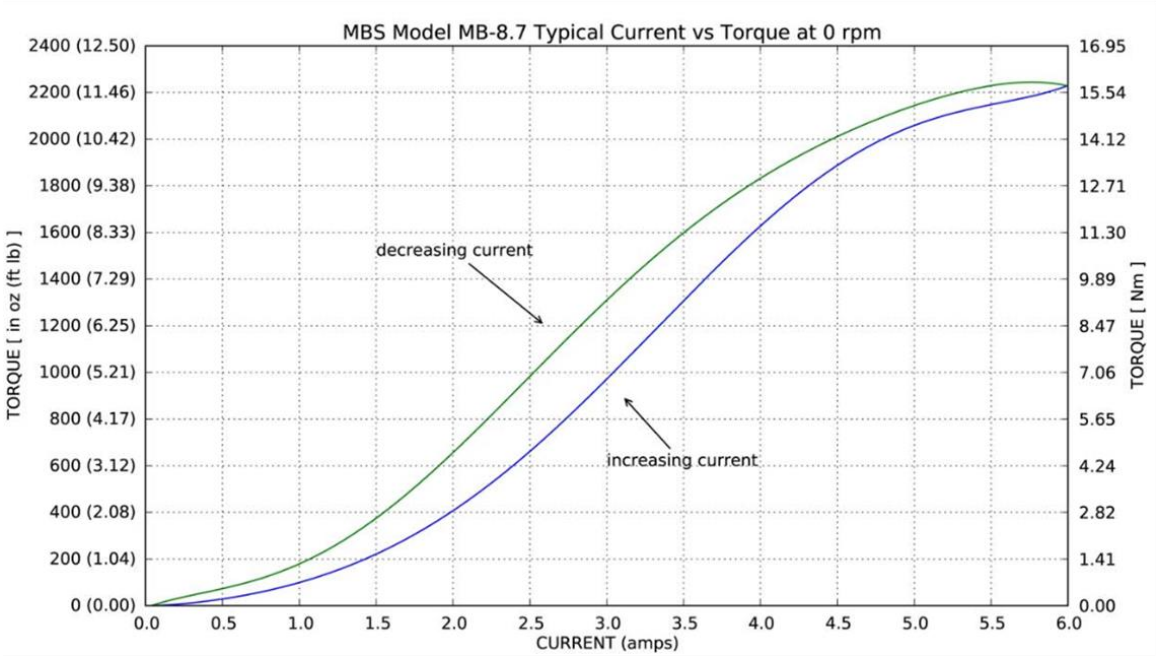

Figure 30 Torque vs. current relationship in MBL-8.7

The maximum rated torque the motor can withstand is calculated using the equation below [35], where torque is in units ft.-lbs.

$$Torque = \frac{Horsepower\ x\ 5252}{RPM}$$

The maximum torque is calculated to be 4.567 ft.-lbs., which equates to 876.9 in.-oz. This calculation becomes important when determining whether or not the magnetic brake can sustain continuous operation at these torque levels without overheating. Figure 31

shows the maximum operating torque and speeds at which the MBL-8.7 can operate at without overheating.

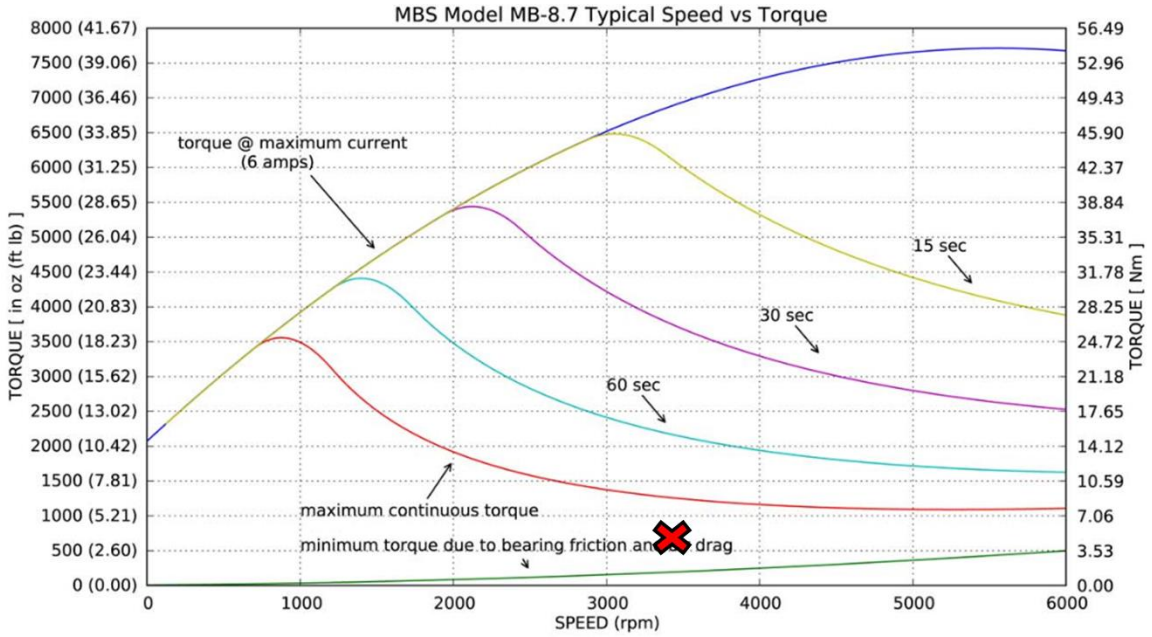

Figure 31 Torque vs. speed maximum operating time

The ‘X’ indicates the maximum operating point (3450 RPM and 876.9 in.-oz. of torque) in which the motor can operate at. This point falls below the maximum continuous torque line, indicated by the red curve, thus the magnetic brake can dissipate all the converted heat energy without overheating. Furthermore, the system is controlled in such a way that the relationship between input current and torque output is independent of the operating speed [34]. This means that the analog signal sent to the controller from the user will yield the same torque on the motor, regardless of the speed.

The MBL-8.7 requires two 24 VDC power supplies (one +24 VDC and one -24 VDC). Each of these power supplies must be capable of outputting 0 – 4 Amps. An additional power supply, 0 – 10 VDC and 0 – 0.25 Amps, is required to generate the analog signal sent to the controller. All three power supplies are connected to the controller, which in

turn is connected directly to the brake. Figure 32 shows the three power supplies and the controller.

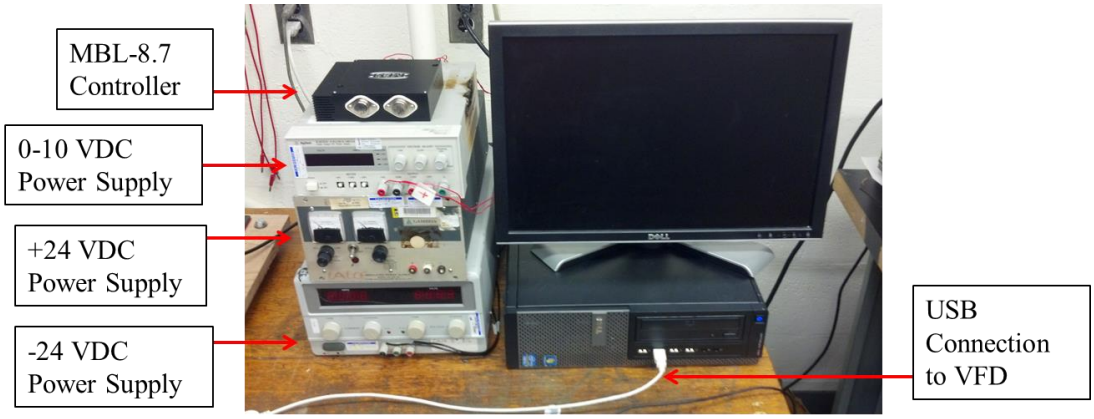

Figure 32 Power supplies and MBL-8.7 controller

4.3 Transformer

In order to meet the power requirements of the drive, a transformer was used to convert the three-phase 208 VAC power from the wall to three-phase 480 VAC power. The transformer was a T204H15E model manufactured by Federal Pacific, shown in Figure 33. It has a power rating of 15kW, a primary delta configuration and a secondary wye configuration. A safety switch was also included to eliminate the need for continuous plugging and unplugging from the wall. In addition, three fuses (one for each phase-line) rated to 15A were placed between the wall outlet and the switch to protect the circuit breaker in the building. Both the safety switch and the fuses are shown in Figure 33 Transformer, switch and fuses.

Figure 33 Transformer, switch and fuses

4.4 Assembly of Electromechanical Motor Drive System

Power is transmitted between the motor and the magnetic brake through a mechanical coupling, shown in Figure 34. The coupling is made of steel, is rated for up to 51200 in.-oz. of torque at 4000 RPM and utilizes the ANSI standard keyways machined into the brake and motor shafts.

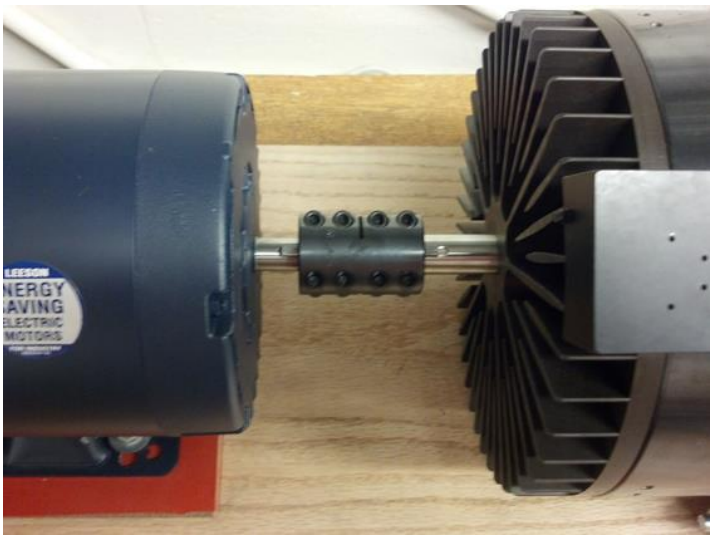

Figure 34 Mechanical coupling between motor and magnetic brake

The MBL-8.7 is not manufactured with a means for mounting the device to a surface. The torque generated will cause the system to rotate. Therefore a bracket used to fasten the brake to a sturdy surface was developed. Other methods, such as purchasing extra parts from the manufacturer, were investigated but it was determined that manufacturing a custom bracket would be the most cost-effective and efficient method. Figure 35 shows an image of the bracket fastening the brake to a wooden base.

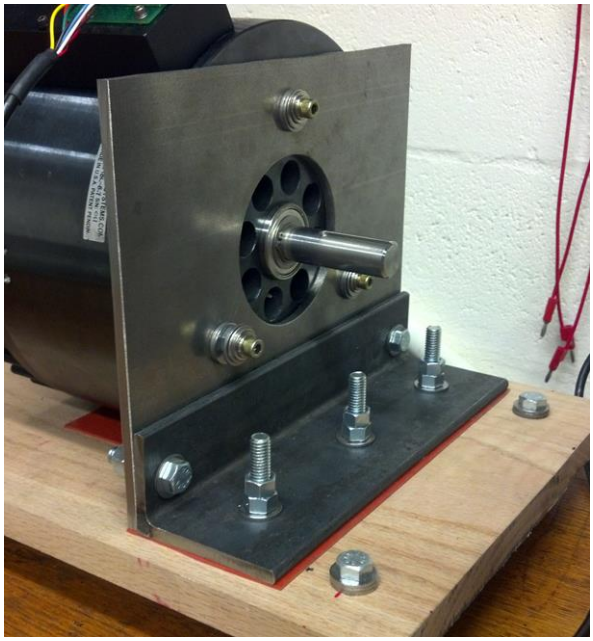

Figure 35 Bracket fastening brake to wooden base

4.4.1 Vibration Damping Components

Multiple methods to reduce vibration were implemented in the design of this system. Although the centers of the motor and brake shafts were aligned as concentrically as possible, any deviation from perfect alignment will result in vibrations. At speeds up to 3450 RPM, these small vibrations may produce significant stresses on the system. Furthermore, vibration damping techniques were implemented to also mitigate noise

created from vibrations. Figure 36 shows vibration-damping pads located under the motor and brake to absorb energy created from vibrations.

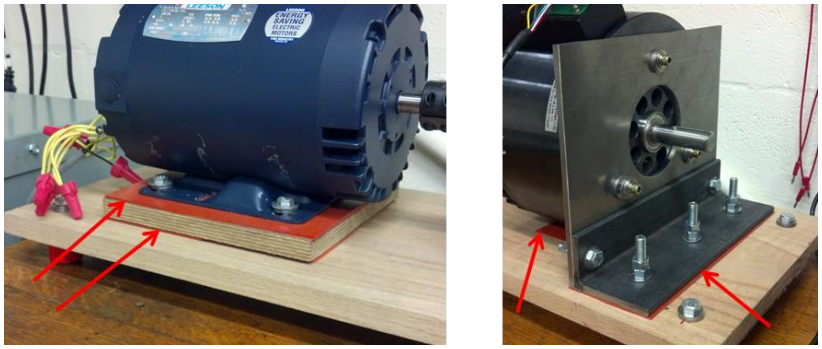

Figure 36 Vibration damping pads under motor (left) and brake (Right)

These pads were made of silicone-rubber and consisted of two thicknesses: 1/16” thick and 1/32”. Aside from damping vibrations, they also served as spacers to finely adjust the height of both the motor and brake. This provided a simple means to align the centers of the motor and brake shafts.

Another mechanism used to dampen vibrations were four rubber feet located at the corners of the wooden base. Shown in Figure 37, these bumpers also provided enough space between the wooden base and the table the assembly would rest on to access the nuts and bolts used to fasten down the components.

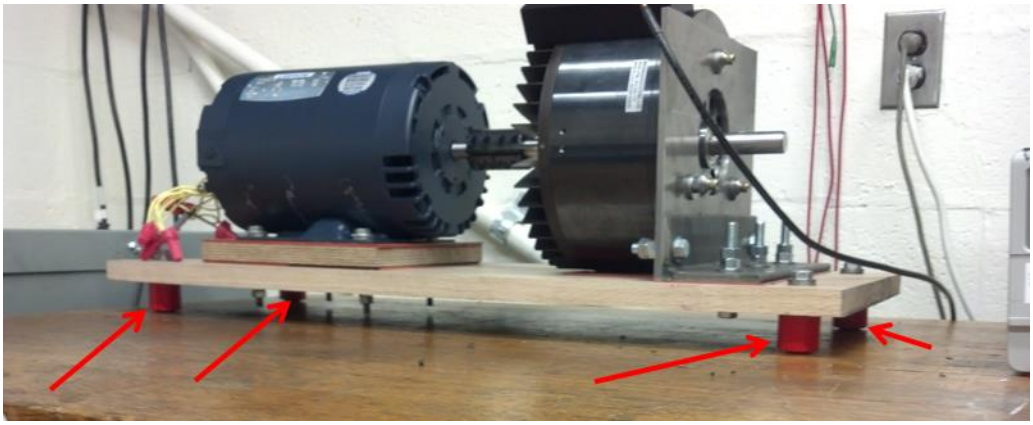

Figure 37 Vibration damping rubber bumpers

4.4.2 Motor – Brake Subassembly

The induction motor, magnetic brake and vibration-reducing mechanisms were all mounted to a wooden base, creating a portable subsystem. Rather than permanently mounting the components to a table or the floor, a subassembly was created to allow for more freedoms with regards to placement and arrangement of the system. In order to accurately design the subassembly and allow for proper vertical alignment of the brake and motor shafts, a SolidWorks model was created that captured the dimensions of all components. Shown in Figure 38, this model also provided a method to determine how thick and how many vibration pads must be included to create necessary spacing.

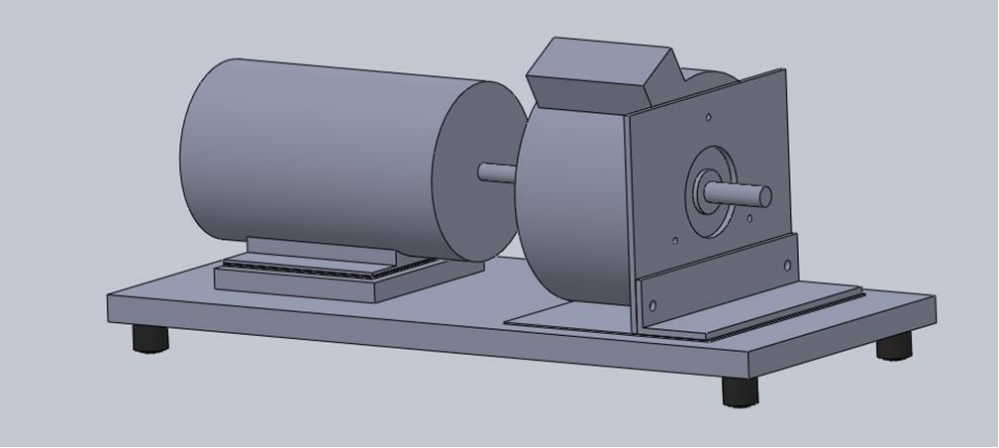

Figure 38 SolidWorks model of motor-brake subassembly

Figure 39 shows the motor-brake subassembly created according to the SolidWorks model. Although not shown for display purposes, this subassembly will be enclosed in a cardboard fixture during testing to reduce noise, prevent undesired airflow from cooling the drive and to enhance safety of the test setup.

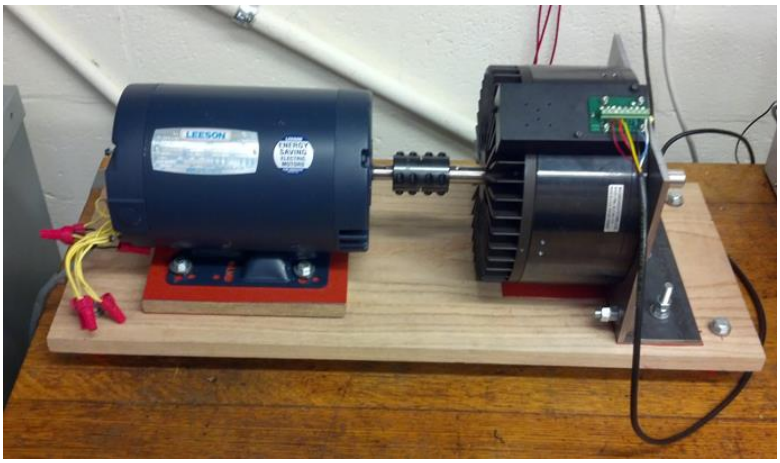

Figure 39 Motor-brake subassembly

4.5 Entire System Layout

An additional SolidWorks model was created of the entire system, shown in Figure 40. This allowed the proper placement of all components to be determined with respect to testing room and allowable space.

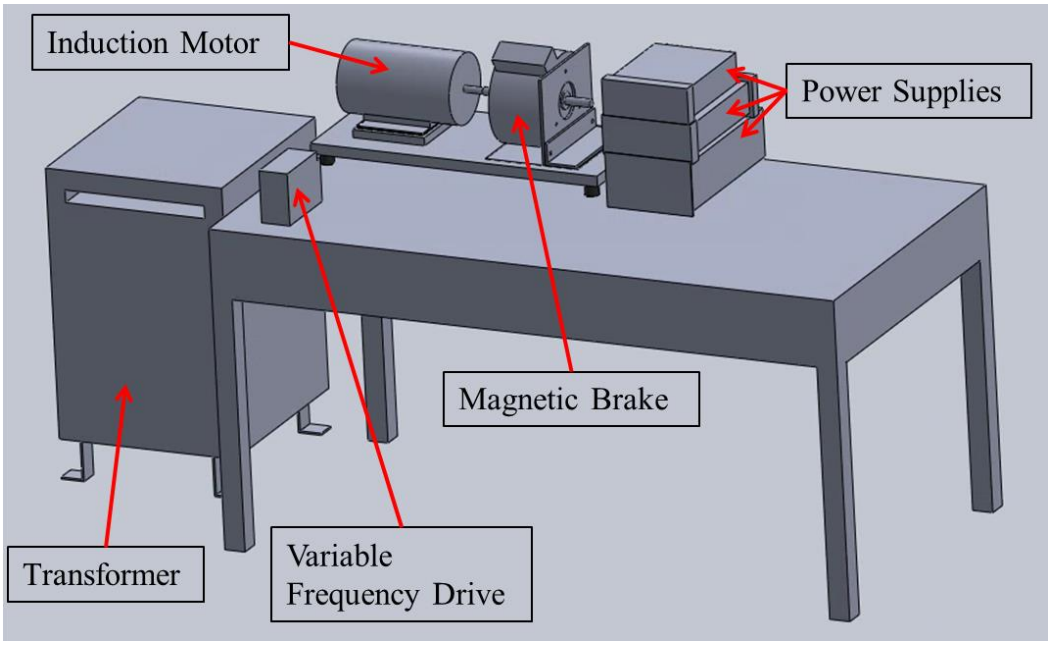

Figure 40 SolidWorks model of entire test setup

The actual test setup, including all subassemblies and components, is shown in Figure 41.

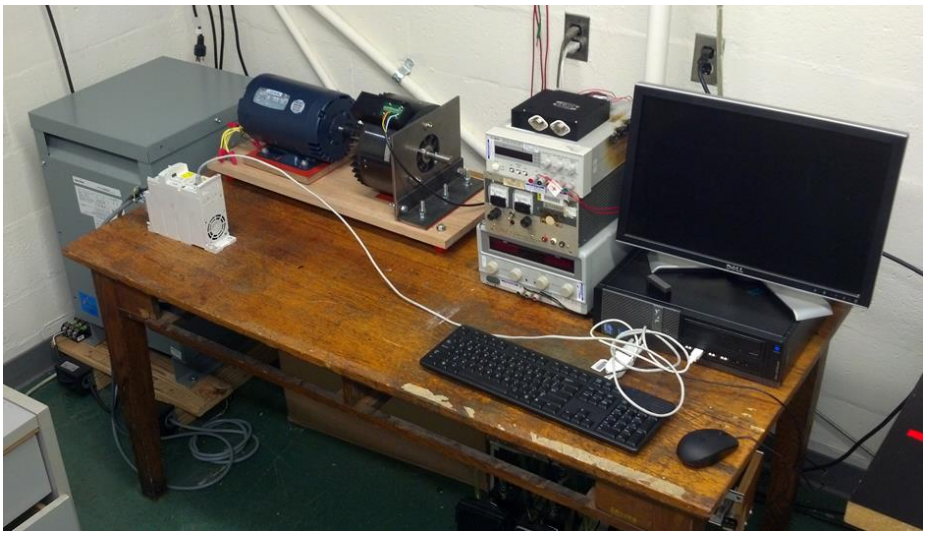

Figure 41 Entire VFD test setup

Table 6 shows the information regarding all components used to construct the test setup. Many parts were ordered from McMaster, therefore part numbers were included if applicable.

Table 6 Part information for motor drive test setup

Part	Information	McMaster Part Number
Transformer	Federal Pacific T204H15E	N/A
Fuses	15A UL Class RK5 Time-Delay	7049K13
Variable Frequency Drive	ABB ACS355-03E-05A6-4	N/A
Three Phase Induction Motor	Leeson C6T34DB17D	N/A
(+) 24 VDC Power Supply	Lambda LH125FM	N/A
(-) 24 VDC Power Supply	Good Will Instruments GPR-3510HD	N/A
0 - 6 VDC Power Supply	Agilent E3630A	N/A
Magnetic Brake System	MBL - 8.7	N/A
Vibration Damping Pads	Silicone-Rubber 1/16" and 1/32" Thick	8632K42, 8632K41
Rubber Feet	Polyurethane Bumper with 3/8"-16 Thread	9546K51
Cable	Shielded, 18AWG, 4 Conductor	9936K58
Wooden Base	30" x 12" Oak Board	N/A
Wooden Block Under Motor	Marine Grade Plywood, 3/4" Thick	1125T41
Metal Bracket to Fasten Brake	Low Carbon Steel 90 Degree Angle, 1/4" Thick	9017K81
	Low Carbon Steel Sheet, 1/4" Thick	6544K24
Bolts	3/8"-16 Thread, 1-1/2" and 2-3/4" Lengths	91309A628, 91309A635
Nuts	3/8"-16 Thread	90473A031
Washers	3/8" Screw Size, 13/16" O.D.	91083A031

4.6 Initial Load Testing of Magnetic Brake System

Prior to any extended testing on the drive, it was important to both ensure proper functioning of the magnetic brake system and to assess the load levels that the magnetic brake can generate on the motor drive. The motor in this setup has a full-load amperage (F.L.A) rating of 3.7 and a safety factor amperage (S.F.A.) rating of 4.3A. The F.L.A rating describes the amount of current needed to operate the motor at full load under the supply voltage [36] while the S.F.A rating describes the overload capacity at which the motor can periodically operate at without causing damage [37].

The first benchmarking test compared the amount of torque generated by the brake to the amount of current sent to the motor from the VFD. This test simply validated the proper functioning of the magnetic brake system, the datasheets provided by the brake manufacturer and its ability to generate a load on the drive. The amount of torque generated by the brake was controlled by adjusting the voltage level on the 0 - 6 VDC power supply. Measurements were taken at 20, 30 and 40 Hz. Table 7 displays the results from this test in which the percent torque is a percentage of the maximum rated torque the motor can withstand. While the induction motor has a maximum torque rating, computed in Equation 3, the VFD can periodically overload the motor and is rated to drive the motor at 150% of its rated torque for up to six seconds. This scenario, where the VFD operates the motor above 100% of its rated torque, only applies if the magnetic brake system generates a torque on the motor above 876.9 in.-oz. (as calculated in Equation 3). For reference purposes, the magnetic brake system is able to generate a maximum torque up to 2200 in.-oz., however this would only be relevant in different applications with much larger motors (up to 6.7 HP).

Table 7 Comparing percent torque of motor to current from VFD

20 Hz		30 Hz		40 Hz	
Amps	% Torque	Amps	% Torque	Amps	% Torque
1.6	7.2	1.6	10.8	1.6	10.6
2.0	34.2	2.0	32.8	2.1	32.0
2.6	50.7	2.6	49.9	2.7	52.8
3.5	76.6	3.5	74.5	3.6	74.0
4.4	100.3	4.6	101.8	Fuses Blew	
5.8	134.2	5.0	113.5		

Higher load levels induced on the motor while operating at 40 Hz resulted in blown fuses. This was due to current spikes that occurred during start-up which exceeded the original 10A fuse rating. 15A fuses were installed in the system and the problem was fixed. As

the amount of torque on the motor increased, the VFD was required to output more current to the motor to maintain a constant speed. Table 7 shows that 4.3A equates to roughly 100% of the full load operating torque while 3.7A equates to roughly 75% - 80% of the full load operating torque. This validated the manufacturer specifications of the motor and the VFD.

A second validation test was performed which measured the percentage full load operating torque to input current at different speeds. This was essentially a motor efficiency test and the results are displayed in Table 8.

Table 8 Percent torque at varying frequencies

% Torque	Full Load Amps (3.7A)	Safety Factor Amps (4.3A)
10 Hz	85.3	99.6
20 Hz	82.0	97.5
30 Hz	80.0	94.7
40 Hz	76.0	No testing
50 Hz	75.0	

This test shows that as the speed of the motor increases while maintaining a constant input current, the percent full load operating torque decreases. This can be attributed to mechanical, electrical and magnetic losses that occur. An example of a mechanical loss could be increased friction in the ball bearings due to higher rotation speeds. While identifying and quantifying the types of losses fall outside the scope of this project, it is important to note that these losses do occur and will be present in this experiment.

These preliminary tests also brought to attention the large amount of noise that was generated when the system operated above 30 Hz.

4.7 Discussion and Analysis of Testing Apparatus

This setup provides a successful method to generate loads on induction motors and variable frequency drives. The relatively low cost of the system, compared to other methods investigated, enabled this setup to be reconstructed in other testing environments. Furthermore, the MBL-8.7 has the ability to generate a wide-range of torque. While a 2.2 kW motor drive system was tested in this study, the MBL-8.7 can be used for testing motors up to 5 kW (6.7 HP) in the same manor. Figure 31 should to be consulted prior to any change in the setup to ensure proper operating times to prevent overheating of the brake.

Safety was of major concern because the power levels were large enough to cause serious injury or death. As such, a number of precautionary measures were taken. Prior to every operation, all wiring was checked and double checked. Caution signs were posted all throughout the testing room. Wire thickness calculations, fuse sizes, transformer placement, magnetic brake power supplies and switches were all properly checked and verified to prevent unforeseen dangers. Furthermore, the mechanical forces generated during testing were also significant enough to cause great serious harm. The motor-brake subassembly required significant effort to ensure that the materials, design and interactions between parts could withstand the generated forces with a sufficient safety factor. These calculations were conducted with scrutiny to ensure no mistake was made. The final test setup was successfully tested and operated as expected. Finally, the testing apparatus will remain intact to be used in further studies at CALCE involving similar motors and drives.

Chapter 5: Overview of Method to Assess Thermal Profile

The ultimate goal of this research was to develop a method to assess the reliability of the control circuitry within a VFD. The specific failure mechanisms investigated in this were those related to interconnect failure, which are largely dependent on temperature and temperature changes. While these failure mechanisms are by no means a comprehensive survey of all failure mechanisms that are applicable to motor drives, the validation efforts used in this project were designed to specifically accelerate those dependent on temperature and temperature changes. The specific failure mechanisms are discussed later in the report.

In order to create a temperature change, two different power levels were used. This was based on the assumption that different power levels result in different temperatures within the drive. One power level occurred while the drive was turned on but not running the motor and the other power level occurred while the drive was operating the motor at full-load (3.7A). It was initially predicted that the idle condition would produce lower temperatures than the full load condition surrounding the control circuitry. However, testing as described in the *Boundary Temperature Measurements* chapter revealed the opposite to be true.

A thermal simulation of each board was conducted at both the idle and full load conditions. The results of these simulations were a series of thermal profiles that were used in the reliability assessment. However, two component and system-level parameters were left out of the CalcePWA models due to lack of information. These needed to be

determined through experimental efforts in order to complete the CalcePWA models and conduct the simulations. They were individual component power dissipation and the thermal boundary conditions. Table 9 lists the steps taken to find the missing information and generate the thermal profiles of the control board.

Table 9 Steps to generate thermal profile of control board

1	Setup control board to run outside motor drive using various cables.
2	Take boundary temperature measurements of control board operating OUTSIDE THE CASE while idle. These can be found in Table 14.
3	Perform infrared thermography of control board while idle.
4	Extract surface temperatures of all components from infrared images.
5	Use iterative approach to determine component power dissipation simulating NATURAL CONVECTION CONDITIONS OUTSIDE MOTOR DRIVE using boundary temperatures measured in Step 2.
6	Take boundary temperature measurements of control board operating INSDIE THE CASE while idle. These measurements can be found in Table 11.
7	Use the same component power dissipation values found in Step 5 to perform a thermal analysis simulating NATURAL CONVECTION CONDITIONS INSIDE THE MOTOR DRIVE using the AVERAGE IDLE TEMPERATURE, found in Step 6, as the boundary temperature. The thermal profile generated in this step will be termed "control board idle" and will be used in the reliability assessment.
8	Use the same component power dissipation values found in Step 5 to perform a thermal analysis simulating FORCED CONVECTION CONDITIONS INSIDE THE MOTOR DRIVE using the AVERAGE LOAD (3.7A, 30 Hz) TEMPERATURE, found in Step 6, as the boundary temperature. The thermal profile generated in this step will be termed "control board load" and will be used in the reliability assessment.

Steps 1, 2 and 6 are described in the *Boundary Temperature Measurements* chapter, Steps 3 and 5 are described in the *Infrared Thermography* chapter and Steps 7 and 8 are described in the *Thermal Simulations in CalcePWA* chapter. It was verified through infrared testing that the power dissipation from individual components on the control board does not increase while the motor drive operates under a load. Therefore, the same power dissipation values used in the idle power level simulations were also used in the load power level simulations.

Many of the components on the power and connector boards did however exhibit load-dependent power dissipations, as discovered through testing. Although the steps taken to generate the thermal profiles for the control, power and connector boards were similar, two distinct processes are listed to make clear particular points. Table 10 lists the steps taken to generate the thermal profiles for both the Power and connector boards.

Table 10 Steps to generate thermal profile of power and connector boards

1	Remove case and setup power and connector boards to run outside motor drive using various cables to attach control board. Ensure fan is not connected.
2	Take boundary temperature measurements of power and connector boards operating OUTSIDE THE CASE while idle. These measurements can be found in Table 15.
3	Perform infrared thermography of power and connector boards while idle.
4	Extract all component surface temperatures from infrared images of Power and Connector board.
5	Use iterative approach to determine component power dissipation values simulating NATURAL CONVECTION CONDITIONS OUTSIDE THE MOTOR DRIVE while operating under the IDLE POWER LEVEL using boundary temperatures measured in **Step 2**. This is conducted for both the power and connector board.
6	Take boundary temperature measurements of power and connector boards operating INSDIE THE CASE while idle. These measurements can be found in Table 11.
7	Use the same power dissipation values found in **Step 6** to perform a thermal analysis simulating NATURAL CONVECTION CONDITIONS INSIDE THE MOTOR DRIVE using the average idle temperature, found in **Step 5**, as the boundary temperature. This is conducted for both the power and connector boards. The thermal profiles generated in this step will be termed "power board idle" and "connector board idle" and will be used in the reliability assessment.
8	Use the same power dissipation values found in **Step 6** to perform a thermal analysis simulating FORCED CONVECTION CONDITIONS INSIDE THE MOTOR DRIVE using the average idle temperature, found in **Step 5**, as the boundary temperature. This is conducted for both the power and connector boards. The thermal profiles generated in this step will be termed "power board load" and "connector board load" and will be used in the reliability assessment.
9	Repeat **Steps 2 – 8** WHILE OPERATING THE MOTOR DRIVE AT LOAD (3.7A, 30 Hz). In **Steps 3, 6 – 8** ensure that the boundary temperatures from the LOAD condition, rather than the idle condition, are used.

Steps 1, 2 and 6 are described in the *Boundary Temperature Measurements* chapter, Steps 3 and 5 are described in the *Infrared Thermography* chapter and Steps 7 and 8 are

described in the *Thermal Simulation in CalcePWA* chapter. Step 9 will be included in both sections as it is simply a series of repeated efforts.

Chapter 6: Boundary Temperature Measurements

Aside from specifying component geometry and materials in the CalcePWA model, two parameters needed to be determined through experimental efforts: component power dissipation and the ambient temperature surrounding each board. Due to the fact that the boards are housed within close proximity to one another, the heat dissipated from components on one board may affect the surface temperatures of components on a different board. This section describes the methods used to determine the ambient temperatures surrounding the boards, both inside and outside of the motor drive casing. Once determined, this data will be used in the CalcePWA model to perform thermal and reliability assessments of the VFD system.

This chapter along with the upcoming *Infrared Thermography* chapter will be used on conjunction with one another to develop a simulated thermal profile of the entire system. Testing of the motor drive will be conducted at two power levels, idle and 3.7A of current. This simulates a no-load condition and a full-load condition respectively.

6.1 Forced Convection – Operating the Boards Inside the Casing

This section will be divided up into two parts, one pertaining to the control board while the other pertaining to the power and connector boards. Both sections will describe the process used to obtain the boundary temperatures of the boards while operated within the drive case. All thermal measurements were taken using type T thermocouples with a data-logger to display the measurements.

6.1.1 Control Board

Six thermocouples were placed inside the motor drive to simultaneously measure different points surrounding the control board. An additional thermocouple was used to track the ambient temperature. All thermocouples inside the drive were placed approximately 1 cm. away from the surface of the control board or any other component. Figure 42 Schematic of control board thermocouple Locations shows a schematic of the thermocouple locations.

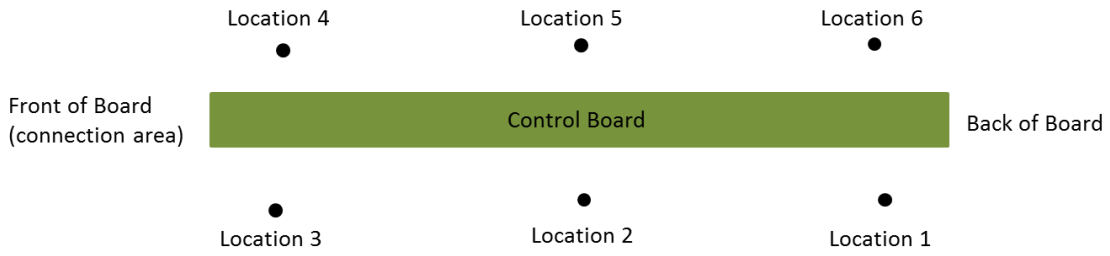

Figure 42 Schematic of control board thermocouple Locations

Standard electrical tape was used to hold the thermocouples in place. Their "wire-like" nature allowed them to be weaved into the motor drive through small crevices and air-vents in the case. Figure 43 Thermocouples measuring the bottom of the control board shows the thermocouples in Locations 1, 2 and 3 within the motor drive. This image does not include the control board because it had to be removed to properly place the thermocouples. Once placed, the control board was then reattached.

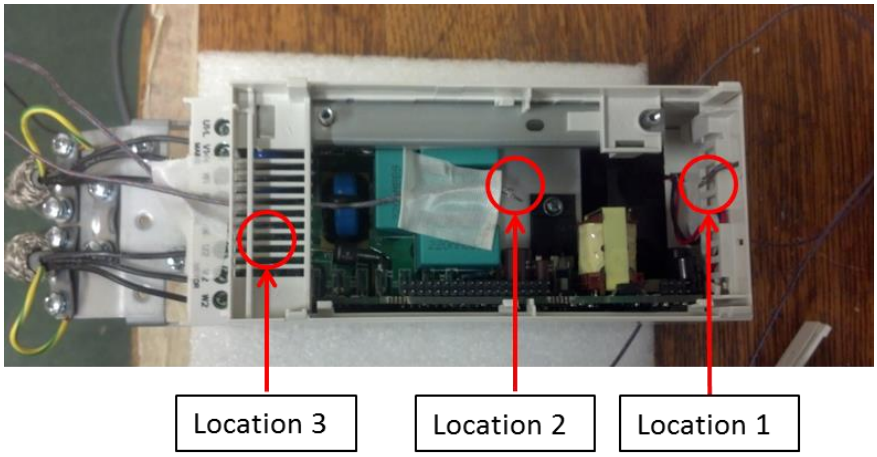

Figure 43 Thermocouples measuring the bottom of the control board

The thermocouples placed in Locations 4, 5 and 6 are shown in Figure 44.

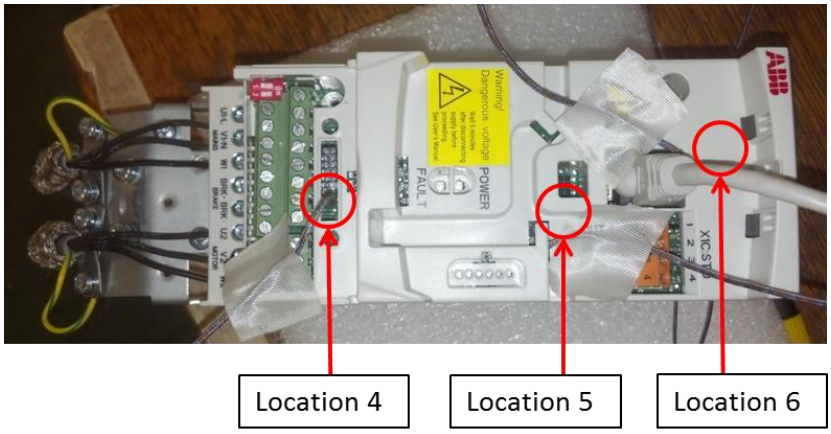

Figure 44 Thermocouples measuring the top of the control board

The testing was conducted so that four different current levels were tested (1.8A, 2.5A and 3.7A) at 20 and 30 Hz. Temperature measurements were also taken while the drive was idle, i.e. no current passing through to the motor but still powered on. The results from this test are shown in Table 11.

Table 11 Results from control board boundary temperature measurements

Temperatures °C		20 Hz			30 Hz		
	Idle	**1.8A**	**2.5A**	**3.7A**	**1.8A**	**2.5A**	**3.7A**
Ambient	24.2, 24.5	24.4	25.5	25.9, 26	26.0, 26.1	25.7, 26.2	26.4, 26.5
Avg. Ambient	24.4	24.4	25.5	26.0	26.1	26.0	26.5
Loc. 1	44.1	25.8	26.3	26.8	27.1	27.3	27.5
Loc. 2	48.9	26.1	26.3	26.9	27.5	27.7	28.2
Loc. 3	33.9	24.6	24.7	25.0	26.2	26.1	26.2
Loc. 4	33.6	24.9	25.2	25.9	26.4	26.1	26.5
Loc. 5	43.4	25.6	26.3	27.0	27.2	27.0	27.3
Loc. 6	35.6	25.3	25.9	26.7	26.9	27.0	27.1
Range	15.3	1.5	1.6	2.0	1.3	1.6	2
Average	39.9	25.4	25.8	26.4	26.9	26.9	27.1
Change from Ambient to Avg.	15.6	1.0	0.3	0.4	0.8	0.9	0.7

An average temperature, shown in Table 11 as the row labeled “Average”, was calculated by averaging the six thermocouple measurements. An ambient temperature reading was taken right before recording the temperatures from the data logger and right after as well. These two measurements were averaged to produce an average ambient temperature. The bottom row indicates that regardless of the current, frequency and fluctuations in room temperature there is little difference between the ambient temperature and the temperature surrounding the control board. However, the motor drive experienced significant heating while idle. Prior to conducting this test it was hypothesized that as the load increased on the motor drive, the temperatures within the drive would increase accordingly. This was predicted based on the assumptions that the fan is continuously running throughout all power levels.

However, through testing it was discovered that the fan only runs while the VFD is powering the motor. While idle, the fan does not run which severely limits the drive’s ability to cool the components. While idle, natural convection is the only mechanism

cooling the components. Furthermore, the range of temperatures taken at any power level or frequency (not including the idle condition) is small. This can be explained due to the fact that the fan induces chaotic airflow surrounding the components, nearly eliminating thermal gradients in the air. Likewise, under idle conditions hotter air regions could more easily form. This can be seen by comparing the temperatures of Location 2 and Location 4 under the idle condition in Table 11.

6.1.2 Power and Connector Boards

The same process used to obtain the surrounding temperatures of the control board was used to obtain the surrounding temperatures of the power and connector boards. Temperatures for both boards were measured simultaneously due to their close proximity with respect to one another. As such, 12 thermocouples, termed "Location 1" through "Location 12", were used to take measurements including one to keep track of the ambient temperature (Location 4). Much like the control board, the thermocouples were placed approximately 1 cm. from the surface of the board. An exception to this exists for Location 3 and Location 5 due to geometrical limitations imposed by the drive case. They are placed approximately 0.5 cm away from the surface of the board. Of the 12 thermocouples, Location 1, Location 7 and Location 9 were strategically placed so that data could be used for both boards. Figure 45 Thermocouple locations surrounding the power board displays the top side of the power board with the locations of the thermocouples. The placement of Location 3 and Location 5 exist on the back side of the board.

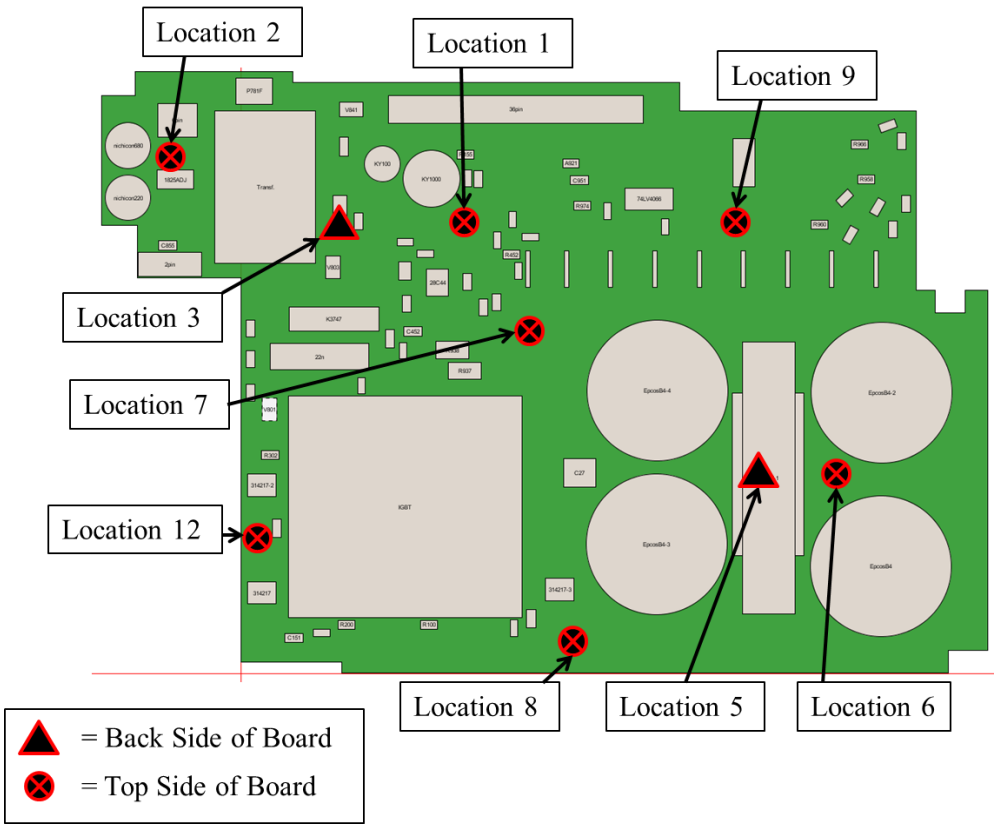

Figure 45 Thermocouple locations surrounding the power board

Figure 46 displays the thermocouple placement surrounding the connector board. As stated previously Location 1, Location 7 and Location 9 were also used on the power board. Location 10 and Location 11 are used solely for the connector board and all thermocouples were placed approximately 1 cm away from the surface of any board.

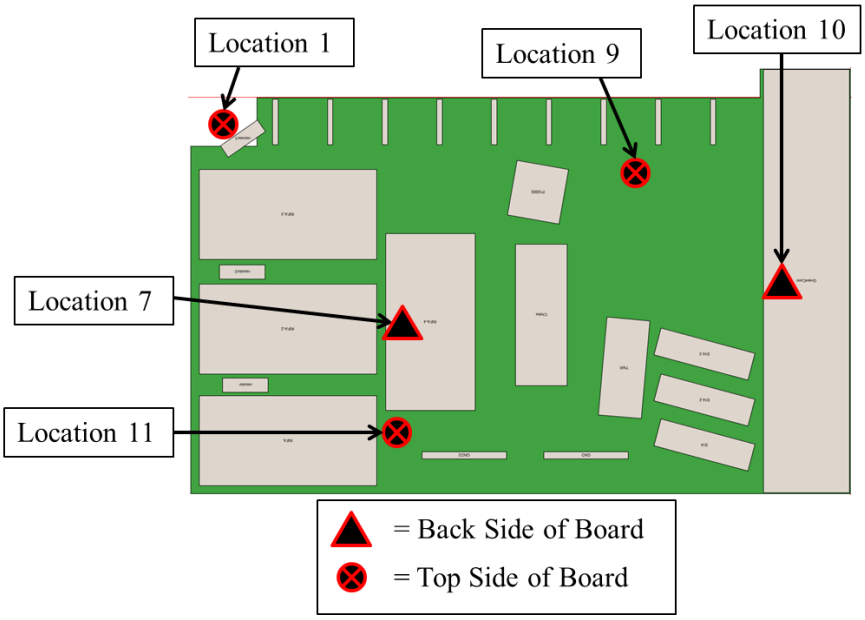

Figure 46 Thermocouple locations surrounding the connector board

In order to place all 12 thermocouples into the motor drive, the fan-door shown in Figure 47 had to be taken out and taped back into place. This was conducted so that airflow could be maintained in its original manor. Inside the drive, the thermocouple wires were bent in such a fashion so that contact with any component or the fan was avoided.

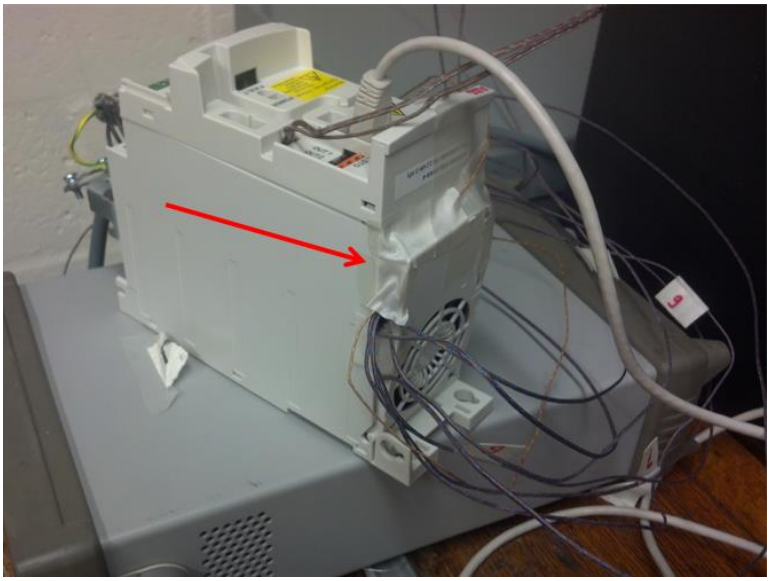

Figure 47 Thermocouples entering motor drive through fan door

Testing of the power and connector boards was conducted in the same manner as the control board. Table 12 shows the results from the power board boundary temperature measurements. The blue highlighted rows indicate locations that were also included in the connector board measurements while the orange highlighted rows indicate the locations that were solely used for the connector board.

Table 12 Results from power board boundary temperature measurements

Temperature °C			20 Hz			30 Hz		
	Idle		1.8A	2.5A	3.7A	1.8A	2.5A	3.7A
Ambient (Loc. 4)	25.0, 24.9		25.2	25.2	24.6, 24.9	24.9, 25.0	25.0	25.2
Avg. Ambient	25.0		25.2	25.2	24.8	25.0	25.0	25.2
Loc. 1	45.8		25.7	25.6	24.8	25.3	25.9	26.1
Loc. 2	53.7		29.8	29.7	28.7	29.3	29.7	29.8
Loc. 3	38.9		28.2	28.5	28.5	28.1	28.6	29.3
--	--		--	--	--	--	--	--
Loc. 5	40.1		29.5	29.8	30.2	29.3	29.9	31.3
Loc. 6	37.0		25.3	25.7	25.2	25.7	26.2	26.8
Loc. 7	39.0		27.4	28.2	29.2	27.7	28.7	30.7
Loc. 8	38.2		27.4	27.9	28.5	27.6	28.2	29.7
Loc. 9	40.0		25.6	25.4	25.0	25.5	25.7	26.3
Loc. 10	These locations were solely used on the connector board							
Loc. 11								
Loc. 12	35.2		29.1	29.6	30.3	28.9	29.8	31.3
Average	40.9		27.6	27.8	27.8	27.5	28.1	29.0
Change from Ambient to Avg.	15.9		2.4	2.6	3.0	2.5	3.1	3.8

Table 13 shows the results from the connector board testing.

Table 13 Results from connector board boundary temperature measurements

Temperature °C			20 Hz			30 Hz		
	Idle		1.8A	2.5A	3.7A	1.8A	2.5A	3.7A
Ambient (Loc. 4)	25.0, 24.9		25.2	25.2	24.6, 24.9	24.9, 25.0	25.0	25.2
Avg. Ambient	25.0		25.2	25.2	24.8	25.0	25.0	25.2
Loc. 1	45.8		25.7	25.6	24.8	25.3	25.9	26.1
Loc. 7	39.0		27.4	28.2	29.2	27.7	28.7	30.7
Loc. 9	40.0		25.6	25.4	25.0	25.5	25.7	26.3
Loc. 10	35.5		25.0	25.1	25.0	25.3	25.6	26.2
Loc. 11	37.1		25.2	25.0	24.7	25.1	25.3	25.9
Average	39.5		25.8	25.9	25.7	25.8	26.2	27.0
Change from Ambient to Avg.	14.5		0.6	0.7	0.9	0.8	1.2	1.8

Similarly to the control board, both the power and connector boards have idle operating temperatures significantly higher than the temperatures experienced while under load. Furthermore, the data shows that as the load increases at 20 Hz and 30 Hz the average temperature difference between the ambient and the air surrounding both boards increase slightly. This is different than the control board measurements where there appears to be no qualitatively significant temperature rise in relation to power level. This may be due to the fact that the power board contains the power switching module and the Si MOSFET, both which dissipate more heat due to losses at increased power levels. Although future tests should be conducted to verify if this increase is quantitatively significant, this observation is nonetheless important to note.

For each power level the average surrounding temperature of the power and connector boards were determined by computing the average of the thermocouples used, nine for the power board and five for the connector board. Like the control board measurements, the fluctuations in the ambient temperature were factored out from the analysis by subtracting the average ambient temperature from the average temperature surrounding the board. This research is focused towards the methodology implemented, therefore statistical analysis of the boundary temperature thermal results falls outside the scope of this project.

6.2 Setting up VFD for IR Thermography and Temperature Measurements

The packaging and locations of all three boards in the motor drive were manipulated to access all components for thermal imaging. Furthermore, due to the nature of the

processes as described in Table 9 and Table 10 a natural convection environment needed to be created. This was performed by eliminating the airflow restraints imposed by the motor drive casing and disabling the fan for certain measurements.

Figure 48 shows how sets of wires were used to run the control board autonomously from the rest of the motor drive. The infrared camera is also shown to better depict the setup for infrared imaging.

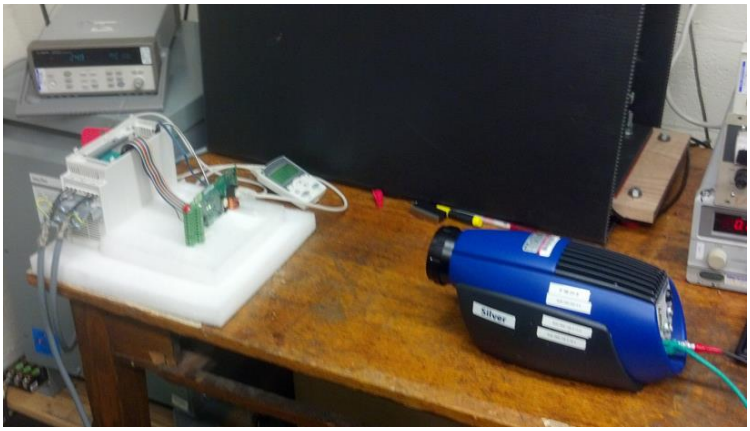

Figure 48 Control board setup for IR thermography

Two sets of wires were used, one with 36 wires to link the 36-pin connectors and one with 6 wires to link the 6-pin connectors. The wires were 20 cm long and had male-to-female connectors. Figure 49 shows the how the removal of the case provided access to the power board for imaging.

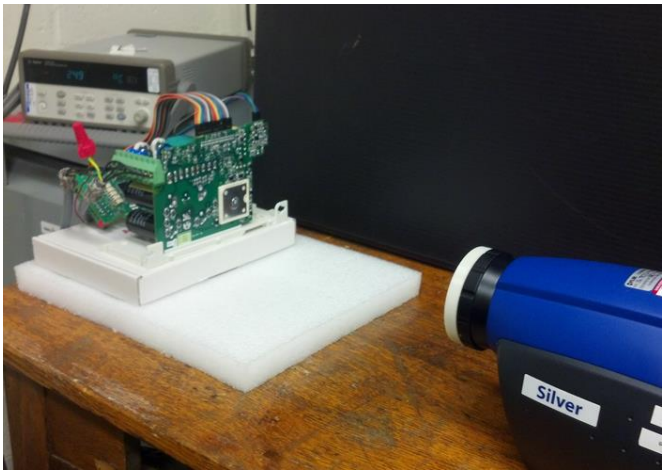

Figure 49 Power board setup for IR thermography

Furthermore although the case was removed and the fan was disconnected to best simulate a natural convection environment, the control board continued to operate through a set of wires. This served two purposes, both to provide a direct view of the connector board as shown in Figure 50, and to remove physical barriers that may trap heat.

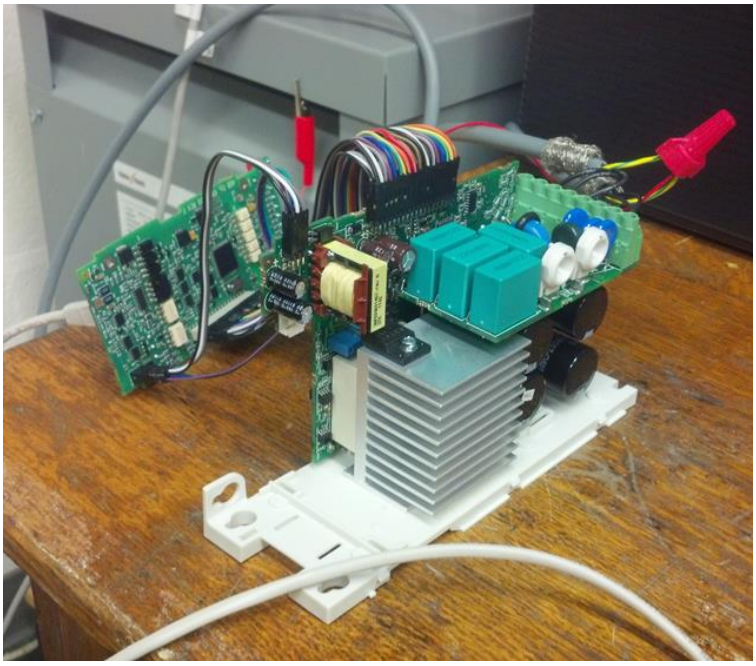

Figure 50 Case removed, direct view of connector board

By removing the case and setting up the boards in the fashion shown, component surface temperatures could be measured via infrared imaging and boundary temperatures of all three boards could be measured with thermocouples.

6.3 Boundary Temperature Measurements – Natural Convection Environment

Once removed and set up outside the case, boundary temperature measurements were taken for all three boards. These were then used in the iterative process (described in Step 5, Table 9 and Table 10) to determine component power dissipation values. Figure 51 shows the two thermocouples used to measure the surrounding temperature change due to heating of the control board.

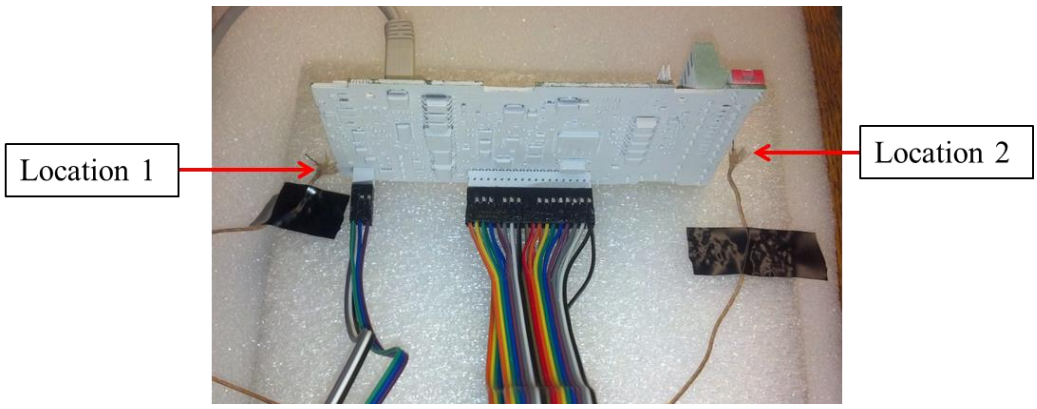

Figure 51 Control board natural convection boundary temperature measurements

In this image, the control board is covered with a boron nitride spray. Boron nitride was initially used during infrared measurements to create a uniform surface emissivity across all components. After testing began it was discovered that the high conductivity of the boron nitride powder created an undesired heat spreading effect. While the emissivity among all components was unified, the infrared camera was not able to differentiate components based upon their thermal signatures. Therefore another method, described later in this report, was implemented to determine the surface emissivity of components.

Thermal measurements of the control board were taken while the motor drive was operating at the full-load power level. Measurements were only taken at this power level based on the assumption that the control board does not have components with load-dependent power dissipation. Prior to taking measurements, the motor drive was held at this power level for ten minutes to allow all components to reach their steady state temperature. The control board temperature could be monitored using a thermistor built into the board. Furthermore, only two thermocouples were used because it was predicted that the temperature change due to component power dissipation would be small relative to the ambient temperature. Table 14, which shows the results from this test, reveals that the prediction was correct.

Table 14 Control board boundary temperature measurements - outside case

	Temperatures °C
Location 1	28.0
Location 2	26.0
Average	27.0

An average of the two measurements was calculated and used in the thermal simulations. Throughout all thermal boundary measurement tests the ambient temperature varied between 24.0°C – 26.0°C. For all thermal simulations conducted in this project, it was assumed that the base ambient temperature was 25°C. Therefore, boundary temperatures of the boards were simulated using the average measured temperatures without adjusting for ambient temperature deviations.

Figure 52 shows the thermocouples used to measure the boundary temperatures of the power and connector boards. Unlike the control board, the power and connector boards

were hypothesized to contain components with load-dependent power dissipation. As such, more thermocouples were used to provide more data points to calculate an average value.

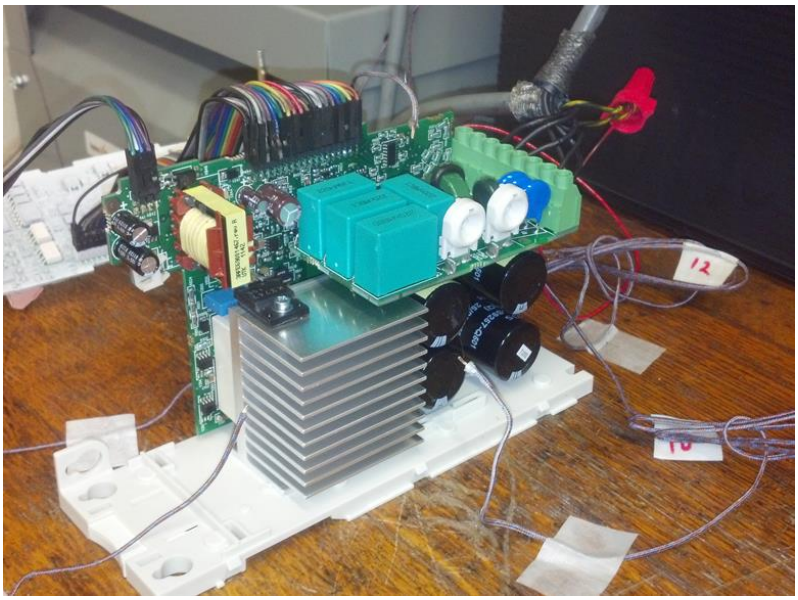

Figure 52 Power and connector board natural convection boundary temperature measurements

A schematic showing the locations where the thermocouples were placed is shown in Figure 53. The tips of the thermocouples were placed approximately 1 cm. away from the boards and components.

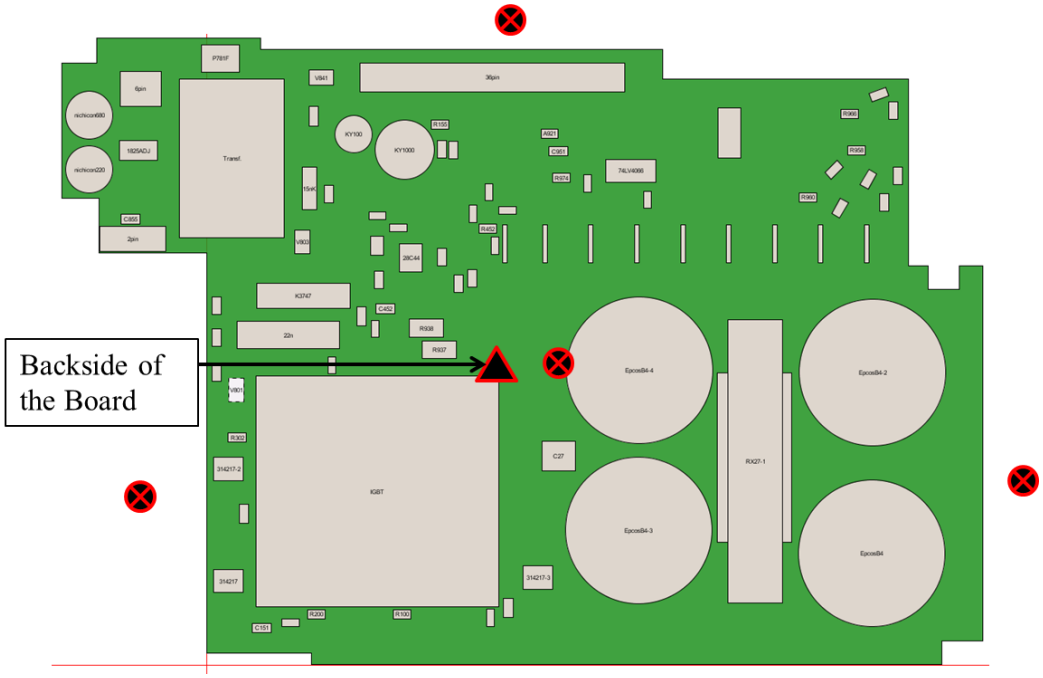

Figure 53 Schematic showing thermocouple locations - outside case

Measurements were taken while the motor drive was idle and while operated at full-load. It was assumed that the motor drive would reach its steady state temperature within 10 minutes of operating at a particular power level. This was validated by monitoring the IGBT temperature through an internal monitoring mechanism built into the VFD. It was discovered that the motor drive reached steady state temperature at the idle power level within 10 minutes. However, it was also discovered that the IGBT never fully reached steady state temperature while operating under load because the fan was not connected to cool the system down. In fact, the drive tripped due to overheating prior to reaching steady state temperature. Therefore, the boundary temperature measurements of the power and connector boards, along with the IR images of these boards, were taken while the IGBT temperature was between 100°C - 110°C. Table 15 shows the results from these tests.

Table 15 Power and connector board boundary temperature measurements - outside case

	Idle	**Full Load**
Temperatures °C	25.5	25.8
	26.2	26.7
	26.3	29.6
	26.9	31.6
	26.0	27.0
Average	**26.2**	**28.1**

This test reveals that the power and connector boards contain components that have load-dependent power dissipations. This explains the increase in boundary temperature between the idle and full load conditions.

6.4 Discussion and Analysis of Boundary Temperature Measurements

There were essentially two sets of boundary temperature measurements conducted. One consisted of measuring the boundary temperatures of each assembly inside the case and the other consisted of taking these measurements outside the case. The first of these showed that the temperatures inside the case changed with the load. Specifically, it was seen that the surrounding temperature of the control circuitry was highest while the drive was idle rather than at full load. This was unexpected but also indicated the importance of a reliable fan to provide cooling. Future studies could be conducted to identify the importance of the fan and how system performance could be affected in cases such as a complete fan failure or in case of degraded fan performance.

Chapter 6: Infrared Thermography

Infrared thermography was used to obtain surface temperatures of each component on all boards. These values were then used to derive power dissipation using the CalcePWA thermal simulation software. Fourier's Law of thermal resistance, described the Equation below, shows that the amount of power dissipated can be determined if the surface temperature, the junction-to-case thermal resistance and the junction temperature are known. P_D is the power dissipated, T_j is the junction temperature, T_c is the case or surface temperature and θ_{jc} is the junction-to-case thermal resistance.

$$P_D = \frac{T_j - T_c}{\theta_{jc}}$$

However, of the three unknowns in Equation 4 only the case temperature could be measured. The junction-to-case thermal resistance was estimated to be 10 °C/W for all components on the control board. The components on the control board were relatively the same size and thus it was assumed that they all have similar abilities to dissipate heat. For the power and connector boards however, the junction-to-case thermal resistances were estimated based upon component size. This was due to the fact that the types and sizes of components on these boards varied considerably and therefor different values should be used. The assumed junction-to-case thermal resistance values for each component can be found in the Appendix of this report. P_D will be extracted from the CalcePWA thermal simulations, T_C will be measured using the IR camera and thus θ_{jc} will only affect the junction temperature. Due to the fact that this study does not utilize the junction temperature for any of the reliability simulations, accurate thermal resistance values are not necessary. Accurately determining thermal resistance values for all components is a process which falls outside the scope of this project. Much work has

been done in this field [38] but in order to proceed through this research within the time constraints of the project, the thermal resistance values were inputted into the CalcePWA model uniformly.

6.1 Basic Infrared Thermography Theory

All objects above absolute zero continuously emit electromagnetic radiation [39]. The amount of radiation an object emits is a strong function of temperature and can be modeled by Equation 5,

$$Q = \varepsilon \sigma A T^4 \tag{5}$$

where Q is the heat transfer per unit time (in unit Watts), ε is the emissivity of the surface, σ is Plank's constant, A is the surface area and T is the absolute temperature in Kelvin. Emissivity is a dimensionless material property and describes a materials ability to emit radiation.

An infrared camera works by capturing radiation patterns emitted by objects and converts them into visible images. A lens focuses the radiation into a detector that outputs electrical signals. These response signals are then converted into a digital picture where various temperatures are represented by different shades of grey or different colors depending on the processing software. This enables the user of an IR camera to "see" the temperature profile of an object [40].

6.2 Capturing Infrared Images of Assemblies

A FLIR Silver SC series infrared camera was used to perform the infrared measurements. This camera has a rated accuracy of (+/-) 1°C, given that the emissivity of the object is known, and has a rated operating range of 5°C - 300°C. Altair, which is a processing software developed by FLIR, was used to extract the surface temperatures of components from the images.

Four sets of images were taken: the control board while idle, the control board while operating at full-load, the power and connector boards while idle and the power and connector boards while operating at full-load. Within each of the sets, numerous images were taken due to the fact that one image could not capture all components. Especially on the power board, larger components prevented smaller components from being visible. As such, images were taken at various angles with respect to the boards to measure all components.

6.2.1 Calibrating Emissivity of Components

Equation 5 states that accurately determining surface temperature using IR imaging is largely dependent upon the accuracy of the surface emissivity. Although the component materials were assumed in the CalcePWA model, factors such as the conformal coating on top of the components were not included in the model but affect emissivity. As such, using charts which contain emissivity values for different materials could not be used. Therefore a method was developed to determine the emissivity of all components.

It is known that black electrical tape (3M Scotch Super 33+) has an emissivity of 0.95 [41][42]. The process consisted of calibrating the emissivity of each component to the emissivity of the black electrical tape. In order to do this a strip of tape was first placed and positioned next to the components of interest so that the view from the IR camera could include the components and tape. Given that the motor drive was off, it was assumed that the temperature of the tape and the temperature of the components were the same. Next, a point measurement was taken of the component and a point measurement was taken of the tape. In the software, the user has the ability to alter the emissivity of the point measurement and witness the corresponding change in measured temperature. The emissivity of the tape was set to 0.95 and the emissivity of the component was altered until both temperatures were equal. This process enabled the emissivity of each type of component to be determined.

Initial emissivity calibrations indicated that not all components of the same material exhibited the same emissivity. Further investigation into literature revealed that factors such as surface roughness, viewing angle and viewing distance all affect the accuracy of the calibration efforts [43]. However, it was determined after determining the emissivity of all components that all emissivity values fell within the range of 0.8 – 0.90. Therefore, the temperature of each component was measured using an emissivity of 0.8 and an emissivity of 0.90, producing a range containing the actual surface temperature. As an example, Figure 54 and Figure 55 show the surface temperature of the DSP with emissivity set to 0.8 and 0.9 respectively. These images show that the actual surface temperature range for the DSP lies between 52.3°C and 54.3°C.

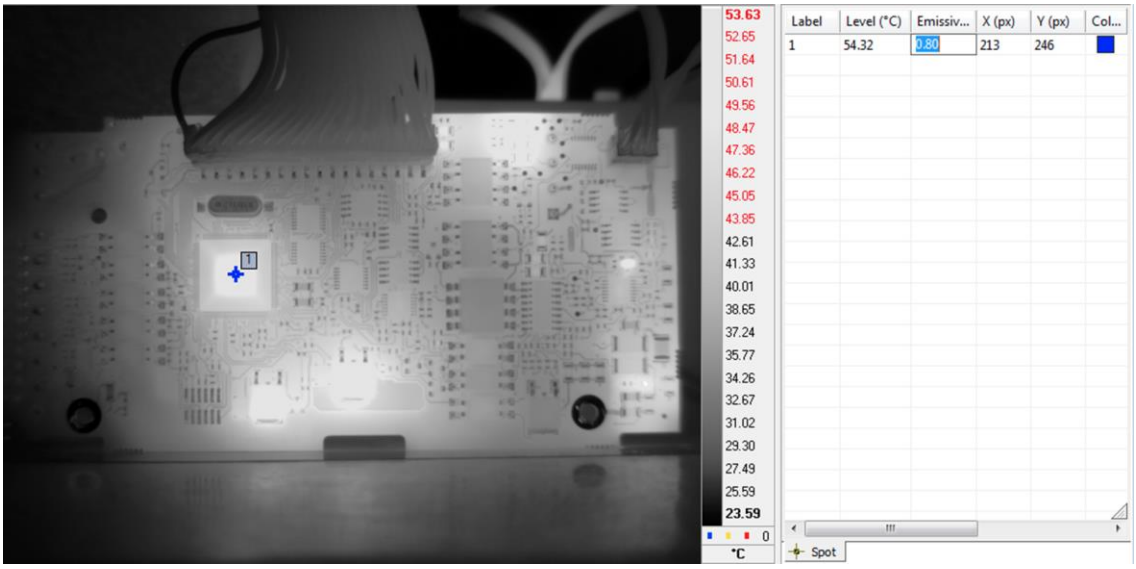

Figure 54 IR image: surface temperature of DSP, emissivity = 0.8

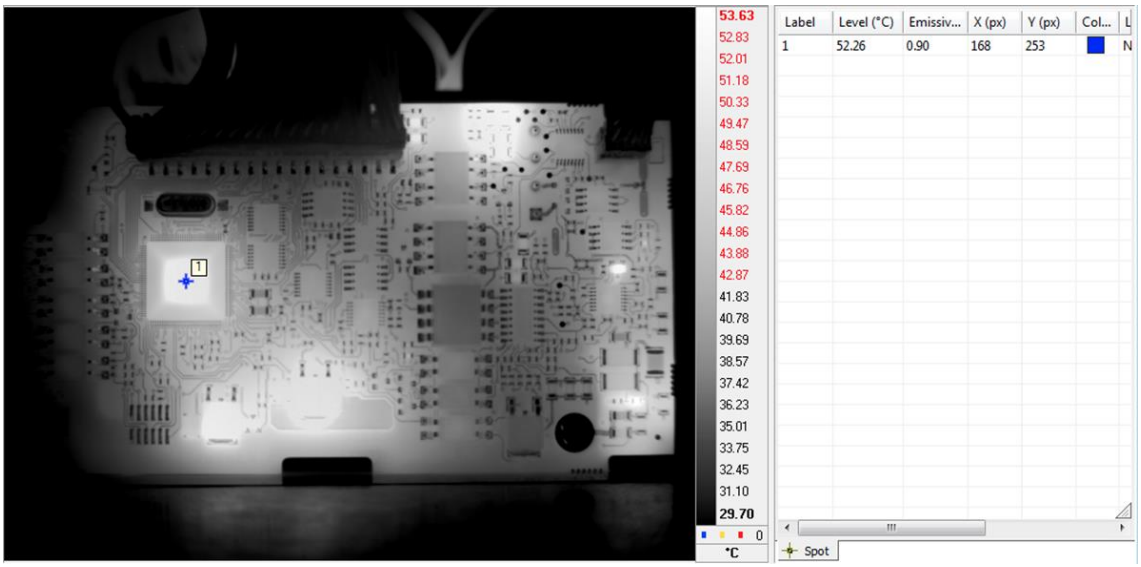

Figure 55 IR image: surface temperature of DSP, emissivity = 0.9

While this method of performing infrared thermography and calibrating component emissivity provides a sound first order approach, further revisions of this method could include a more accurate approach for determining emissivity. Special pyrometers and emissivity calculators exist that provide a more accurate means for emissivity measurements [44]. This will be discussed the *Future Work* section of this report.

6.2.2 Using Software to Analyze IR Images

Two types of measurements could be taken using the Altair software, a point measurement and an area measurement. The point measurement technique, shown in Figure 54 and Figure 55, allows the user to determine the surface temperature of a single point once the emissivity is set appropriately. The point measurement technique is beneficial when measuring smaller components such as resistors, capacitors and small PEM devices. However an area measurement, shown in Figure 56, is more useful when taking thermal measurements of larger components.

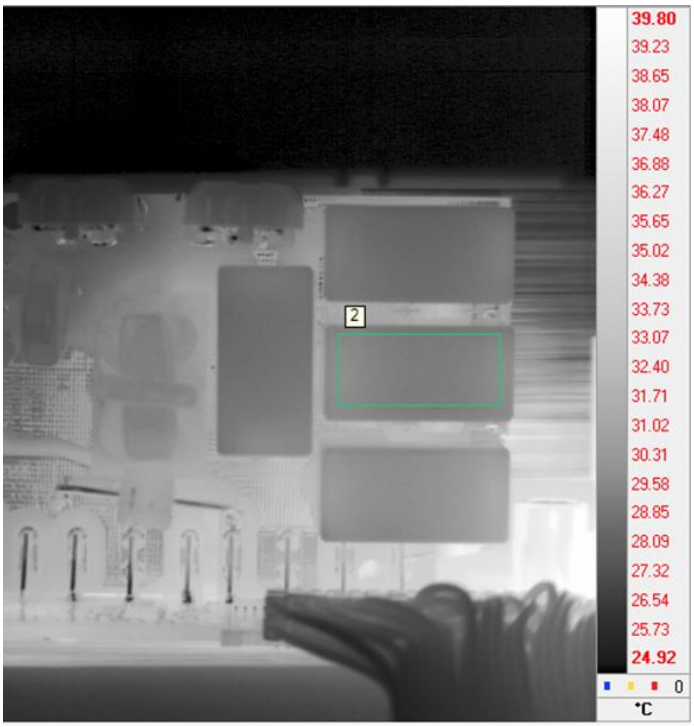

Figure 56 IR image: displaying area measurement

This image shows that the surface of a film capacitor located on the connector board has a mean temperature of 31.5°C, with maximum and minimum temperature of 32.2°C and 31.0°C respectively. Furthermore, averaging the surface temperature over an area can produce more accurate measurements. “Phantom” temperature gradients occasionally

occur over larger areas being measured due to reflection variations across the surface [45]. Averaging the temperature over the area may reduce the impact of these “phantom” temperature gradients.

6.2.3 Control Board

Figure 57 displays the infrared profile of the back of the control board while the system is under full load. To show that there is negligible temperature rise in the control board between the idle (Figure 54) and full-load condition, the surface temperature of the DSP is assessed.

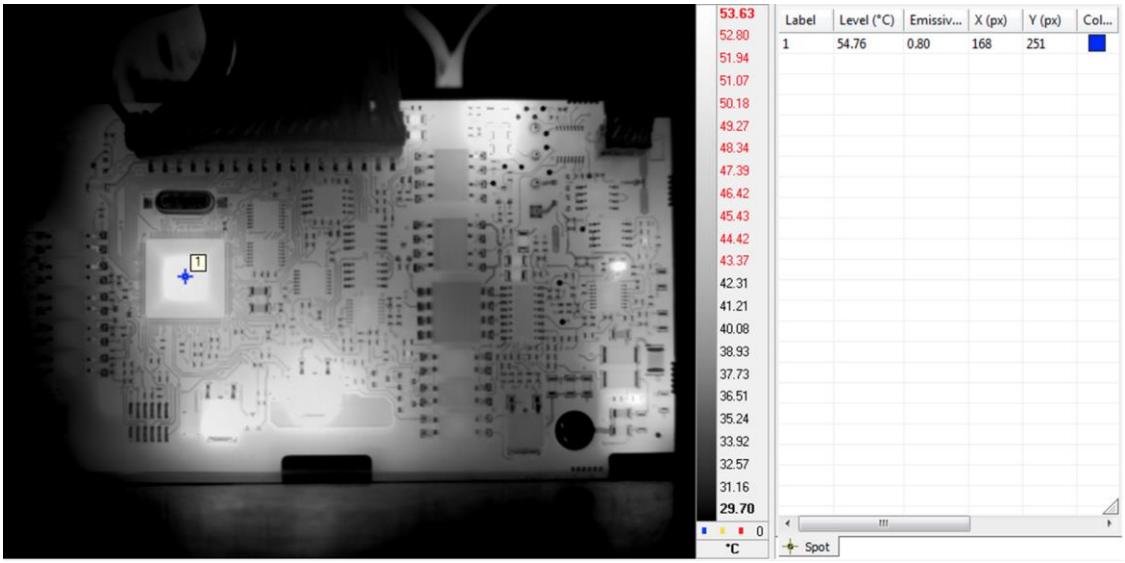

Figure 57 IR image: back of control board

The surface temperature of the DSP is 54.3°C while the system is idle and 54.8°C while the system is under load. The small difference can be attributed to measurement error and changes in ambient temperature between measurements. While this is only one component on the control board, all the components were measured under the idle and load conditions and revealed very small (less than 2°C) temperature differences. Due to the fact that this small difference can be accounted for by the +/- 1°C accuracy of the IR

camera and the 2°C ambient temperature range of the testing room, it was assumed that the surface temperatures of all components are independent of the load. The temperatures of all 139 components on the control board were assessed with the emissivity set to 0.8 and 0.9. These temperatures were recorded manually.

6.2.4 Power Board

Unlike the control board, the power board contains components that get hotter under the full load condition. Figure 58 shows a number of the larger sized and higher powered components on the power board while the motor drive is idle.

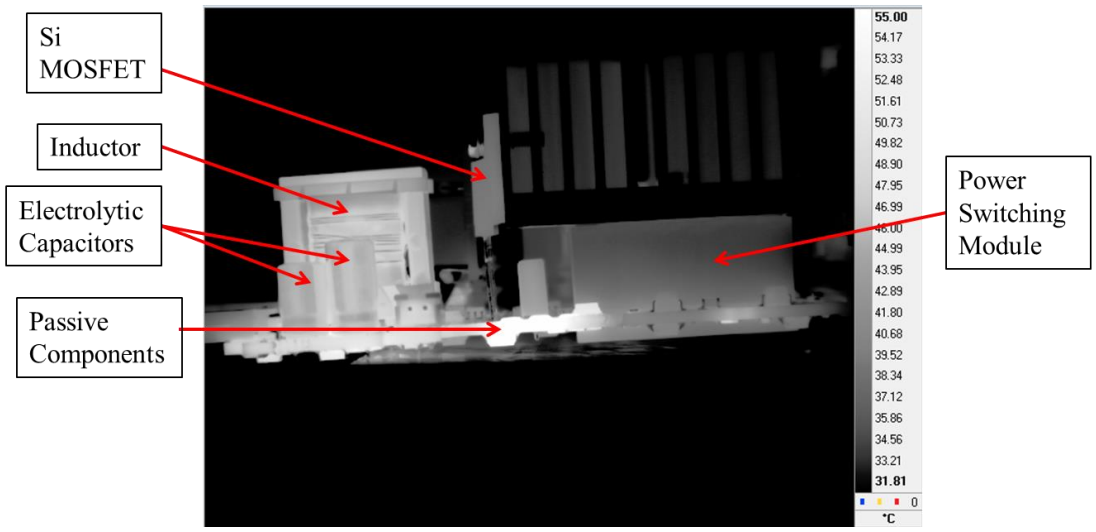

Figure 58 IR image: power board idle

In this image, the power switching module and the Si MOSFET are relatively inactive and do not dissipate much heat. Comparatively, the passive devices are the hottest components. However, this changes when the motor drive is operated at full load, shown in Figure 59.

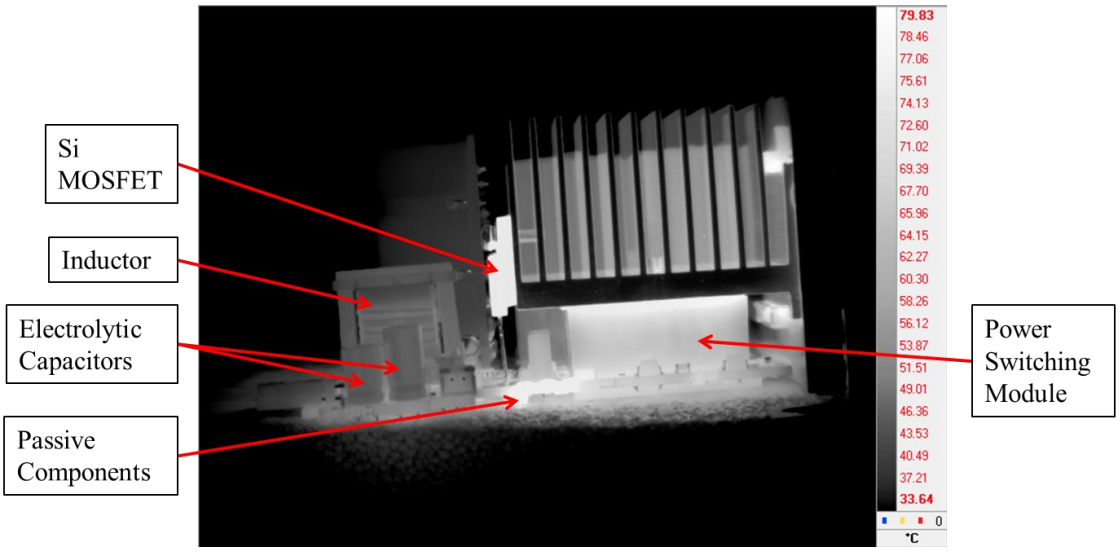

Figure 59 IR image: power board full-load

While the system is running at full load, the Si MOSFET and the power switching module become the dominant heat dissipating components. Furthermore, a heat sink is directly attached to both of these components in order to channel heat away from other components.

The passive components shown in Figure 58 and Figure 59 consistently dissipate a significant amount of heat regardless of the load. However, once the surface temperatures of all components were taken it became apparent that most components on the power board experienced a temperature rise between the idle and full load condition. While the scope of this project covers how to decouple the heating effects experienced between assemblies in the VFD, decoupling the heating effects of components on the same assembly falls outside the scope of this project. The assumptions that deal with extracting power dissipation values from the IR images will be discussed in later sections.

6.2.5 Connector Board

Figure 60 shows the connector board while the motor drive is idle.

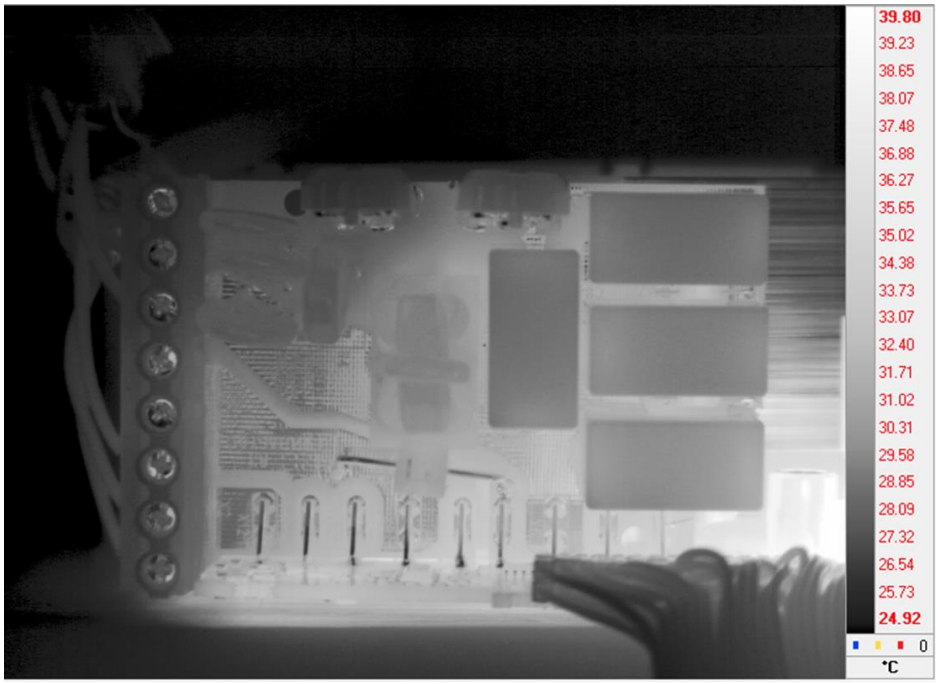

Figure 60 IR image: connector board idle

This image makes clear that the connector board does not contain components that dissipate significant heat. Furthermore it can be seen that a significant thermal gradient appears across the board that is most likely caused by the larger heat dissipating components, such as the transformer and passive devices, on the power board. Figure 61 shows the connector board while the drive is running at full load.

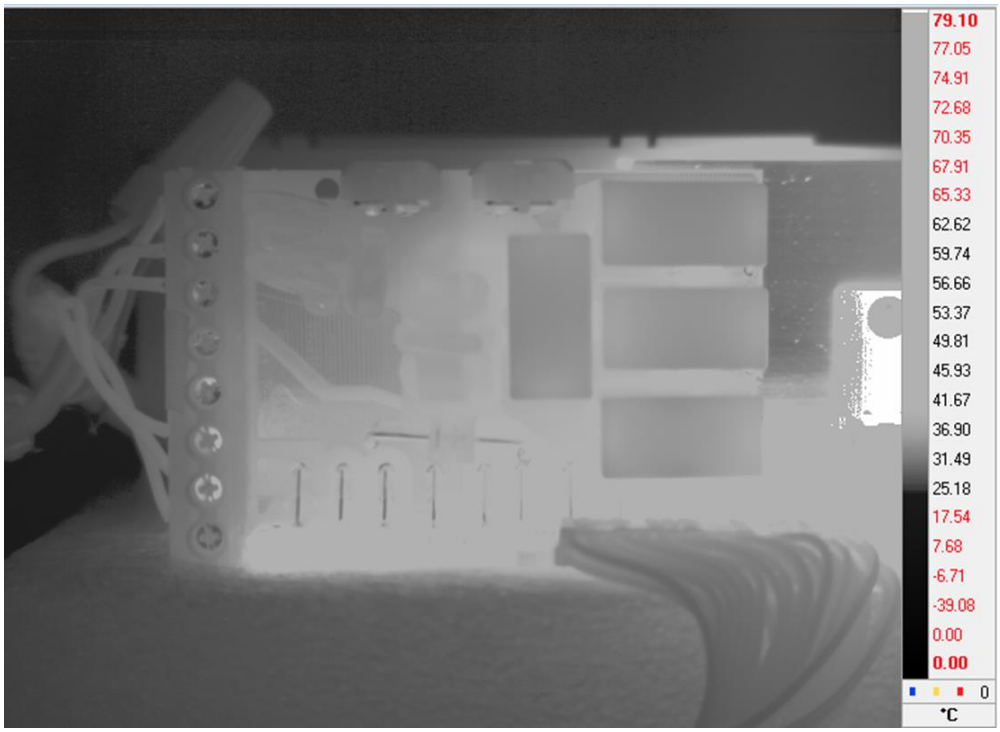

Figure 61 IR image: connector board load

An overall increase in surface temperature is seen across all components. Due to the heating created by the Si MOSFET and the power switching module, the air surrounding the connector board becomes hot enough that differentiating individual components for measuring becomes difficult. This most likely reveals that any increase in power dissipation from these components is negligible compared to the increase in power dissipation exhibited by the larger components on the power board.

6.3 Extracting Component Power Dissipation from IR Images

Once the thermal profile of all three boards was assessed and the boundary temperatures surrounding the boards were measured, power dissipation values could be extrapolated for each component. This process was an iterative approach which used the CalcePWA thermal analysis tool as the primary vehicle for these calculations. This section will

describe each step in the process of determining the power dissipation exhibited by the components. Figure 62 displays a diagram of the methodology.

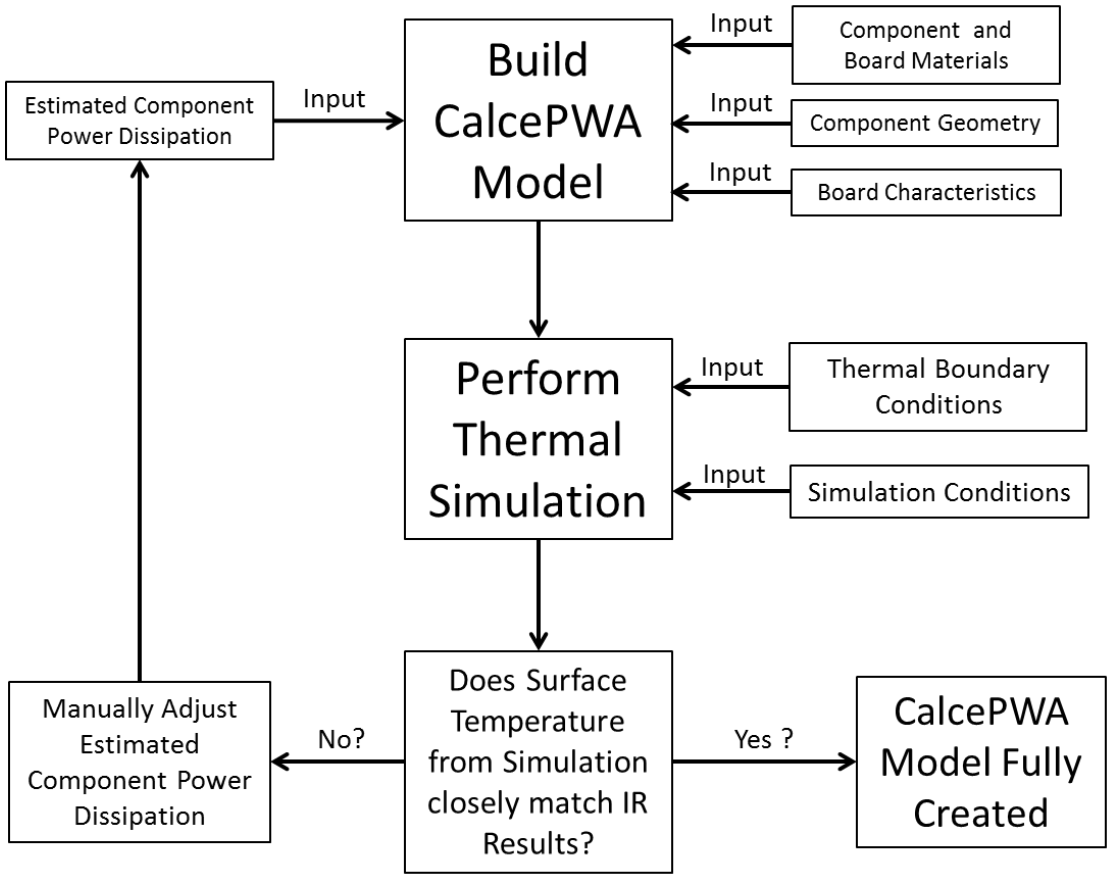

Figure 62 Iterative process for determining component power dissipation

The first step in the process was to build a CalcePWA model of all three boards, capturing component and board material, component geometry and PCB characteristics. This was previously described in the report. However, the model must also include the amount of power each component dissipates. Due to the fact that these values were unknown, an initial estimation was inputted into the model based upon component size, type and information from data sheets.

The next step in the process was to perform thermal simulations using the CalcePWA thermal analysis tool. Infrared thermography of all three boards was conducted while the boards were operated outside of the case and without a fan. This emulated a natural convection environment. Therefore, the thermal simulations were conducted under natural convection conditions. As an example this section will describe how the power dissipation of the DSP, located on the control board, was determined. Figure 63 shows a screenshot of the control board in the CalcePWA thermal analysis tool.

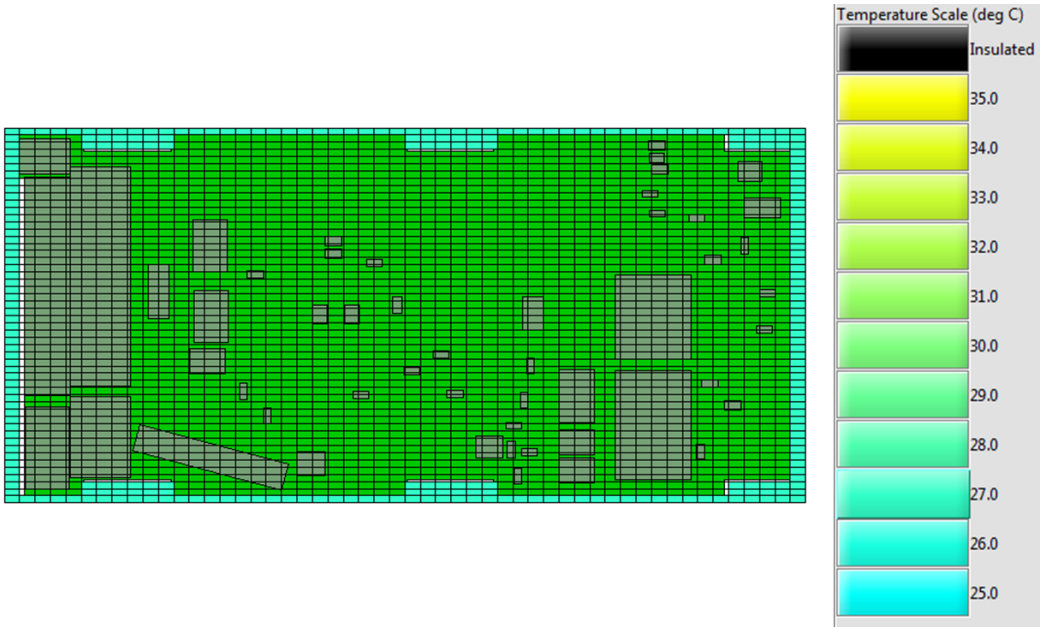

Figure 63 Screenshot of control board in CalcePWA thermal analysis tool

Thermal boundary measurements taken of the control board operating outside the case indicated that the surrounding temperature was 27.0°C. This was specified in the simulation as indicated by the blue ring surrounding the board in Figure 63. Furthermore, a variety of other parameters were specified to simulate natural convection conditions. Figure 64 shows screenshots of the various parameters. The thermal analysis tool also provides a method to manually change the amount of power each component dissipates.

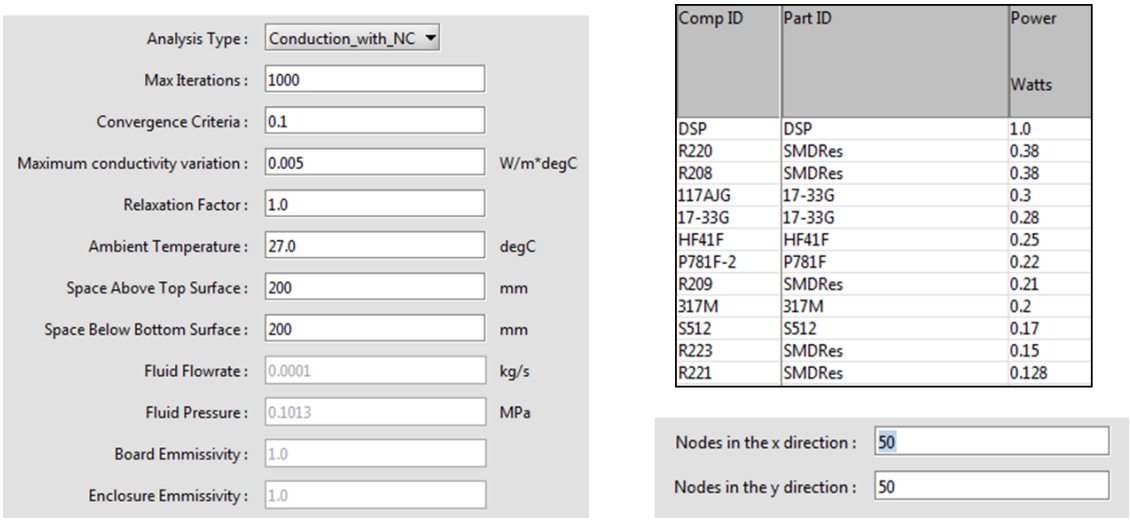

Figure 64 Specified parameters in CalcePWA thermal analysis tool

The analysis type was set to "Conduction with Natural Convection", simulating conduction within the board and components, but natural convection between the board and components and the surrounding air. The number of iterations and convergence criteria are properties of the finite element solver. These were assumed to be 1000 and 0.1 respectively for all thermal simulations. Maximum conductivity and relaxation factor are application constants and were assumed to be 0.005 W/m°C and 1.0 respectively for all simulations. Ambient temperature was specified as 27.0°C, as this was the measured boundary temperature. "Space Above" and "Space Below" signify airflow boundaries. Due to the fact that the control board was operated outside of the case, these values were large and were specified as 200 mm. Finally, the initial estimation for the amount of power the DSP dissipates was 1.0 Watt.

The thermal analysis tool was run and Figure 65 displays the results, showing the thermal profile of the backside of the control board.

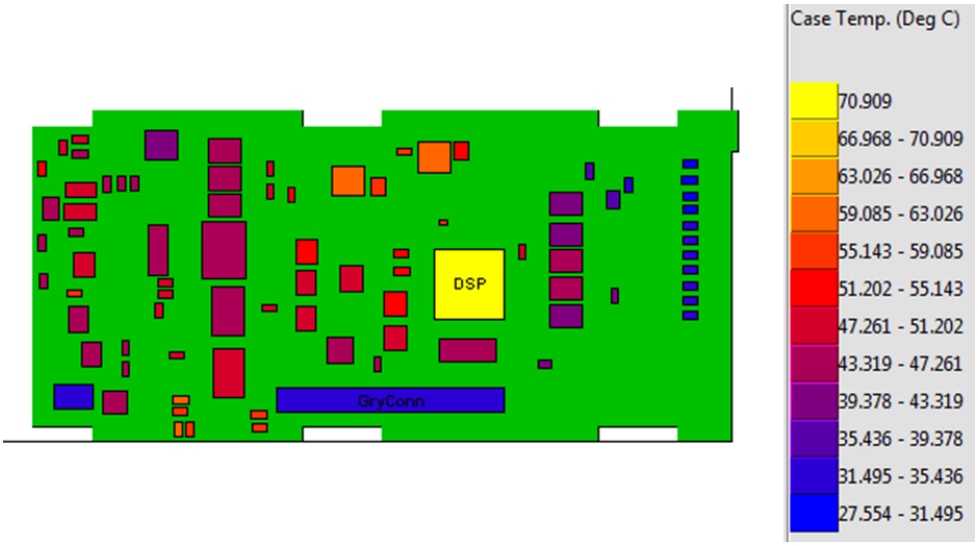

Figure 65 Thermal profile of control board, DSP = 1W

This image shows the DSP exhibits a surface temperature of 70.1°C. However the infrared images revealed that the actual surface temperature of the DSP lies between 52.3°C and 54.3°C, indicated by Figure 54 and Figure 55. As such, the power dissipation of the DSP was changed to a lower value of 0.5 Watts. Figure 66 shows the thermal profile using this estimate.

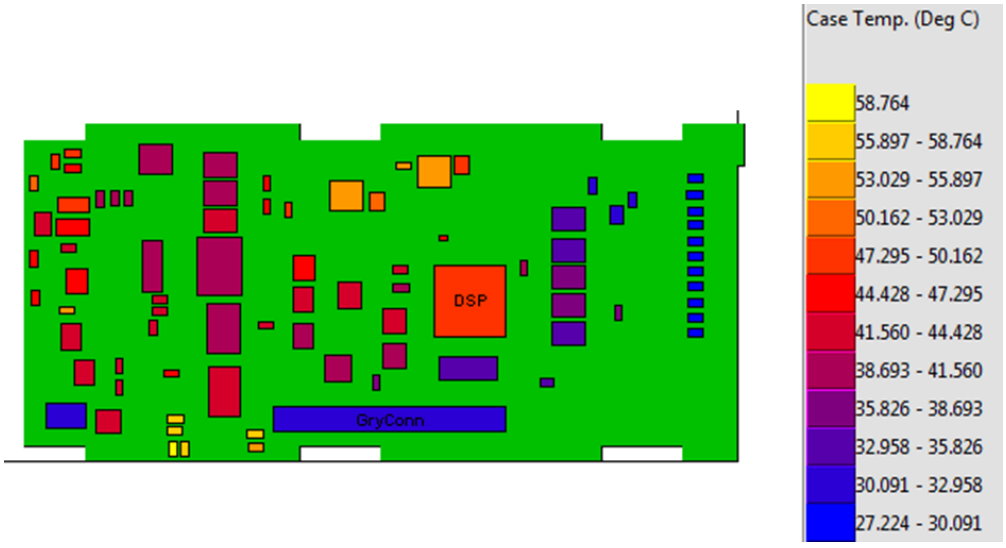

Figure 66 Thermal profile of control board, DSP = 0.5W

The adjusted power dissipation of the DSP reveals a surface temperature of 49.2°C, slightly under the acceptable surface temperature range. Therefore further iterations were conducted in order to fit the surface temperature in between the acceptable range. It was ultimately determined through this process that the DSP dissipates 0.62W of power. This produces a surface temperature of 53.1°C which falls in the middle of the acceptable temperature range.

This iteration process was conducted for each component on all three boards. However, one complication arose in that the power dissipation of one component affected the surface temperatures of nearby components. Therefore, on each of the three boards the power dissipation values of the largest and hottest components were determined first. Once this process was conducted for all components, a series of fine tune adjustments were made across all boards to ensure that each component fell into the range of acceptable values. This was a manual process that consumed much time. In order to simplify this process the acceptable temperature range was increased by 2°C. For example, if the IR images revealed that a small resistor had a temperature range between 39.2°C – 40.4°C, the acceptable temperature range produced by the thermal simulations was increased to 38.2°C – 41.4°C.

While this process only needed to be conducted once for the control board, due to the fact that the idle and full load conditions produced the same thermal profile, this same process was conducted for all components on the power and connector boards both at the idle and full load conditions. The final result of this process was a complete inventory of power

dissipation values for each component in the motor drive. The Appendix contains the thermal profiles generated using the natural convection conditions.

These values were discovered while the boards were under natural convection conditions operated outside the drive case. Using the same component power dissipation values and simply changing the thermal simulation parameters, the thermal profiles of the boards while operated inside the drive case could be simulated. The section *Thermal Simulations in CalcePWA* will discuss this in detail.

6.4 Discussion and Analysis

Infrared imaging provided a decent method to capture the thermal profile of the boards. The images show that the surface temperatures of each component can be easily identified. One major issue was determining the proper emissivity value of each component. As stated earlier in the report, boron nitride spray was used initially to unify all surface emissivity values. However the high conductivity of the spray created a heat-spreading effect making it virtually impossible to capture the thermal signature of each component. The final method consisted of measuring the surface temperatures of each component using two different emissivity values. This provided a temperature bracket through which the actual temperature was assumed to be contained within. While this approach served as a viable method for this application, this process would benefit from a more accurate emissivity determination method.

Furthermore, capturing the surface temperatures of the larger components on the power and connector boards was difficult because the geometries and sizes of the components varied. Many of the larger components prevented smaller components from being seen at the same angle. Therefore, the IR camera was constantly moved and arranged so that all components could be seen. Factors such as viewing angle and viewing distance may affect the accuracy of the IR images [43] therefore altering these to measure different components may have affected the accuracy of the measurements.

The control board was the simplest assembly to take infrared images of. All of the components were relatively the same height and existed on the same plane. Only micro-adjustments of the IR camera were made to capture all components on the board. Therefore, it was assumed that the surface temperatures extract from the IR images of the control board were most accurate compared to the other assemblies.

Due to the fact that the junction-to-case thermal resistance values were assumed to be constant throughout the control board assembly, the power dissipation values were most likely unrepresentative of real-world component applications. While the assumptions conducted in this application with regards to component thermal resistance are viable for a first-order simulation, truly determining component power dissipation would require an electrical schematic and simulation of the system.

According to the junction-to-case thermal resistance equation defined earlier in this chapter, the assumed θ_{jc} value was essentially arbitrary. The power dissipation values

inputted into the model during the iterative calibration process were selected as to align the surface temperatures from the IR images to the surface temperatures in the simulations. Regardless of the junction-to-case thermal resistance, the surface temperatures were still able to be aligned. For example, a component with assumed θ_{jc} of 10°C/W was discovered to require a power dissipation of 1 W to yield of a surface temperature of 50°C. According to the equation presented at the beginning of this chapter, the junction temperature of this component would be 60°C. However, if the assumed θ_{jc} was 15°C/W rather than 10°C/W, it would require 0.66W of power to align the junction and surface temperatures of the same component to 60°C and 50°C respectively. In conclusion, the surface temperatures of the components were able to align during the calibration process regardless of the thermal resistance used.

The one downside to this assumption is that power dissipation in the model was calibrated in order to match the model to the infrared images. Therefore the power dissipation value used for each component in the model may not be representative of the true power dissipation. While this does not pose a problem for this application, future iterations of this method may need accurate θ_{jc} values.

Chapter 7: Thermal Simulations in CalcePWA

Prior to performing reliability assessments in CalcePWA, thermal profiles of all boards simulating component temperatures inside the case needed to be developed. The previous two sections in this report described how component power dissipation values were derived from component surface temperatures measured with the IR camera. Once known, these power dissipation values were used in the CalcePWA thermal analysis tool to model component temperatures. From these thermal profiles, the PoF reliability assessment could be conducted.

7.1 Control Board

Although component power dissipation values on the control board do not change with load, the boundary conditions of the board do change while operated inside the case. The fan plays a major role in this observation as described in Table 11, Table 12 and Table 13. Therefore two thermal profiles were created of the control board, one capturing temperatures while the drive was idle and the other while the drive was operated at full load. Figure 67 displays the estimated thermal profile of the control board while idle inside the drive case. Using the same power dissipation values extracted, as described in the previous section of this report, parameters of the thermal simulation software were changed in order to capture conditions inside the case.

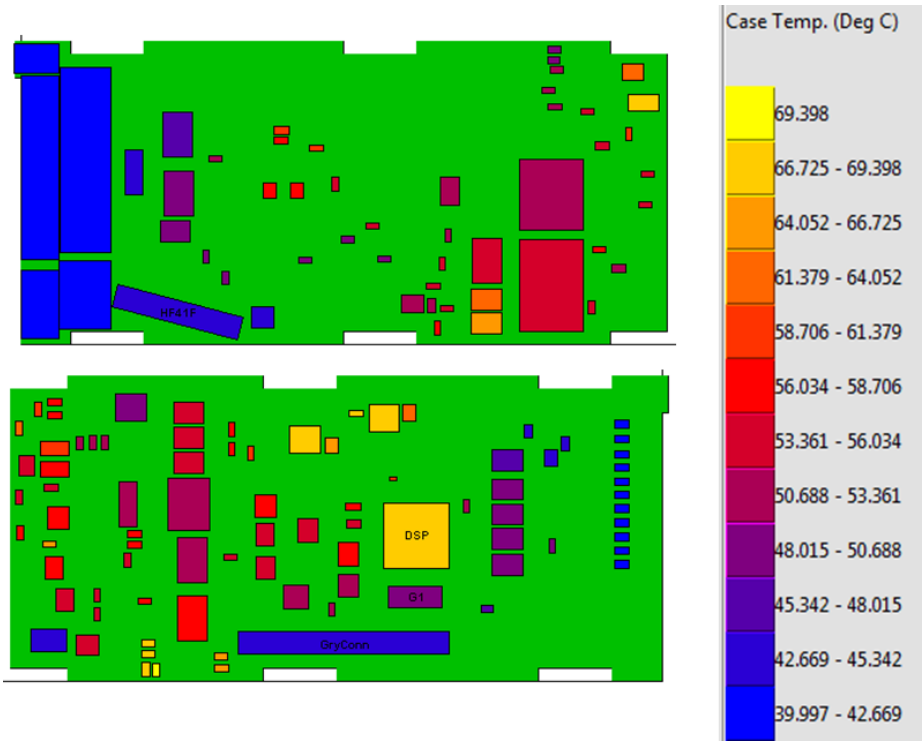

Figure 67 Thermal profile: control board, idle

Table 16 displays the simulation parameters used to generate the thermal profile in the CalcePWA simulation analysis tool.

Table 16 simulation parameters for thermal profile: control board, idle

Analysis Type	Conduction with Natural Convection
Max Iterations	1000
Ambient / Surrounding Temperature	39.9°C
Space Above Top Surface	10 mm
Space Below Bottom Surface	20 mm
Nodes in X-Direction	50
Nodes in Y-Direction	50

The surrounding temperature was measured using thermocouples as described in Table 11. The “Space Above Top Surface” was taken to be the space between the top surface of the control board and the motor drive case while the “Space Below Bottom Surface” was taken to be the space between the bottom surface of the control board and the connector

board. Figure 68 displays the estimated thermal profile of the control board inside the case while the drive is under full load.

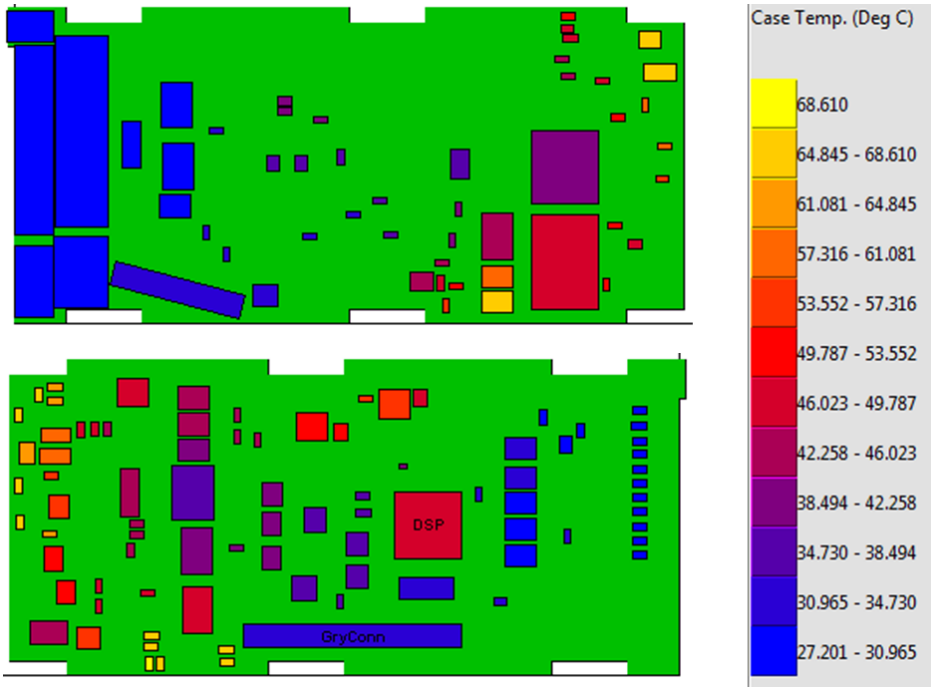

Figure 68 Thermal profile: control board, full-load

Table 17 displays the simulation parameters used to generate this thermal profile.

Table 17 simulation parameters for thermal profile: control board, full-load

Analysis Type	Flowover
Max Iterations	1000
Ambient / Surrounding Temperature	27.1°C
Flow rate	0.00228 kg/s
Space Above Top Surface	10 mm
Space Below Bottom Surface	20 mm
Nodes in X-Direction	50
Nodes in Y-Direction	50

As stated earlier in the report, the total fluid flow rate of the fan is 0.0114 kg/s. In order to distribute the fluid flow rate across all three boards in the simulation, a division of the flow rate was implemented according to Table 18. These values were estimated

according to the relative surface area of the boards along with their placement with respect to the fan location.

Table 18 Distribution of flow rate across boards

	Percentage	Fluid Flow Rate (kg/s)
Control board	20	0.00228
Power board	50	0.0057
Connector board	30	0.00342

7.2 Power Board

The same process used to generate the thermal profiles for the control board was used to generate the thermal profiles for the power board. Figure 69 shows the estimated thermal profile of the power board while the drive is idle and Table 19 displays the corresponding simulation parameters.

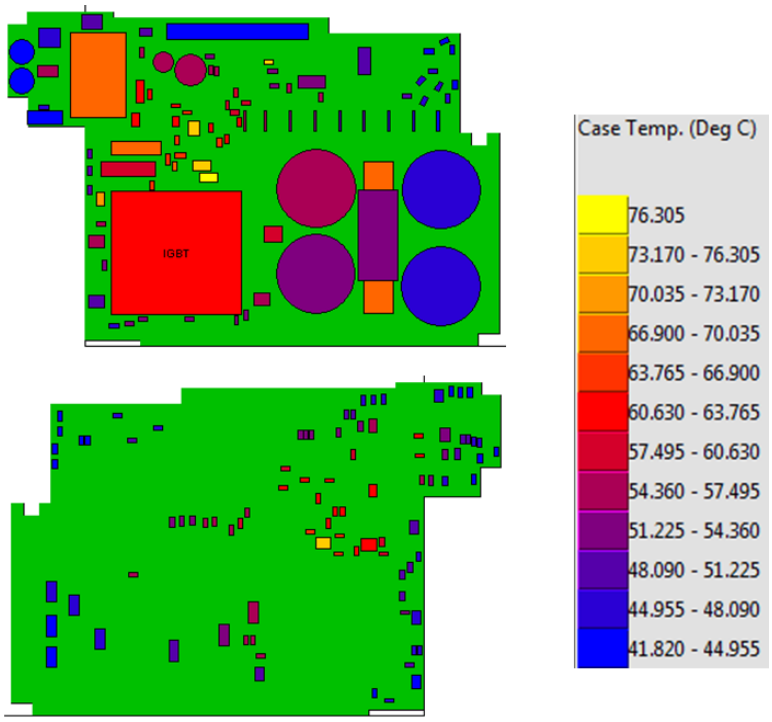

Figure 69 Thermal profile: power board, idle

Table 19 Simulation parameters for thermal profile: power board, idle

Analysis Type	Conduction with Natural Convection
Max Iterations	1000
Ambient / Surrounding Temperature	40.9°C
Space Above Top Surface	5 mm
Space Below Bottom Surface	50 mm
Nodes in X-Direction	50
Nodes in Y-Direction	50

As seen in the thermal profiles, the larger components remain relatively cool compared to some of the passive devices on the back side of the board. However, Figure 70 shows the estimated thermal profile of the power board while the drive is under full load which shows that a number of components are dissipating significantly more heat than the idle conditions. Table 20 displays the simulation parameters used for this profile.

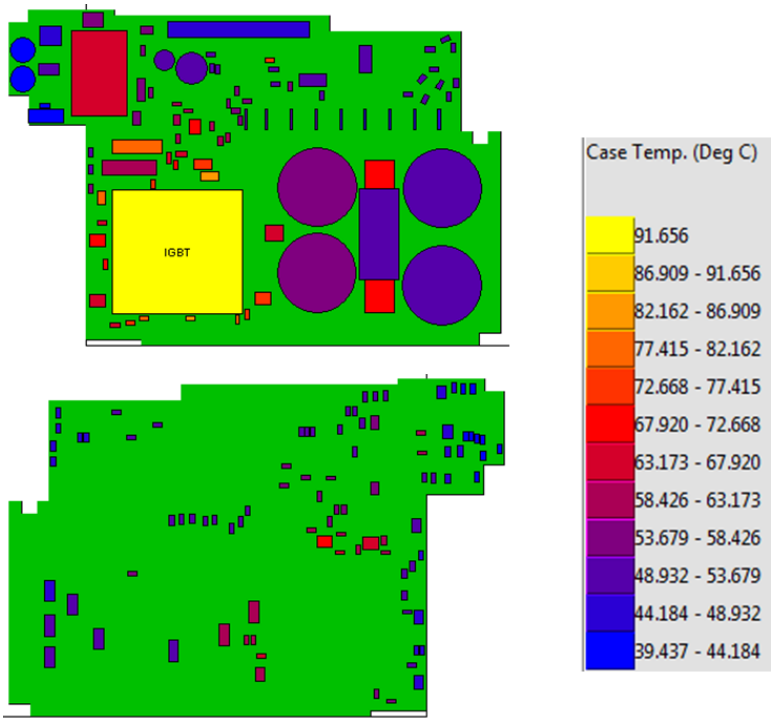

Figure 70 Thermal profile: power board, full-load

Table 20 Simulation parameters for thermal profile: power board, full-load

Analysis Type	Flowover
Max Iterations	1000
Ambient / Surrounding Temperature	29.0°C
Flow rate	0.0057 kg/s
Space Above Top Surface	50 mm
Space Below Bottom Surface	5 mm
Nodes in X-Direction	50
Nodes in Y-Direction	50

7.3 Connector Board

Figure 71 shows the estimated thermal profile for the connector board while the drive is idle and Table 21 displays the corresponding simulation parameters.

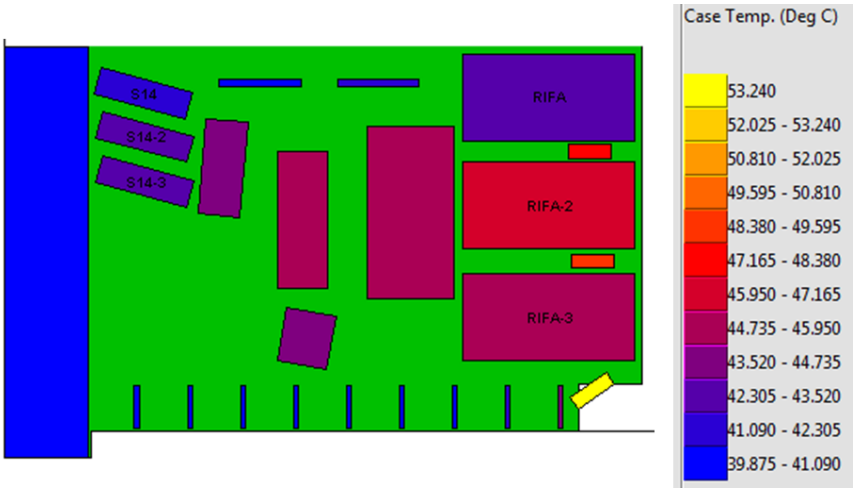

Figure 71 Thermal profile: connector board, idle

Table 21 Simulation parameters for thermal profile: connector board, idle

Analysis Type	Conduction with Natural Convection
Max Iterations	1000
Ambient / Surrounding Temperature	39.5°C
Space Above Top Surface	25 mm
Space Below Bottom Surface	10 mm
Nodes in X-Direction	50
Nodes in Y-Direction	50

Figure 72 shows the thermal profile of the connector board while the motor drive is under load and Table 22 displays the respective simulation parameters.

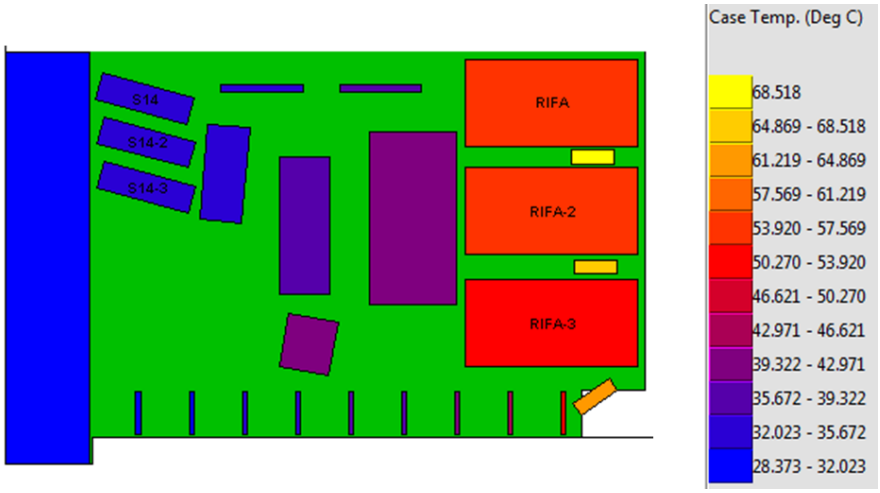

Figure 72 Thermal profile: connector board, full-load

Table 22 Simulation parameters for thermal profile: connector board, full-load

Analysis Type	Flowover
Max Iterations	1000
Ambient / Surrounding Temperature	27.0°C
Flow rate	0.00342 kg/s
Space Above Top Surface	25 mm
Space Below Bottom Surface	5 mm
Nodes in X-Direction	50
Nodes in Y-Direction	50

7.4 Discussion and Analysis of Thermal Simulations

The accuracy of the thermal simulations can be estimated based on the accuracy of the infrared images, the power dissipation extraction process and the simulation parameters. One major assumption that was implemented during this process was the distribution of the airflow across all boards. The power board is the largest assembly and is located directly in front of the fan. The connector board, although smaller than the control board, is located slightly outside the air flow path. The control board is located farthest away from the fan and has larger number components. The connector board blocks potential

airflow to the control board. While the air flow distribution was implemented based upon educated reasoning, the exact distribution would require FEM simulation to accurately determine.

Furthermore, thermal boundary measurements revealed that temperature gradients inside the drive existed, especially while the drive was idle. The CalcePWA simulation software only allows the user to define the boundary temperatures surrounding the board. With air temperature variations up to 16.7°C inside the drive, the simulation software does not have the ability to integrate this into the thermal profiles developed. While altering the thermal simulation software is outside the scope of this project, the thermal profiles developed may be more representative of real world systems if the software has the ability to take into account temperature gradients.

Chapter 8: CalcePWA Reliability Assessment

The reliability assessment software in CalcePWA consists of two primary applications, the Life Cycle Load Profile Manager (LCPM) and the PWA Failure Analysis tool. The LCPM allows the user to define the loads and stresses that the assembly will experience throughout the expected life cycle. Once defined, the Failure Analysis tool scans the assembly for applicable PoF-based failure mechanisms and then calculates estimated times-to-failure for each component. The results are presented in tabular format and contain both estimated times-to-failure and estimated number of cycles to failure based upon the loads defined in the LCPM.

To validate and calibrate the reliability assessment method described in this study, the CalcePWA failure analysis results were compared to accelerated tests of the motor drive. The load-generating test setup was used to perform power cycling of the drive based upon accelerated field conditions. Although there exists other forms of accelerated testing that are relevant to these assemblies, this section will describe the LCPM and the failure analysis results as they pertain to the power cycling tests conducted and the passive temperature cycling test.

While the primary focus of this study was on the control board, both the power board and connector board were analyzed using the CalcePWA reliability assessment as well. Due to the fact that these assemblies contain non-standard parts, only the standard parts (SMDs, PEMs, Connectors, etc.) were analyzed in this fashion.

8.1 Life Cycle Load Profile

The LCPM application allows users to define the stress profile through which the assembly will cyclically undergo during the life cycle. These stresses include thermal cycling, mechanical shock, mechanical cycling, harmonic vibration, random vibration and a temperature-humidity bias. Each of these can be induced as a single stress or can be coupled together.

The fundamental goal behind accelerated testing is to quickly gather information on the product performance and estimated life under normal use [46]. By increasing the magnitudes of the applied stresses or increasing the frequency through which they occur, the same mechanism that created failure in the field could be recreated under accelerated conditions in a shorter period of time. However, sound assumptions and a complete knowledge of all potential failure mechanisms are necessary due to the fact that the exaggerated testing conditions may also accelerate undesired mechanisms [47]. This would skew the results. For example, many failure mechanisms may be dormant under normal use but may become active under accelerated stress levels [48]. This would result in reliability data that would be unrepresentative of normal use conditions.

Power cycling the motor drive was one of the primary validation test performed. Therefore a load profile was created to be representative of this test and will depict only the stresses that occur during power cycling. The primary stress that occurs is thermomechanical in nature and is caused by the varying temperature levels experienced during the idle and full-load operating condition. The drive was cycled while stationary

on a platform, thus eliminating any random or cyclical vibration or shock. Furthermore, the test was conducted at room temperature (25°C) indoors therefore it was assumed that humidity will yield negligible effects on the motor drive. Temperature cycling was the only stress created in the LCPM.

The thermal boundary measurements revealed that it takes approximately 10 minutes for the temperature inside the drive to reach steady-state, either in the full-load or the idle operating condition. However, approximately 90 percent of this temperature was reached within the first three minutes. Therefore, the thermal cycling profile was defined according to Table 23.

Table 23 LCPM thermal cycling profile

Dwell Time at Max. Temp.	3 min.
Dwell Time at Min. Temp.	3 min.
Ramp Time to Max. Temp.	45 sec.
Ramp Time to Min. Temp.	45 sec.
Temperature Cycles Per Day	192

This profile was used for all three boards in the motor drive. For the control board, the idle condition thermal profile represented the maximum temperature of the thermal cycle while the minimum temperature of the thermal cycle was represented by the full-load condition. However, for the power and connector boards the maximum temperature of the thermal cycle was described by the full-load thermal profile. This was because the power board contains components that dissipate more heat at increased power levels. Likewise, the minimum temperature of the thermal cycle was depicted by the idle condition thermal profile.

While there are a variety of applications, the number of cycles the motor-drive will undergo during normal use was estimated to be less than 10 per day. For industrial purposes this number is most likely closer to three, however 10 cycles per day served as a conservative estimate. Therefore this power cycling test produces an acceleration factor of 19.2. In other words, failure from this accelerated test is estimated to occur 19.2 times faster than failure in the field. For example, if failure from this test occurs in one year, the product is estimated to last 19.2 years in the field. However, the caveat to this statement is that the failure mechanisms that cause failure in one year during the accelerated testing must be the same failure mechanisms that cause failure in 19.2 years in the field. While power cycling is one form of accelerated testing and can provide insight into the reliability of the system, a variety of other accelerated tests must be conducted in order to accurately assess system reliability.

8.2 Failure Analysis

Once the LCP was defined, the failure analysis software was ran and produced estimated times-to failure for each component based upon specific failure mechanisms. Although there are a total of 31 failure mechanisms the CalcePWA software is capable of screening for, only six of them were applicable for the components on these assemblies. The following are the failure mechanisms in which the CalcePWA software tested for:

- First Order Thermal Fatigue Model for Leadless Packages
- First Order Thermal Fatigue Model for Gullwing Packages
- First Order Interconnect Thermal Fatigue Model for Surface Mount Transistor Packages

- First Order Interconnect thermal Fatigue Model for C-Leaded Packages
- First Order Thermal Fatigue Model for Insertion Mount Axial Packages
- First Order Thermal Fatigue Model for Insertion Mount PGA Packages

Each of these failure mechanisms are modeled using a mathematical formula. As an example, the 1st order thermal fatigue model for leadless packages is shown the equation below,

$$N_f = \frac{1}{2}\left(\frac{\Delta\gamma}{2\epsilon_f}\right)^{\frac{1}{c}} \tag{6}$$

where N_f is the median cycles to failure, $\Delta\gamma$ is the solder cyclic shear strain range metric, $2\epsilon_f$ is the fatigue ductility coefficient, and c is the fatigue ductility exponent and is dependent on mean cyclic solder joint temperature, steady state operating temperature for the substrate and component, temperature during off half-cycle and half-cycle dwell tie at high temperature [49][50][51]. The key assumptions are as follows [51] and were taken as written from the documentation:

- *Maximum strain occurs at corner solder joint in component*
- *In-plane deformations cause the damage while out of plane warping is ignored*
- *Solder joint is modeled as a simple pillar of solder which undergoes uniform shear deformation.*
- *Complete stress relaxation occurs during the thermal cycle.*

This failure mechanism is one example of the six included in the failure analysis. While it is unnecessary to describe each failure mechanism in detail, more information regarding the 31 failure mechanisms can be found in the CalcePWA software documentation.

The simulated thermal stress induced from power cycling was applied to each of the three boards and mean times-to-failure were calculated for each component. The first five failures that are estimated to occur in the control board are shown in Table 24, with the location of each failed component shown in Figure 73.

Table 24 CalcePWA estimated failures: control board

Component	Estimated Cycles to Failure	Relevant Failure Mechanism
R80	4.6e4	First Order Thermal Fatigue Model for Leadless Packages
R81	5.0e4	
C113	2.9e5	
R220	3.1e5	
R222	3.6e5	

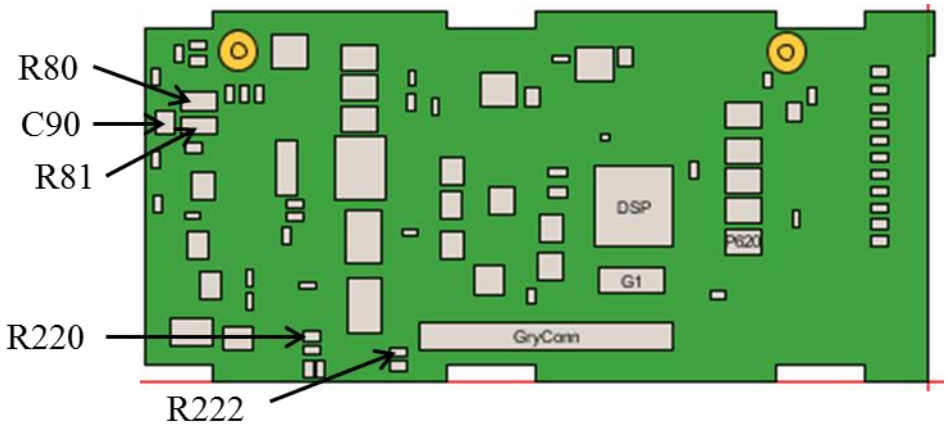

Figure 73 CalcePWA component locations: control board

On the control board, the first five components predicted to fail are located on the underside the assembly. This is the side facing the power board. Furthermore, it was predicted that the first components to fail are SMD resistors and capacitors. The first components estimated to fail on the power board were also SMD resistors and capacitors and fail due to the first order thermal fatigue model for leadless packages. Table 25 lists

the first five component failures on the power board while Figure 74 shows the locations of these failures.

Table 25 CalcePWA estimated failures: power board

Component	Estimated Cycles to Failure	Relevant Failure Mechanism
R100	3.8e4	First Order Thermal Fatigue Model for Leadless Packages
C150	6.3e4	
R200	6.4e4	
C151	1.1e5	
C152	1.2e5	

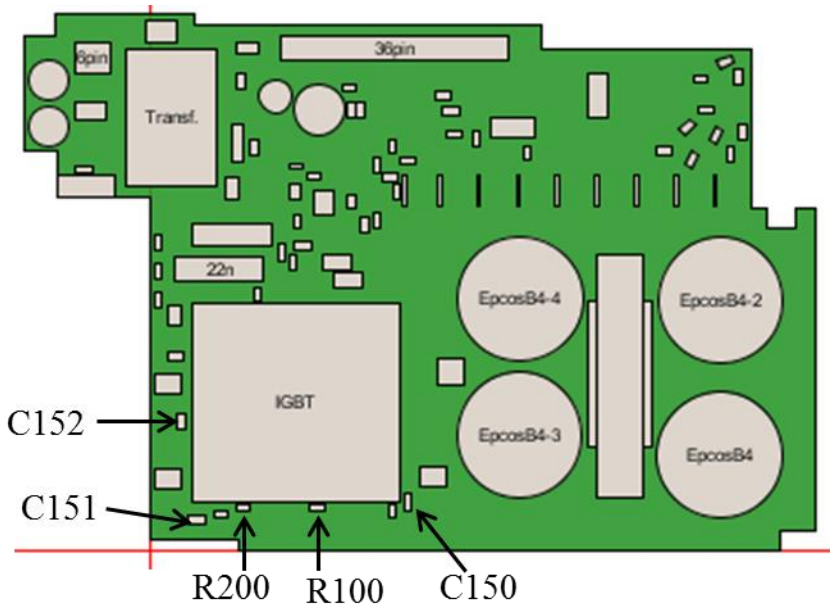

Figure 74 CalcePWA component locations: power board

The first components predicted to fail on the power board were all located on the same side of the board. They are also located within close proximity to the power switching module and are likely to undergo the largest thermomechanical stress which is driven by the heat dissipation from the power switching module. Infrared images also revealed that the power switching module was the major heat dissipating component.

The components on the connector board were also analyzed for estimated interconnect failure times. The CalcePWA failure analysis revealed that the first components to fail due to interconnect failures were the film capacitors. These components were estimated to fail after $2x10^{10}$ cycles, however they are more likely to fail due to mechanisms other than interconnect failure [52]. Through-holed interconnects are stronger than SMD interconnects. As such, these failures are of little concern to the system level reliability assessment.

8.3 Passive Temperature Cycling of the Control Board

While power cycling the motor drive provides a complete testing method for the motor drive system, an additional test can be performed which decouples the control board from the system and analyzes it as a separate entity. Passive temperature cycling consists of placing the assembly in an environmental test chamber and thermal cycling the board based upon a specified profile. The control board would not be operated under any power, therefore the only stress acting upon the assembly can be assumed to be thermomechanical in nature. This section only discusses the estimated reliability results based upon the CalcePWA failure analysis simulations. The profile through which the control board assembly will undergo is described in Table 26.

Table 26 Profile for passive temperature cycling of the control board

Dwell Time at 65°C	30 min.
Dwell Time at -20°C	20 min.
Ramp Time to Max. Temp	20 min.
Ramp Time to Min. Temp	20 min.
Total Cycle Time	90 min.

The same failure mechanisms described in the power cycling failure analysis were screened for in the temperature cycling failure analysis. Table 27 displays the first five components to fail along with the estimated mean cycles to failure. Figure 77 shows the locations of failed components

Table 27 Estimated times-to-failure for passive temperature cycling of the control board

Component	Estimated Cycles to Failure	Relevant Failure Mechanism
317M	1228	First Order Interconnect Thermal Fatigue Model for Surface Mount Transistor Package
R80	1354	First Order Thermal Fatigue Model for Leadless Packages
R81	1354	
C113	2516	
C90	6971	

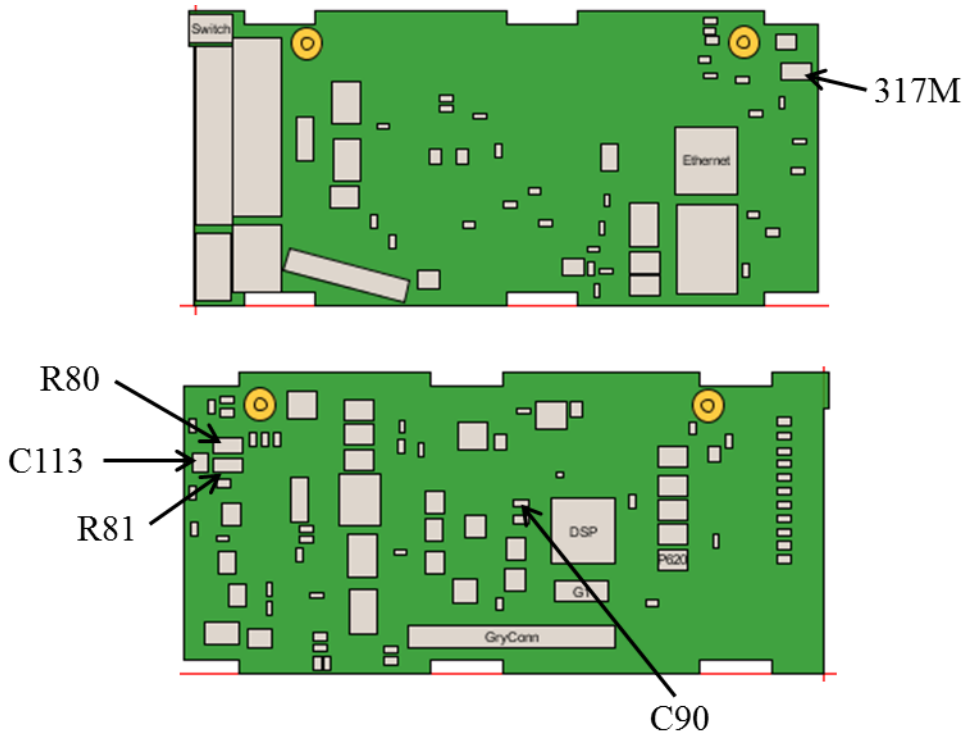

Figure 75 Locations of failures during passive temperature cycling

The 317M component is estimated to fail first. This component is a 500mA adjustable output, positive voltage regulator and was modeled as a small outline transistor in the CalcePWA model. The failure mechanism that computes the mean cycles to failure for this component is a function of the effective bond area of the foot, shown in Figure 76. As such, a smaller bond area of the foot yields lower reliability predictions.

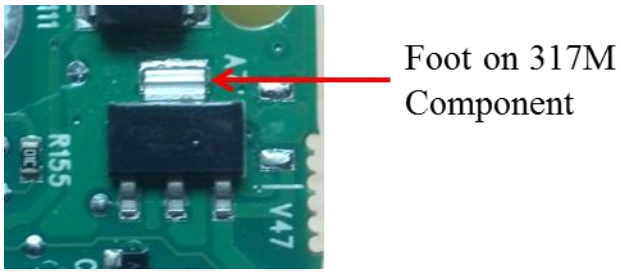

Figure 76 Component: 317M

The R80, R81 and C113 components were estimated to fail next. These failures falls in line with the failure analysis conducted from the power cycling simulations. The 317M components did not appear to pose any hazard during the power cycling reliability simulation due to the fact that the temperature change of this component was not sufficient enough to invoke failure.

8.4 Discussion and Analysis of CalcePWA Failure Assessment

On the control and power boards the first five components to fail during the power cycling simulations are surface mounted passive devices. The two resistors to fail first on the control board, R80 and R81, are larger in size than the rest. Therefore it can be hypothesized that SMD component size contributes to solder joint reliability. Furthermore, the first five components to fail on the power board all surround the power switching module. Therefore it can also be hypothesized that the temperature changes that result from power cycling contributes to interconnect reliability.

While validation measures are necessary to determine the accuracy of the simulations, enough information was revealed to begin reliability enhancement methods. For example, underfill is shown to enhance the reliability of solder bumped flip chips through mitigating thermomechanical stresses induced from CTE mismatch [53]. The underfill material reduces the amount of strain in the solder joint by distributing the stress throughout the solder bump-underfill formation. This same mechanism can be applied to the problem areas identified from the reliability analysis. Epoxy can be applied over the solder joints decreasing the amount of stress induced within the joint during temperature cycling. This same principle has already been applied to the Ethernet and six-pin connector on the control board, shown in Figure 77.

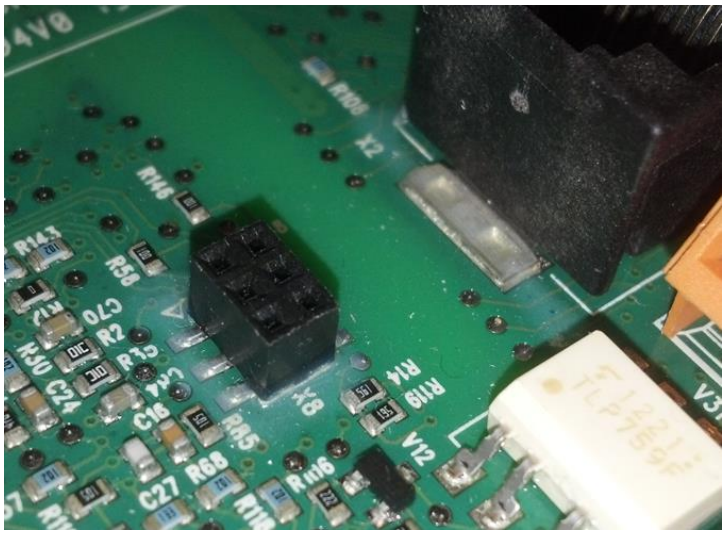

Figure 77 Epoxy Enveloping Interconnect Joints

Both power cycling and passive temperature cycling reveal problem areas of the control circuitry in which this reliability enhancement method can be applied prior to simulation validation results.

Chapter 9: Power Cycling Accelerating Test

The load-generating test setup was used to power cycle the motor drive according to the method described in the *CalcePWA Reliability Assessment* section of this report. To re-emphasize, the motor drive will be held idle for three minutes and will be operated at full-load for three minutes. The ramp up and ramp down times will take approximately 45 seconds. This cycle will be repeated 192 times per day.

9.1 Sequence Programming Tool

The motor-drive comes equipped with a Sequence Programming Tool (SPT) that allows the user to program a set profile through which the drive should operate under. This tool is built into the DriveWindow Light software package and allows the user to operate the drive through a USB cable connected to a computer. The SPT provides the user the

ability to define up to eight different operating states of the motor. The parameters that define each state include run, stop and direction commands, acceleration and deceleration ramp times, state duration, source for the drive reference value, signal source for triggering to the next state and signal source for triggering the shift to any state. Each state can also send output signals to external devices. Figure 78 shows a visual representation of the SPT and the varying states.

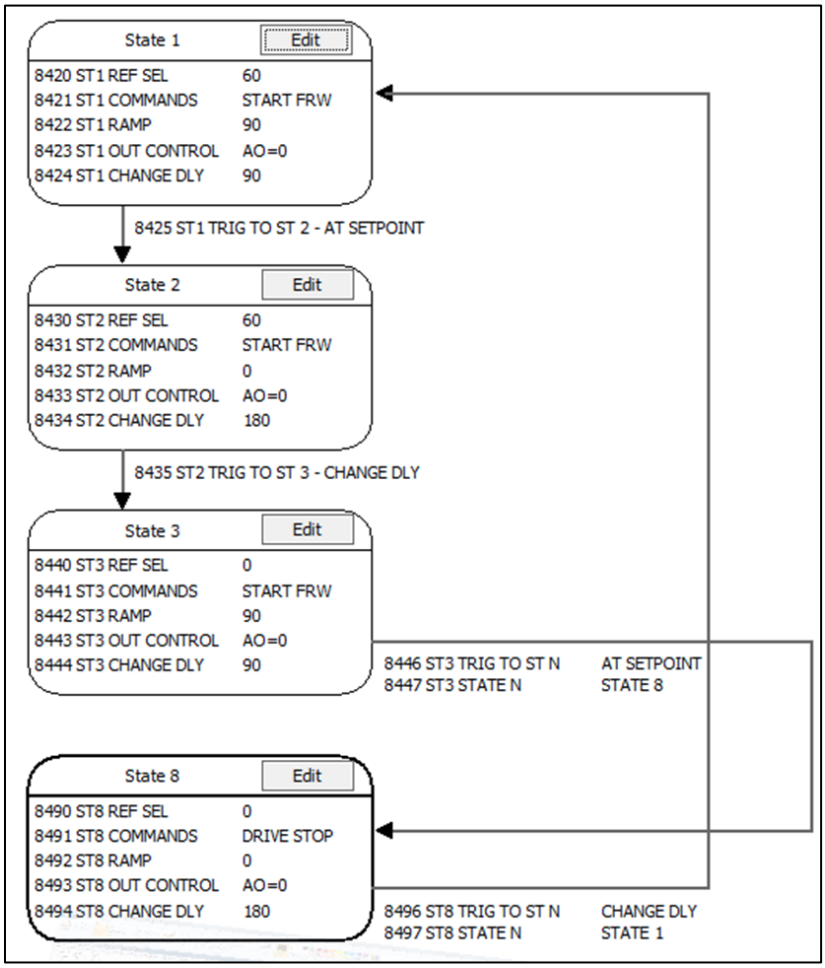

Figure 78 Visual representation of SPT

State 1 represents the ramp up state in which the drive accelerates from idle (0 Hz) to the full-load condition which occurs at 30 Hz. The system is in this state for approximately 45 seconds. State 2 represents the three minute hold while the drive is operating at full-

load. State 3 represents the ramp down state in which the drive decelerates from full-load to idle. Like State 1, the system is in State 3 for approximately 45 seconds. Finally, State 8 represents the hold at idle which last for 3 minutes. States 4-7 are omitted because the SPT is designed so that States 8 occurs as the last state in the cycle.

The two triggers that signal a state change are a timer and a feedback signal containing the speed of the motor. State 1 transitions into State 2 once the system reaches 30 Hz. Once in State 2, a timer begins and signals the transition into State 3 once three minutes are reached. State 8 is reached once the feedback signal from State 3 signifies a system speed of 0 Hz. A timer begins and when three minutes are up the system is reset back to State 1. Furthermore, after each cycle a counter is updated to keep track of how many cycles have past.

9.2 Monitoring the System

The DriveWindow Light software and the SPT allow the user to visually monitor up to four parameters during motor drive operation. While there are numerous parameters that can be monitored, the four chosen to be monitored were the control board temperature (measured by a thermistor on the board), the output current to the motor, the frequency of the motor and a cycle counter. Data points were taken every two seconds for the duration of testing and were stored in files containing up to a million data points. However, due to the nature of the testing environment which required occasional stopping of the test, multiple files were used with each representing a series of continuous cycles. The power

cycling test was interrupted a handful of times and was stopped during weekends for safety concerns. Each time the test was stopped, a new monitoring file was created.

9.3 Running the Power Cycling Test

Once the SPT was programmed, the power cycling began. It was discovered through initial testing of the magnetic break than an analog signal between 1.35 – 1.50 V generated enough torque on the motor to create the full-load operating condition of the drive. Throughout testing, the magnetic break continuously applied a torque. While the motor was idle, the magnetic break produced a static torque on the motor. In order to overcome this torque, the amount of current sent to the motor spiked significantly during the acceleration phase of each cycle. While this current spike was significant, it only lasted for a brief moment and leveled out to the full load condition (3.7A) once the motor reached 30 Hz. Figure 79 displays an example of the visual monitoring conducted during the test wherein the current spikes (green line) up to 8.7A can be seen. While this image displays an example of the data gathered during testing, the complete data sets will be included in the Appendix of this report. This test is ongoing and will run past the timeframe of this project.

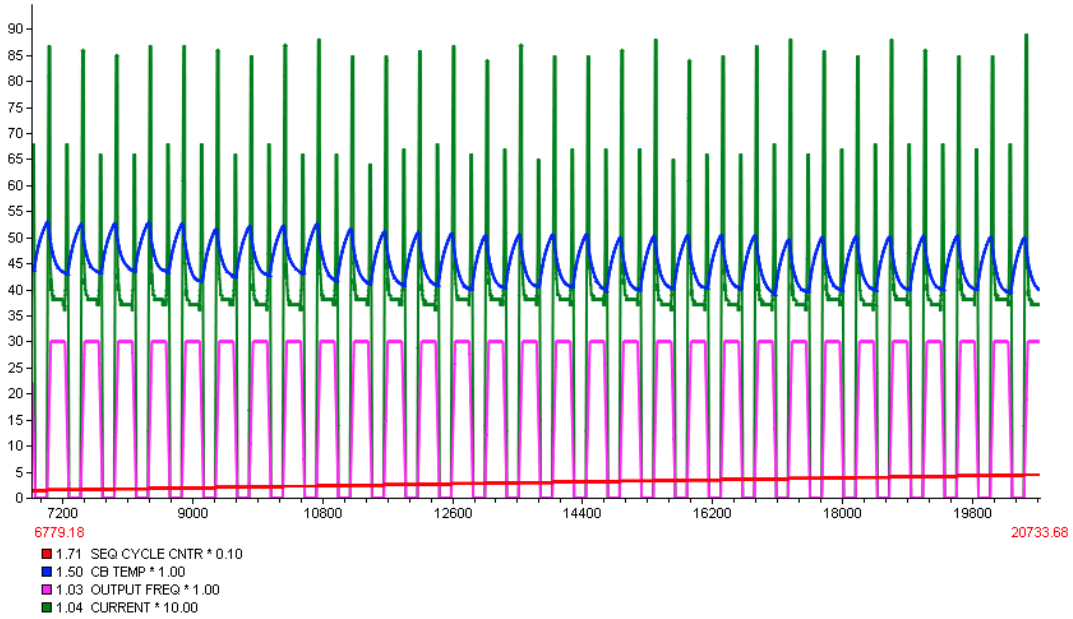

Figure 79 Example of monitored data from power cycling test

9.4 Discussion and Analysis of Power Cycling Test

The CalcePWA failure analysis indicated that interconnect failures are not likely to occur until 37,000 cycles. This results in approximately six months of continuous testing. Literature review indicated that the power switching module and electrolytic capacitors will most likely fail prior to interconnect failure.

As of Novemeber 18, 2013 the test has surpassed 10,000 cycles without any failure. The data collected up to this point, upon initial investigation, does not indicate the presence of degradation or failure. The data plots collected so far will not be included in this report (primarily because they do not indicate any significant findings), but can be attained through contacting the author of this report.

One method to obtain reliability results in significantly less testing time could be through the use of prognostic measurements. Mechanical and electrical parameters could be

monitored for degradation at both the component and system level. Rather than power cycling the system to failure, certain parameters of susceptible components, such as the R80 and R81 resistors, could be monitored. The power cycling failure analysis predictions could then be calibrated against the prognostic measurements. The *Future Work* section of this report describes this concept further.

Chapter 11: Summary and Concluding Remarks

The methodology used in this assessment allows for a complex assembly to be simplified and modelled in order to conduct a first order reliability survey of critical interconnects in normal operating and harsh environmental conditions. The primary advantage CalcePWA has over more complex FEM software programs is the speed in which the software performs the analysis. Once the model has been completed (including calibrated power dissipation values) the software takes less than a minute to perform the reliability assessment of all interconnects. While other software programs may allow for more detailed component models, the time to perform the same analysis would be significantly longer.

While constructing the CalcePWA model it was discovered that the component datasheets often times contained maximum power dissipation values. However after

performing the infrared thermography of the assemblies, it became apparent that similar components did not exhibit the same power dissipation. For example the control board contained three MOSFETS, two of which appeared relatively hot according to the IR images; yet the third MOSFET appeared inactive and dissipated significantly less heat. Therefore it can be concluded that calibration efforts, either through component temperature measurements or electrical analysis of the circuits, must be conducted to determine component power dissipation.

Furthermore, the load generating test setup can be used in future studies at CALCE involving electromechanical drive systems and is compatible for systems up to twice as powerful as the motor drive in this study. The DriveWindow Light software provides a means for controlling the cycle profile of the drive, therefore benchmarking and accelerated testing that can take place as various power levels.

Numerous thermocouple measurements of points surrounding the boards were taken at various loading conditions and revealed that the highest temperatures within the drive were reached while the drive was idle. The power switching module dissipates more power as the load increases, however the fan does not run while the drive is idle. While idle, a natural convection environment is produced inside the casing wherein each component on the control board reaches maximum temperatures. These findings indicate the importance of a reliable fan. This study assumed that the fan was fully operational and exhibited an airflow matching the manufacturer specifications; however the

reliability results would change significantly if the fan catastrophically failed or if the airflow was inhibited.

In order to capture component surface temperatures using the IR camera, the emissivity of each component was calibrated to that of black electrical tape. While the emissivity of each component ranged between 0.8 and 0.9, future iterations of this project could involve more precise emissivity measurement approaches. This would eliminate the temperature bracket which is assumed to contain the real surface temperature. The IR images were processed such that the amount of power each component dissipated was extracted. This was conducted using an iterative method using the CalcePWA thermal simulation tool.

Thermal and reliability simulations were conducted using the CalcePWA thermal and failure analysis programs. Two simulations were conducted, one simulating the three assemblies during accelerated power cycling and the other simulating the control board during passive temperature cycling. The thermal simulations used the power dissipation values and the thermocouple measurements to develop thermal profiles of all three boards while the drive was operating at both the idle and full-load conditions. These thermal profiles were used in the power cycling failure analysis. They represented the high and low temperature points through which the boards would cycle between.

After conducting the power cycling reliability simulation, it was discovered that the larger surface mounted passive devices on the control board would fail first. On the power board, the smaller surface mounted passive devices surrounding the power

switching module were estimated to fail first. This is likely due to the large temperature ranges through which each of these components would experience during continuous power cycling. The passive temperature cycling failure analysis of the control board indicated that a small outline transistor package was estimated to fail first. The other components estimated to fail early were the same components estimated to fail early during the power cycling failure analysis simulation. While validation methods are necessary to prove this methodology and the reliability results, it was hypothesized that the application of epoxy surrounding the solder joints would enhance reliability.

In order to validate the power cycling reliability simulation, accelerated power cycling was conducted of the motor drive. Although the testing time for the power cycling test is estimated to take approximately eight months, a number of operational parameters are being monitored in hopes of detecting degradation prior to failure. This may also serve as the basis for prognostic measurement techniques in future iterations of this method.

11.1 Future Work

This subsection describes tasks that may be implemented in future iterations of this assessment method. These were developed based upon obstacles and challenges discovered while developing this method and through retrospective analysis. While some of these projects are feasible and applicable immediately, many of them may take significant effort and refinement in order to apply them to power electronic system reliability assessment methods.

11.1.1 Passive Temperature Cycling of the Control board

The power cycling accelerated test will take approximately eight months of continuous testing to validate the failure analysis reliability simulations. While this test takes into account every component and assembly within the motor drive, passive cycling will provide a direct focus on the control board. A reliability simulation has already been conducted as described in the *CalcePWA Reliability Assessment* section. As such, this test will serve as a validation for the reliability assessment already conducted. This test will also eliminate the need to replace the power switching module, electrolytic capacitors and other components that may prematurely fail during the power cycling test.

11.1.2 Prognostic Monitoring

The power cycling reliability results indicate that a total testing time of approximately eight months will be required to induce interconnect failure on the control circuitry. The implementation of prognostic monitoring on the control board will indicate component or interconnect degradation well before failure occurs. This would shorten the accelerating testing times and would allow predictions to be made regarding the remaining useful life of the component or system.

11.1.3 Accurately Determine Component Emissivity

The infrared thermography process consisted of taking temperature measurements of the components assuming an emissivity of 0.8 and 0.9. This produced a range of acceptable surface temperatures that would be captured by the thermal simulations. The accuracy of the infrared measurement techniques could be improved if an exact emissivity was

known for each component, rather than a bracket. While a number of techniques have been employed to accurately determine surface emissivity [54] this has been a widespread issue with IR thermography.

Technologies do exist that provide a means for accurate emissivity measurements. For example, the Pyrometer Instrument Company manufactures a line of infrared cameras that measure surface temperature and emissivity at the same time [55]. This mitigates the emissivity and temperatures variations that may result from distance, viewing angle, wavelength of IR beam and thickness of conformal coating over the components. While these instruments may be costly, future iterations of this project would benefit greatly from more accurate emissivity measurements.

11.1.4 Update CalcePWA to Include Previously Customized Components

For the scope of this project, the CalcePWA software worked very well due to the fact that the control board primarily contained standard components. However, the power board and connector board contained components such as electrolytic and film capacitors, inductors, relays, power switching modules and metal oxide varistors which required the customization of generic blocks in the software to meet component dimensions, materials and other parameters. Although these customized components exhibited accurate interconnect properties, CalcePWA software updates to include these types of components would significantly enhance the program and assembly development time.

11.2 Academic Contributions

This work added a number of contributions to the field of power electronics which are described as follows:

- The model developed in CalcePWA served as an example to show that a complex assembly containing over a hundred components could be simplified for the purpose of performing a first-order interconnect reliability assessment. The results of this simulation indicated components most susceptible to interconnect failure during normal operating conditions and in harsh environments.
- Each component in the CalcePWA model required a power dissipation value, yet this value was unknown and could not be found in component datasheets. This study applied a method in which the power dissipation values used in the CalcePWA model were calibrated so that the surface temperatures produced from the thermal simulations matched the surface temperature captured through infrared thermography.
- In order to validate the models and overall methodology, an accelerated testing plan was developed to accelerate normal operating conditions through power cycling and harsh environmental conditions through passive temperature cycling.
- One major contribution to CALCE is the construction of the load generating test setup. This apparatus can be applied in applications involving drives and motors up to 5 kW (6.7 HP).

Appendix

CalcePWA Component Parameters

Table 28 Appendix: control board component parameters, 1 of 2

Identifier	Package Type	Lead Type	Lead Material	Pkg. Material	Location	Apprx. Weight (g)	Length (mm)	Width (mm)	Thickness (mm)	Pitch (mm)	#I/O	Interconnect Format
TLP759F	DIP8	GW	Copper	Epoxy Bisphenol	T/B	0.54	9.66	6.4	3.65	2.54	8	Dual Inline
LM293	SOIC8	GW	Copper	Epoxy Bisphenol	T/B	0.075	4.9	3.9	1.58	1.27	8	Dual Inline
LVC08A	TSSOP14	GW	Alloy42	Epoxy Bisphenol	T	0.054	5	4.4	1	0.65	14	Dual Inline
P781F	DIP4	GW	Copper	Epoxy Bisphenol	T/B	0.25	4.6	6.5	3.5	2.54	4	Dual Inline
317M	SOT223	GW	Copper	Epoxy Bisphenol	T	0.125	3.55	6.66	1.6	2.3	4	SOT-223
HF41F	Box. Relay	TH	Copper	PEI	T	5.4	28	5	15	4.41	5	Single Inline
DSP TMS	LQFP	GW	Copper	Epoxy Bisphenol	B	0.66	14	14	1.4	0.4	128	Quad
HCNR	DIP8	GW	Copper	Epoxy Bisphenol	B	0.96	11.15	9	4	2.54	8	Dual Inline
HCF4051	SOIC16	GW	Copper	Epoxy Bisphenol	B	0.144	9.9	3.9	1.55	1.27	16	Dual Inline
224PJUV	TSSOP14	GW	Alloy42	Epoxy Bisphenol	B	0.054	5	4.4	1	0.65	14	Dual Inline
431A1	SOIC8	GW	Copper	Epoxy Bisphenol	B	0.075	4.9	3.9	1.58	1.27	8	Dual Inline
MB3221I	TSSOP16	GW	Alloy42	Epoxy Bisphenol	B	0.055	5	4.4	1	0.65	16	Dual Inline
FR9014	TO-252 DPAK	GW	Copper	Epoxy Bisphenol	B	0.3	6.55	6	2.29	4.75	3	TO-252
17-33G	TO-252 DPAK	GW	Copper	Epoxy Bisphenol	B	0.3	6.55	6	2.29	4.75	3	TO-252
117AJG	TO-252 DPAK	GW	Copper	Epoxy Bisphenol	B	0.3	6.55	6	2.29	4.75	3	TO-252
MV324I	TSSOP14	GW	Alloy42	Epoxy Bisphenol	B	0.054	5	4.4	1	0.65	14	Dual Inline
L293	TSSOP14	GW	Alloy42	Epoxy Bisphenol	B	0.054	5	4.4	1	0.65	14	Dual Inline
ATMEL1113	EIAJ SOIC8	GW	Copper	Epoxy Bisphenol	B	0.134	5.24	5.29	1.8	1.27	8	Dual Inline
LV4066	TSSOP14	GW	Alloy42	Epoxy Bisphenol	B	0.054	5	4.4	1	0.65	14	Dual Inline
LVC125A	TSSOP14	GW	Alloy42	Epoxy Bisphenol	B	0.054	5	4.4	1	0.65	14	Dual Inline
P620	DIP4	GW	Copper	Epoxy Bisphenol	B	0.26	4.58	6.5	3.65	2.54	4	Dual Inline
SOT23	SOT23	GW	Alloy42	Epoxy Bisphenol	T/B	0.008	2.9	1.3	0.9	1.91	3	SOT23
GlassBody	SMD diode	GW	Tungsten	Soda lime Glass	T/B	0.031	1.58	2.65	1.5	3.6	2	Dual Inline
G1	Crystal	GW	Alloy42	Quartz	B	0.403	4.7	11.4	4	11.4	2	Dual Inline
S512	Varistor	GW	Copper	Epoxy Bisphenol	T	0.105	3.6	4.4	2	5	2	Dual Inline
SMDRes	SMDRes	leadless	leadless	Alumina 85%	T/B	0.017	3	1.6	0.5	x	2	SMD
R80	SMDRes	leadless	leadless	Alumina 85%	B	0.0681	3.15	6.2	0.5	x	2	SMD
R206	SMDRes	leadless	leadless	Alumina 85%	B	0.0045	0.8	1.6	0.5	x	2	SMD
C113	SMDcap	leadless	leadless	BaTiO2	B	0.10235	3.22	4.4	1.2	x	2	SMD
lbcap	SMDcap	leadless	leadless	BaTiO2	T	0.022	1.65	3	0.75	x	2	SMD
dbcap	SMDcap	leadless	leadless	BaTiO2	B	0.03	1.65	3	1	x	2	SMD
c6	SMDcap	leadless	leadless	BaTiO2	B	0.036	1.6	3	1.25	x	2	SMD
c88	SMDcap	leadless	leadless	BaTiO2	B	0.0246	1.6	3	0.85	x	2	SMD
c90	SMDcap	leadless	leadless	BaTiO2	B	0.036	1.6	3.2	1.08	x	2	SMD
LED	LED	clead	Alloy42	Epoxy Bisphenol	T	0.0206	2.8	3.5	1.75	3	2	Dual Inline
c131	cap	clead	Alloy42	Tantanum	B	0.08	3.5	2.8	1.9	1.8	2	Dual Inline
C335	cap	GW	Alloy42	Tantanum	T	0.011	1.75	3.15	1.62	2.75	2	Dual Inline
BlkConn	lg blk conn	TH	Copper	Ultem30	B	0.398	7.6	4.95	7	2.65	6	Dual Inline
6conn	sm blk conn	GW	Copper	Ultem30	T	0.164	6	3.93	4.6	2.1	6	Dual Inline
Connector1	connector	TH	Copper	Ultem30	T	15.816	40	11	19	5	8	Single Inline
Connector2	connector	TH	Copper	Ultem30	T	9.089	39.9	8.2	10	5	8	Single Inline
Connector3	connector	TH	Copper	Ultem30	T	3.393	14.95	8.05	10.15	5	3	Single Inline
Connector4	connector	TH	Copper	Ultem30	T	5.913	14.95	11.1	19.1	5	3	Single Inline
Connector5	orange conn.	TH	Copper	Ultem30	T	9.146	20	13.85	15.4	5	4	Single Inline
10 pin	connector	GW	Copper	Copper	T	1.376	9.9	3.75	23.4	1.6	10	Dual inline
Switch	Switch	TH	Copper	Ultem30	T	0.559	6.4	9.8	5.9	2.5	4	Dual Inline
Ethernet	ethernet	TH	Copper	LCP	T	3.08	15.4	14	12.6	1.5	9	SOT

Table 29 Appendix: control board component parameters, 2 of 2

Identifier	IO Span X (mm)	IO Span Y (mm)	Standoff Height (mm)	Solder Height (mm)	Solder Bond Area (mm^2)	Position of Paddle (mm)	Length of Paddle (mm)	Width of Paddle (mm)	Max Rated Temperature C
TLP759F	7.88	11.06	0.5	0.1	0.6	1.725	3.220	3.2	125
LM293	3.7	5.6	0.1	0.1	0.3	0.69	1.633	1.95	150
LVC08A	4.2	6.25	0.1	0.1	0.205	0.4	1.667	2.2	150
P781F	2.85	11	0.1	0.1	0.65	1.65	1.533	3.25	125
317M	4.75	6	0.1	0.1	0.375	x	x	x	125
HF41F	25.5	0	0.5	1	3	x	x	x	85
DSP TMS	12.4	12.4	0.1	0.1	0.108	0.6	4.667	7	150
HCNR	7.8	11.9	0.75	0.1	0.5	1.9	3.717	4.5	125
HCF4051	9.1	6.9	0.1	0.1	0.2	0.675	3.300	1.95	150
224PJUV	4.1	6	0.1	0.1	0.205	0.4	1.667	2.2	150
431A1	4	5.6	0.1	0.1	0.3	0.69	1.633	1.95	150
MB3221I	4.56	6	0.1	0.1	0.15	0.4	1.667	2.2	150
FR9014	4.75	9	0.1	0.1	0.6	x	x	x	150
17-33G	4.75	9	0.1	0.1	0.6	x	x	x	125
117AJG	4.75	9	0.1	0.1	0.6	x	x	x	125
MV324I	4	6	0.1	0.1	0.205	0.4	1.667	2.2	150
L293	4	6	0.1	0.1	0.205	0.4	1.667	2.2	150
ATMEL1113	3.9	7.7	0.1	0.1	0.225	0.8	1.747	2.645	125
LV4066	4	6	0.1	0.1	0.205	0.4	1.667	2.2	150
LVC125A	4	6	0.1	0.1	0.205	0.4	1.667	2.2	125
P620	2.85	11	0.4	0.1	0.4	1.725	1.527	3.25	100
SOT23	2.1	2	0.1	0.1	0.1125	0.35	0.967	0.65	150
GlassBody	0	3.6	0.1	0.1	0.64	x	x	x	175
G1	0	11.4	0.1	0.1	0.56	x	x	x	85
S512	0	5	0.1	0.1	0.22	0.9	1.200	2.2	125
SMDRes	x	x	0.1	0.1	0.8	x	x	x	125
R80	x	x	0.1	0.1	1.6	x	x	x	125
R206	x	x	0.1	0.1	0.24	x	x	x	125
C113	x	x	0.1	0.1	1.6	x	x	x	125
lbcap	x	x	0.1	0.1	0.825	x	x	x	125
dbcap	x	x	0.1	0.1	0.35	x	x	x	125
c6	x	x	0.1	0.1	0.8	x	x	x	125
c88	x	x	0.1	0.1	0.8	x	x	x	125
c90	x	x	0.1	0.1	0.33	x	x	x	125
LED	x	x	0.1	0.1	1.1	x	x	x	85
c131	x	x	0.1	0.1	1.6125	x	x	x	125
C335	0	2.75	0.1	0.1	0.225	x	x	x	125
BlkConn	5.3	2.6	0.1	0.1	3	x	x	x	105
6conn	4.2	5.15	0.1	0.1	0.8	x	x	x	105
Connector1	35	0	0.1	1	3	x	x	x	105
Connector2	35	0	0.1	1	3	x	x	x	105
Connector3	10	0	0.1	1	3	x	x	x	105
Connector4	10	0	0.1	1	3	x	x	x	105
Connector5	15	0	0.1	1	3	x	x	x	105
10 pin	8.4	6.4	0.1	0.1	0.825	x	x	x	150
Switch	2.5	7.3	0.1	1	3	x	x	x	105
Ethernet	9	16.44	0.1	0.1	1.44	x	x	x	85

Table 30 Appendix: power board component parameters, 1 of 3

Identifier	Package Type	Lead Type	Lead Material	Pkg. Material	Location	Apprx. Weight (g)	Length (mm)	Width (mm)	Thickness (mm)
nichicon680	snap cap	TH	Copper	Aluminum	T	0.208	8.15	8.15	12
nichicon220	snap cap	TH	Copper	Aluminum	T	0.266	8.15	8.15	15.3
KY100	snap cap	TH	Copper	Aluminum	T	0.164	6.4	6.4	12
KY1000	snap cap	TH	Copper	Aluminum	T	0.339	10.1	10.1	15.75
Epcos	snap cap	TH	Copper	Aluminum	T	27.78	25.1	25.1	50
1825ADJ	SOT223-5	GW	Copper	Epoxy Bisphenol	T	0.125	6.5	3.5	1.6
P781F	DIP4	GW	Copper	Epoxy Bisphenol	T/B	0.25	4.6	6.5	3.5
A921	SOT23-5	GW	Alloy42	Epoxy Bisphenol	T	0.012	2.9	1.55	1.1
SOT23	SOT23	GW	Alloy42	Epoxy Bisphenol	T/B	0.008	2.9	1.3	0.9
74LV4066	SOIC14	GW	Copper	Epoxy Bisphenol	T	0.129	8.65	3.9	1.4
LM239DG	SOIC14	GW	Copper	Epoxy Bisphenol	T	0.129	8.65	3.9	1.4
Transf.	Transf.	TH	Copper	Iron	T	73.85	27.25	18	25.4
RX27	WireRes	TH	Copper	Alumina 85%	T	17.08	9.4	48.5	9.4
RTD14012	box relay	TH	Copper	Iron	T	14	29	12.7	15.7
A400	SOIC8	GW	Copper	Epoxy Bisphenol	B	0.075	4.9	3.9	1.58
22n	box cap	TH	Copper	Aluminum	T	1.5	17.55	4.7	9.6
15nk	box cap	TH	Copper	Aluminum	T	0.2	7.2	2.5	6.5
K3747	TO-3PML	TH	Copper	Epoxy Bisphenol	T	5.05	16	4.35	22
BYG	SMD	GW	Alloy42	Epoxy Bisphenol	B	0.026	2.6	4.1	2.05
V844	SMD	GW	Alloy42	Epoxy Bisphenol	B	0.041	3.5	4.4	2.2
V150	SMD	GW	Alloy42	Epoxy Bisphenol	B	0.032	2.8	4.3	2.2
V802	SMD	GW	Alloy42	Epoxy Bisphenol	B	0.028	2.6	4.5	2
V850	SMD	GW	Alloy42	Epoxy Bisphenol	B	0.008	1.8	2.75	1.35
28C44	SOIC8	GW	Alloy42	Epoxy Bisphenol	T	0.75	4.9	3.9	1.58
2pin	conn	TH	Copper	plastic	T	1.5	4.33	11.35	6.07
314217	SO8	GW	Copper	Epoxy Bisphenol	T	0.143	5.1	3.95	3
36pin	conn	TH	Copper	Copper	T	4.5	45.36	5	4.85
6pin	conn	TH	Copper	Copper	T	1.5	7.1	6	5.13
C150	SMDcap	leadless	leadless	BaTiO2	T	0.035	1.61	3.3	1.6
C27	SMDcap	leadless	leadless	BaTiO2	T	0.08	5.13	5.7	1.3
C802	SMDcap	leadless	leadless	BaTiO2	T	0.05	2.2	3.25	2.6
C843	SMDcap	leadless	leadless	BaTiO2	B	0.03	1.6	3.3	1.1
C844	SMDcap	leadless	leadless	BaTiO2	T/B	0.015	1.6	3.3	0.65
HeatSink	heatsink	SolderBall	Copper	Aluminum	T	183.5	63	53.25	42
R10	SMDres	leadless	leadless	Alumina 85%	B	0.05	6.7	3.15	0.55
R100	SMDres	leadless	leadless	Alumina 85%	T/B	0.017	3	1.56	0.55
R937	SMDres	C-Lead	Alloy42	Epoxy Bisphenol	T	0.04	3.1	5.8	1.85
conn	conn	TH	Copper	Copper	T	0.21	6.5	0.77	4.65

Table 31 Appendix: power board component parameters, 2 of 3

Identifier	Pitch (mm)	# I/O	Interconnect Format	IO Span X (mm)	IO Span Y (mm)	Standoff Height (mm)	Solder Height (mm)	Solder Bond Area (mm^2)
nichicon680	3.5	2	Single Inline	0	3.5	0.25	1	3
nichicon220	3.5	2	Single Inline	0	3.5	0.5	1	3
KY100	2.5	2	Single Inline	0	2.5	0.5	1	3
KY1000	5	2	Single Inline	0	5	0.2	1	3
Epcos	10.1	3	Perimeter Array	7.41	7.41	0.1	1	3
1825ADJ	1.3	6	SOT223-5	5.2	6.8	0.1	0.1	0.375
P781F	2.54	4	Dual Inline	2.85	11	0.5	0.1	0.65
A921	0.95	5	Dual Inline	1.8	3	0.1	0.1	0.105
SOT23	2.1	3	SOT23	2.1	2.1	0.1	0.1	0.1125
74LV4066	1.27	14	Dual Inline	7.5	5.7	0.1	0.1	0.2
LM239DG	1.27	14	Dual Inline	7.5	5.7	0.1	0.1	0.2
Transf.	5	10	Dual Inline	20	12	2.5	1	3
RX27	x	2	Axial	x	x	20.5	1	3
RTD14012	8.4	8	Dual Inline	25	7.5	0.5	1	3
A400	1.27	8	Dual Inline	3.85	6.2	0.1	0.1	0.3
22n	15	2	Single Inline	0	15	1	1	3
15nk	5	2	Single Inline	0	5	0.5	1	3
K3747	5.45	3	Single Inline	0	10.9	14.6	1	3
BYG	4.8	2	Single Inline	0	4.8	0.1	0.1	0.3
V844	5.75	2	Single Inline	0	5.75	0.1	0.1	0.43
V150	5.5	2	Single Inline	0	5.5	0.1	0.1	0.45
V802	5.75	2	Single Inline	0	5.75	0.1	0.1	0.45
V850	3.15	2	Single Inline	0	3.15	0.1	0.1	0.22
28C44	1.27	8	Dual Inline	4.9	3.9	0.1	0.1	0.3
2pin	2.4	2	Single Inline	2.4	0	0.1	0.1	0.825
314217	1.27	8	Dual Inline	5	4	0.1	0.1	0.25
36pin	2.35	36	Dual Inline	42.45	3.1	0.1	0.1	0.825
6pin	2.65	6	Dual Inline	5.3	3	0.1	0.1	0.825
C150	x	2	SMD	x	x	0.1	0.1	0.48
C27	5.7	2	SMD	0	5.7	0.1	0.1	6.75
C802	x	2	SMD	x	x	0.1	0.1	0.77
C843	x	2	SMD	x	x	0.1	0.1	0.48
C844	x	2	SMD	x	x	0.1	0.1	0.48
HeatSink	4	24	Full Array	60	50	16	1	7.24
R10	x	2	SMD	x	x	0.1	0.1	0.47
R100	x	2	SMD	x	x	0.1	0.1	0.47
R937	6.42	2	C-Lead	x	x	0.1	0.1	1.2
conn	5.12	2	Single Inline	5.12	0	0.1	0.75	14

Table 32 Appendix: power board component parameters, 3 of 3

Identifier	Position of Paddle (mm)	Length of Paddle (mm)	Width of Paddle (mm)	Max Rated Temperature C	Theta JC (C/W)
nichicon680	x	x	x	105	40
nichicon220	x	x	x	105	40
KY100	x	x	x	105	40
KY1000	x	x	x	105	40
Epcos	x	x	x	85	40
1825ADJ	0.7	2.17	1.75	150	20
P781F	1.65	1.53	3.25	125	50
A921	0.45	0.97	0.775	150	20
SOT23	0.35	0.97	0.65	150	20
74LV4066	0.6	2.88	1.95	150	40
LM239DG	0.6	2.88	1.95	150	40
Transf.	x	x	x	150	10
RX27	x	x	x	155	40
RTD14012	x	x	x	85	25
A400	0.69	1.63	1.95	150	40
22n	x	x	x	125	40
15nk	x	x	x	125	40
K3747	10.9	5.33	2.175	150	2.4
BYG	0.925	0.87	2.05	150	25
V844	1	1.17	2.2	150	25
V150	1	0.93	2.15	150	25
V802	0.9	0.87	2.25	150	25
V850	0.575	0.60	1.375	150	15
28C44	0.69	1.63	1.95	150	40
2pin	x	x	x	125	60
314217	1.4	1.70	1.975	150	40
36pin	x	x	x	125	60
6pin	x	x	x	125	60
C150	x	x	x	125	35
C27	x	x	x	125	35
C802	x	x	x	125	35
C843	x	x	x	125	35
C844	x	x	x	125	35
HeatSink	x	x	x	500	10
R10	x	x	x	125	32
R100	x	x	x	125	32
R937	x	x	x	150	20
conn	x	x	x	150	20

Infrared Images

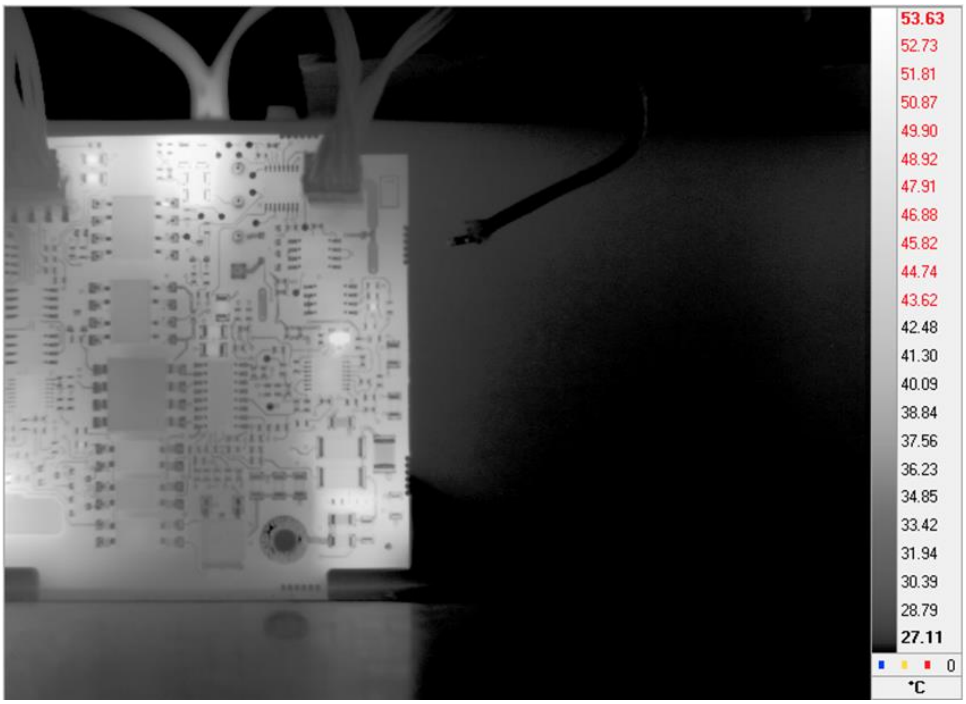

Figure 80 Appendix: IR control board back right

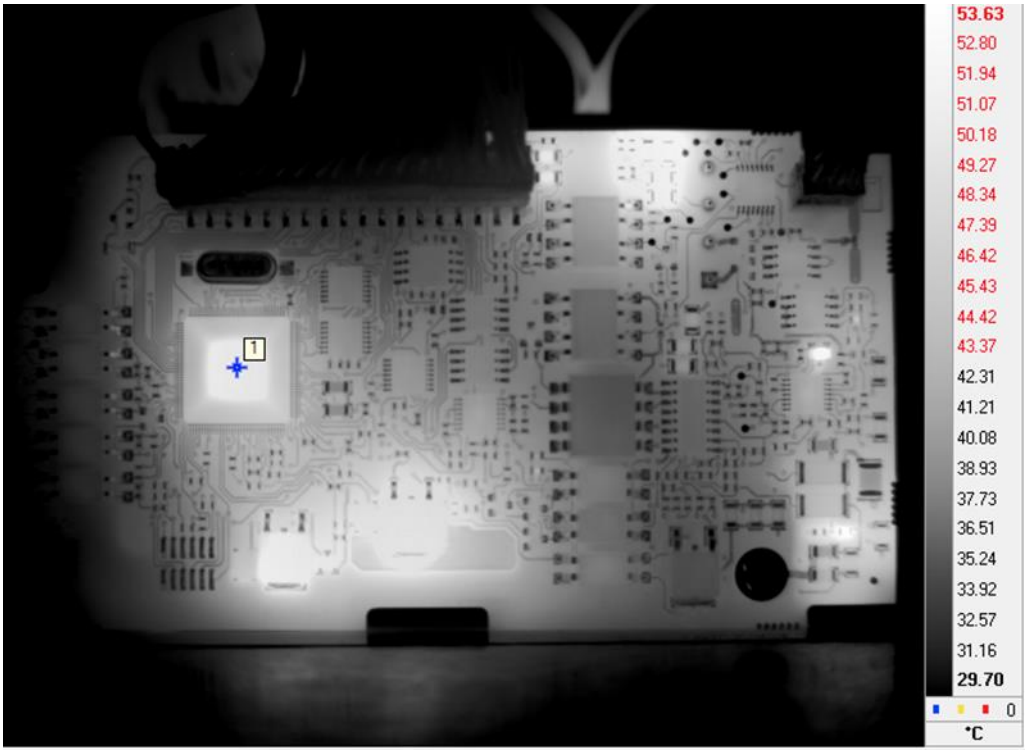

Figure 81 Appendix: IR control board back center

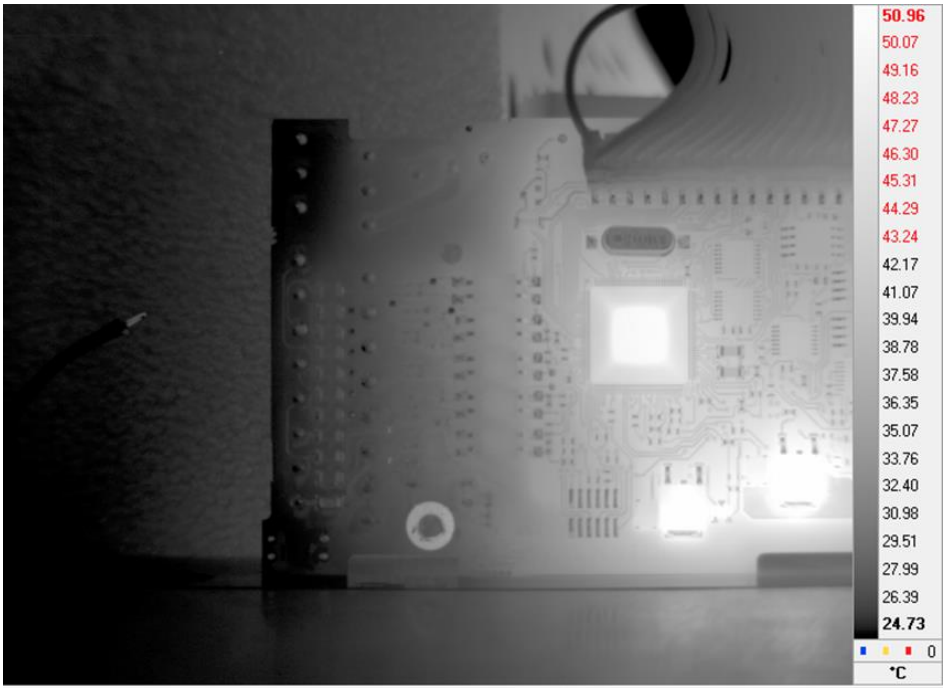

Figure 82 Appendix: IR control board back left

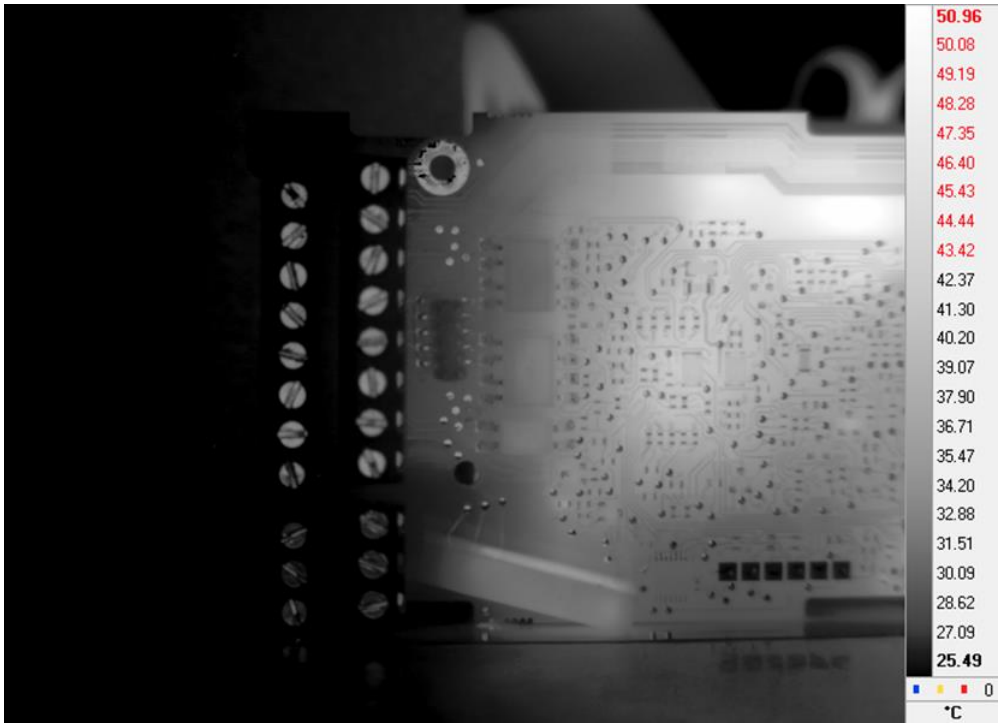

Figure 83 Appendix: IR control board front left

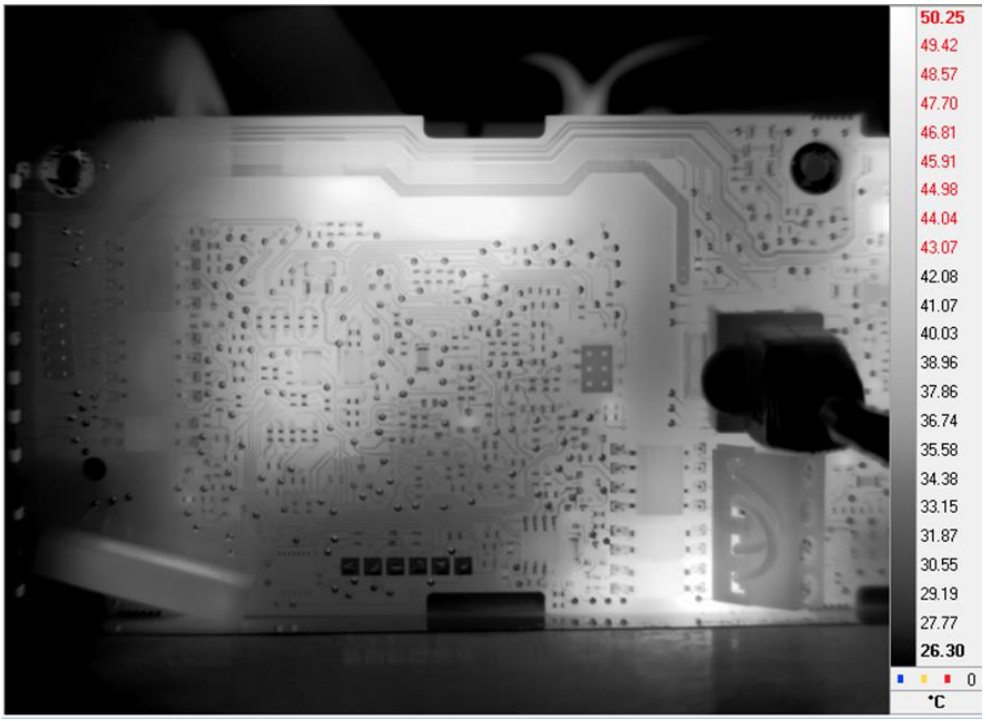

Figure 84 Appendix: IR control board front center

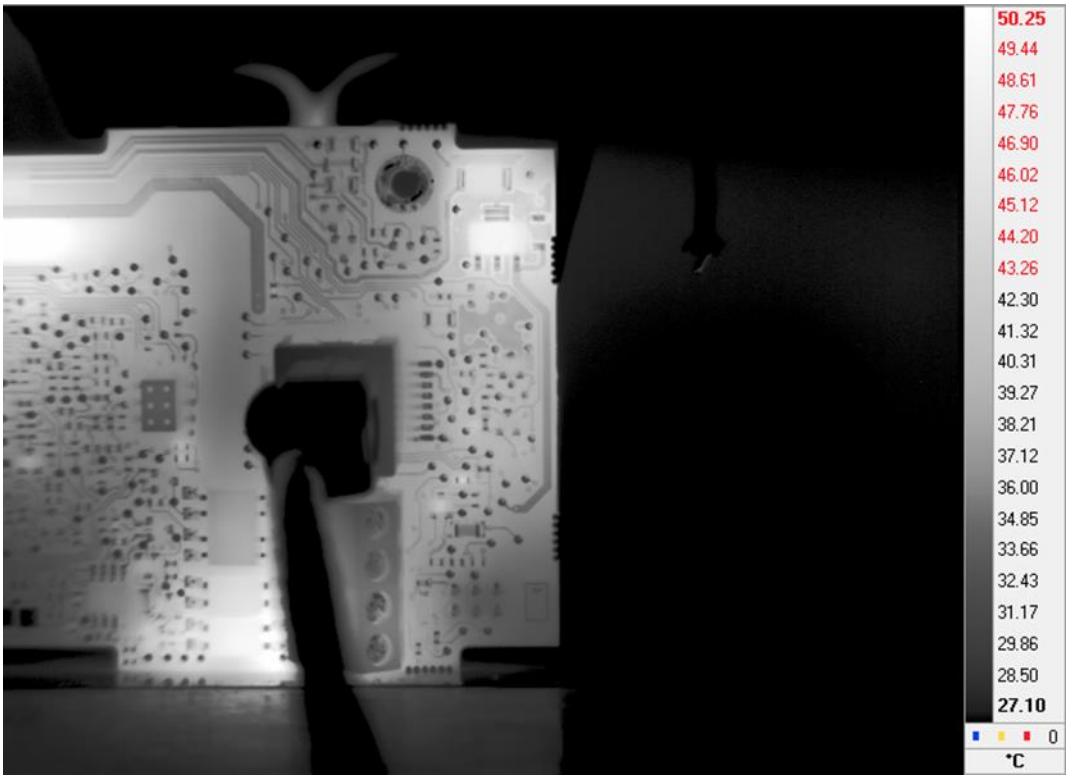

Figure 85 Appendix: IR control board front right

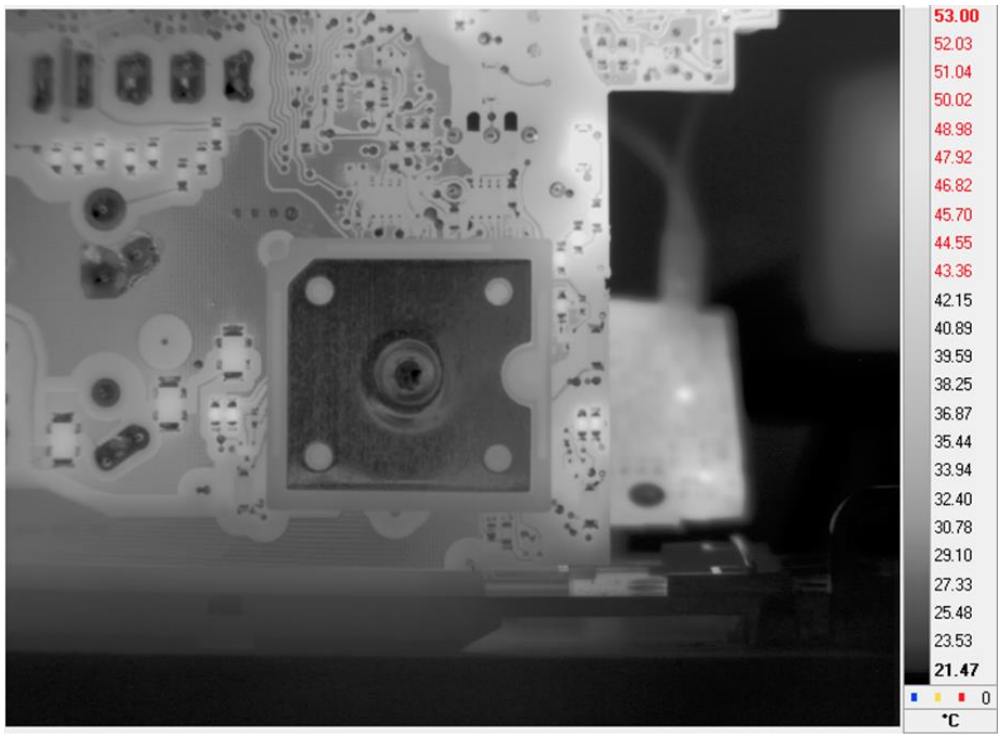

Figure 86 Appendix: IR power board idle back bottom right

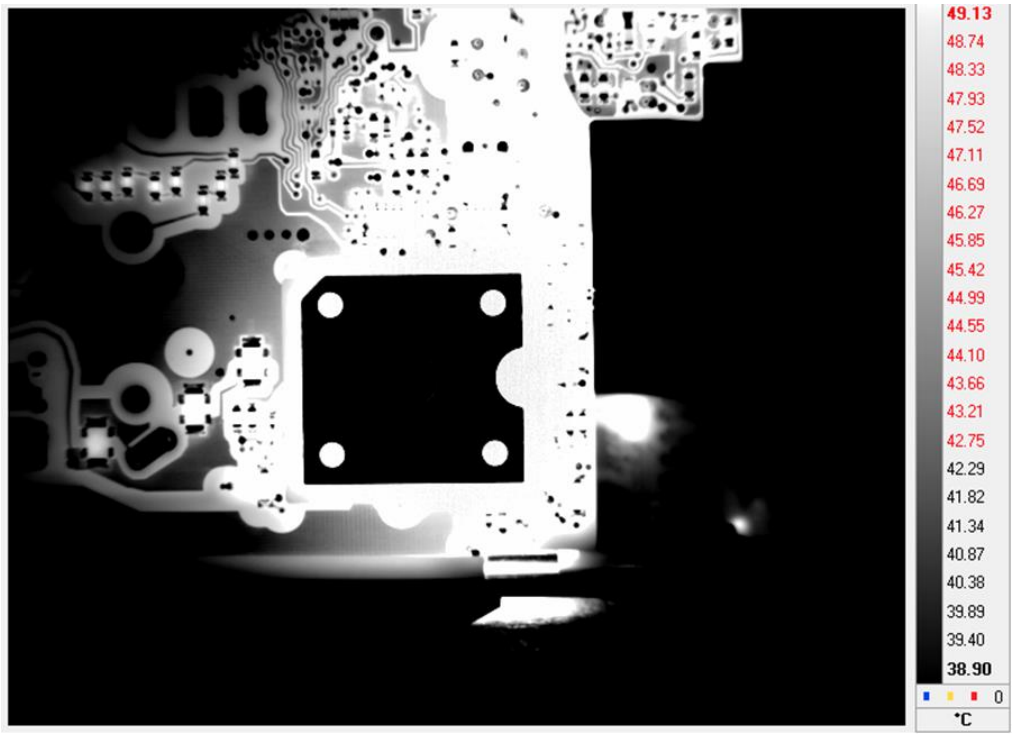

Figure 87 Appendix: IR power board load back bottom right

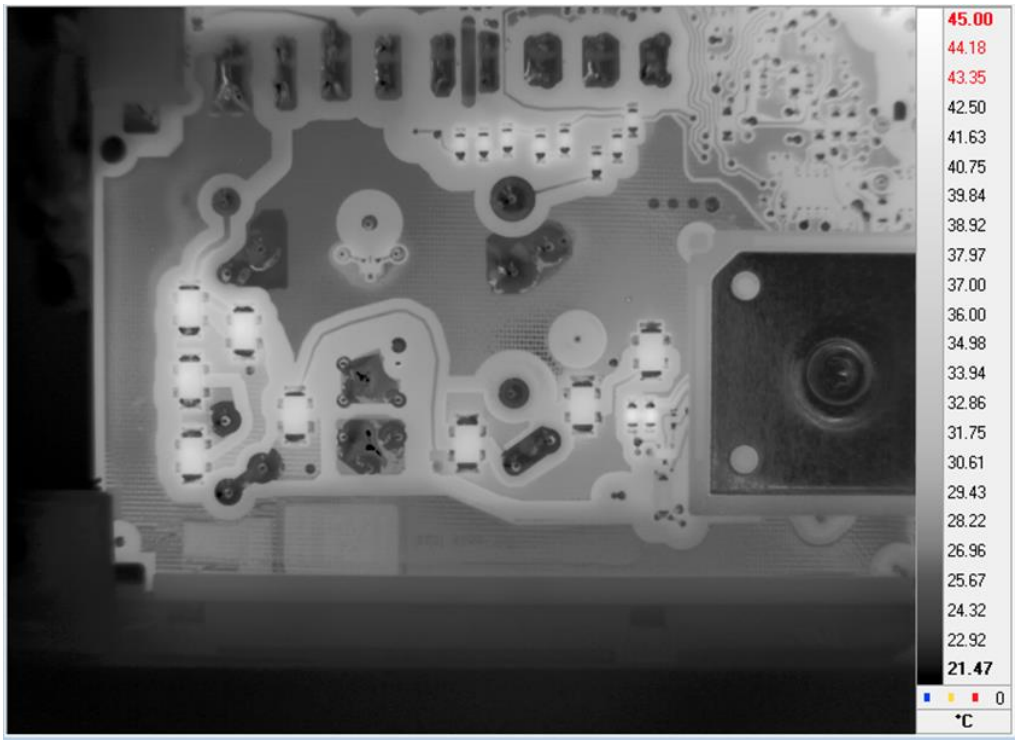

Figure 88 Appendix: IR power board idle back bottom left

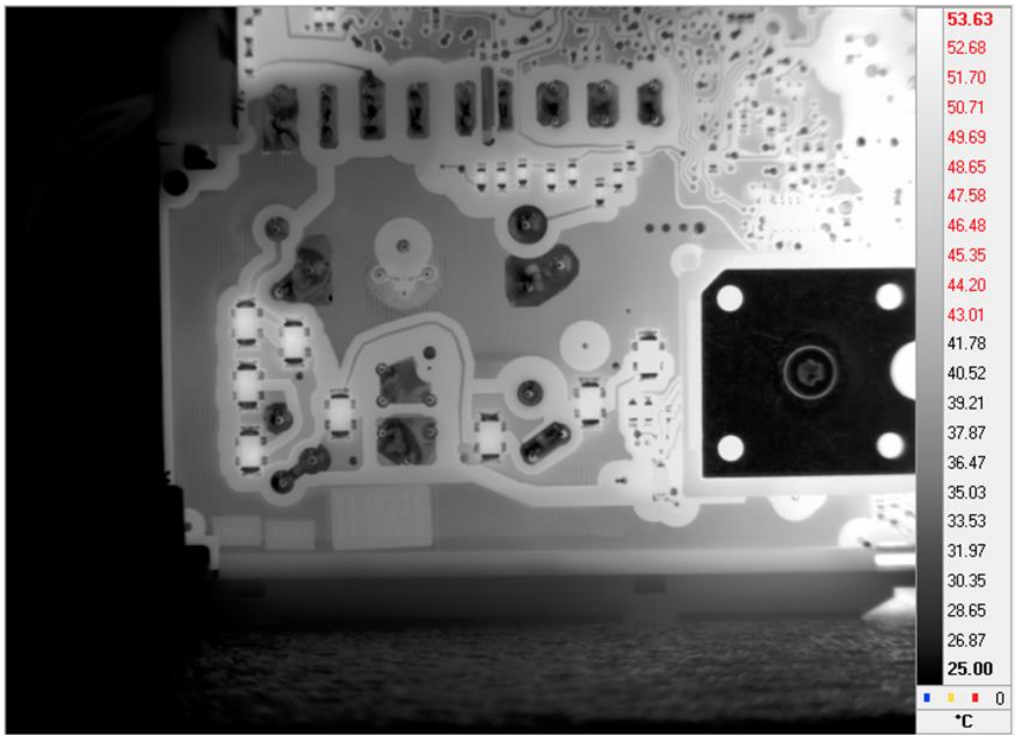

Figure 89 Appendix: IR power board load back bottom left

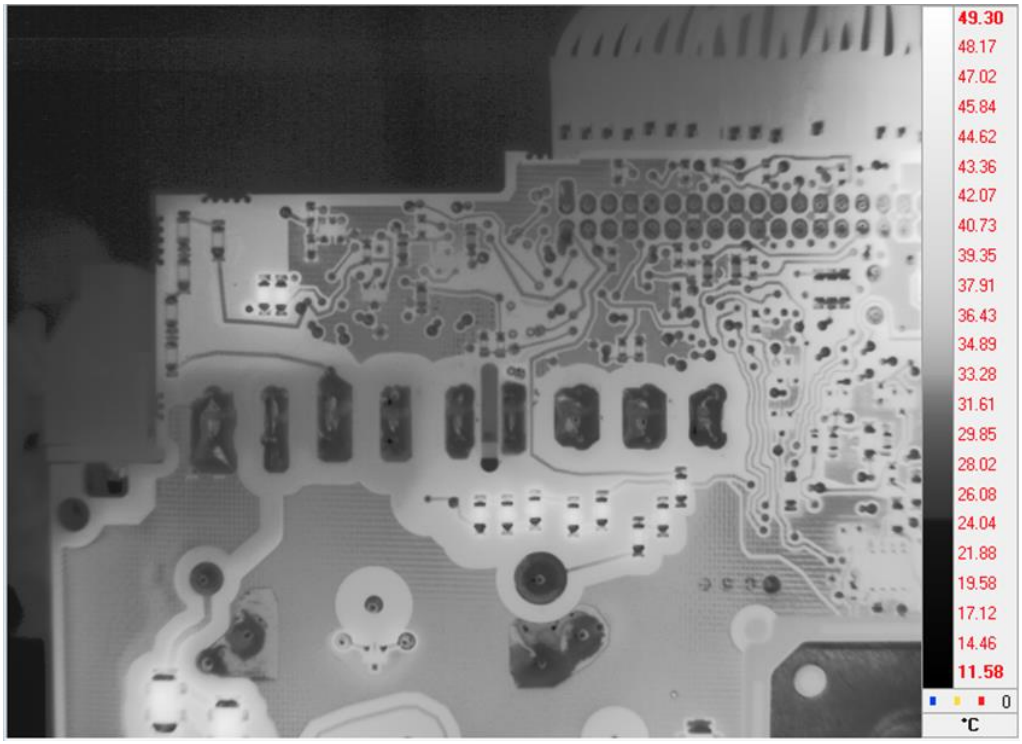

Figure 90 Appendix: IR power board idle back upper left

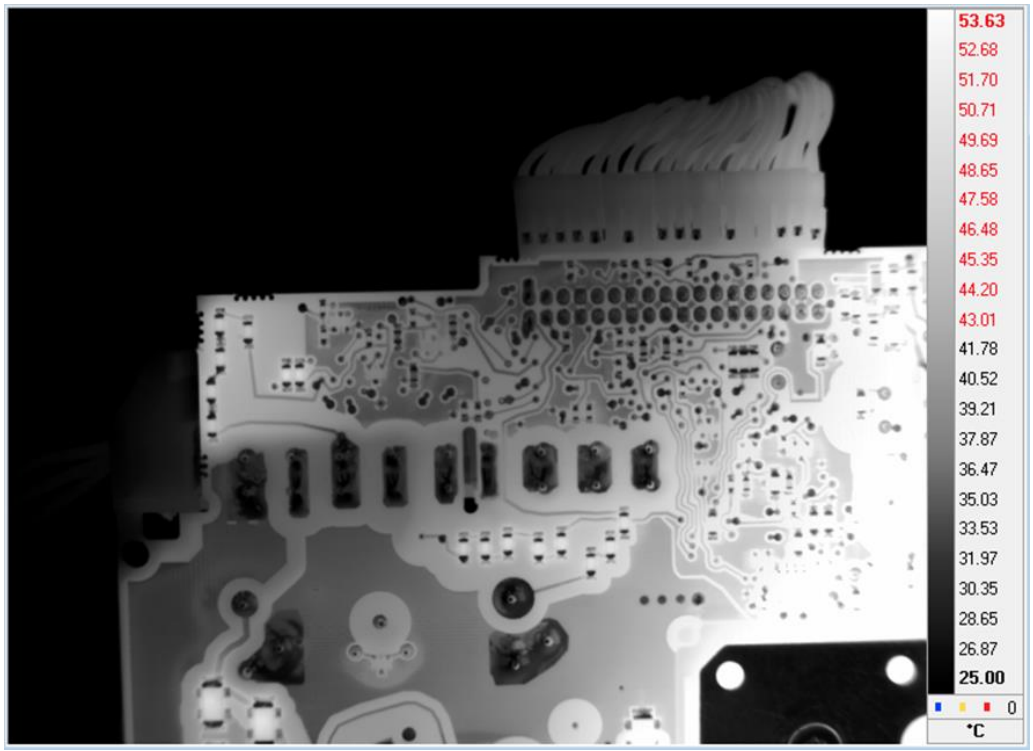

Figure 91 Appendix: IR power board load back upper right

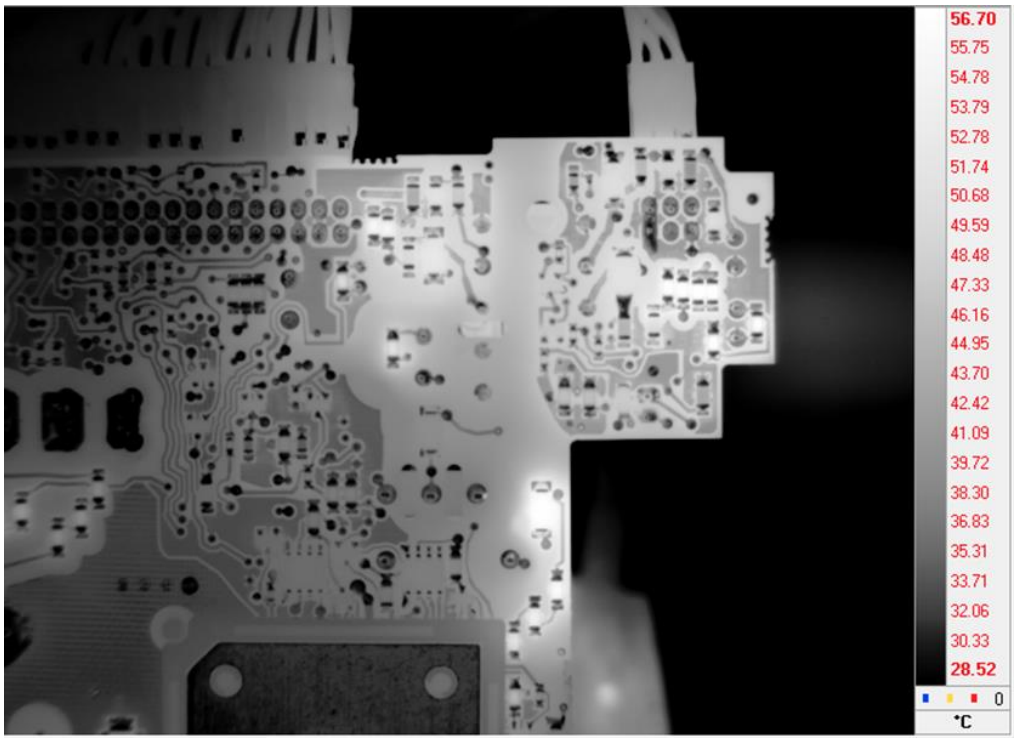

Figure 92 Appendix: IR power board idle back upper right

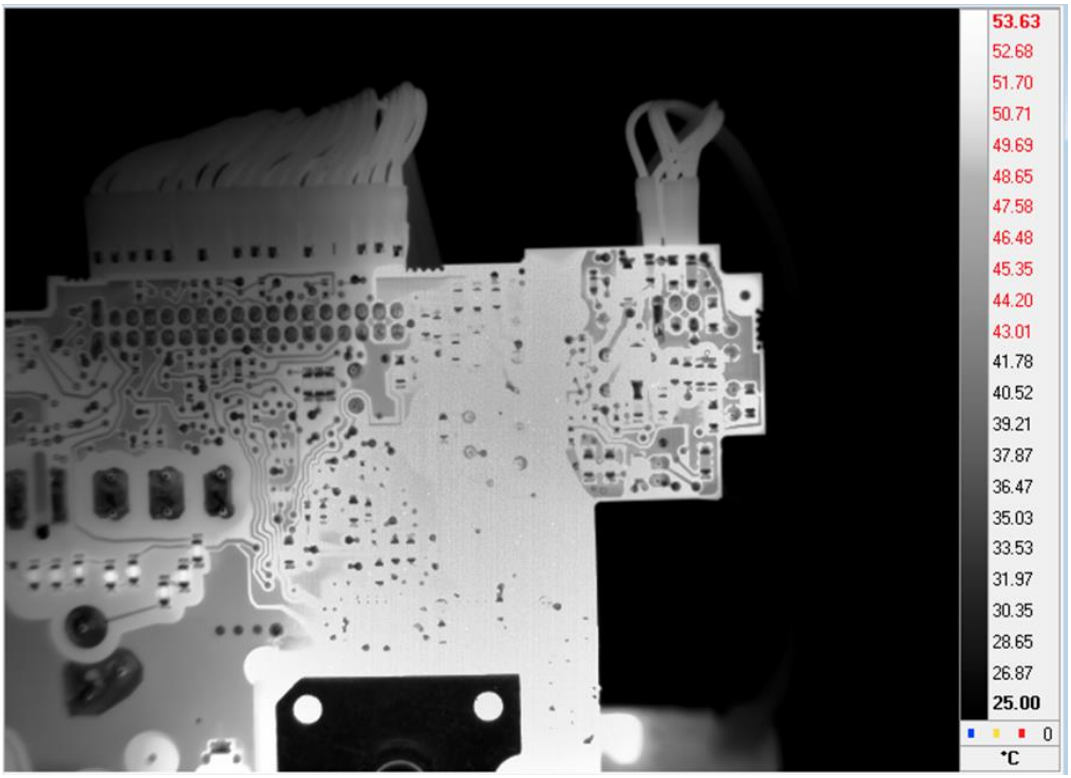

Figure 93 Appendix: IR power board load back upper right

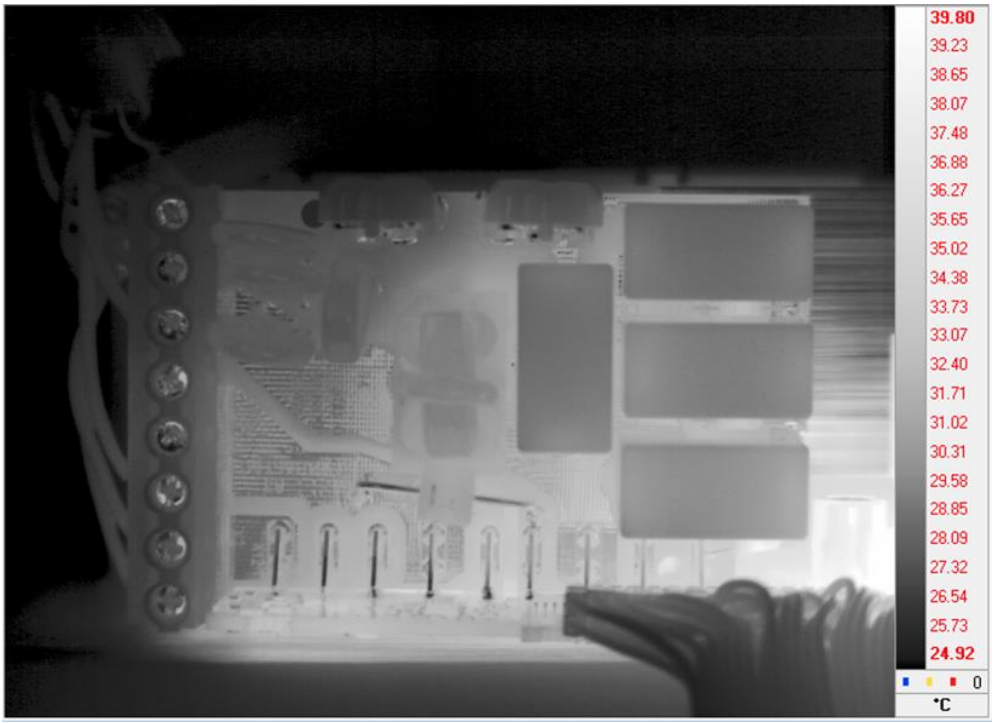

Figure 94 Appendix: IR connector board idle

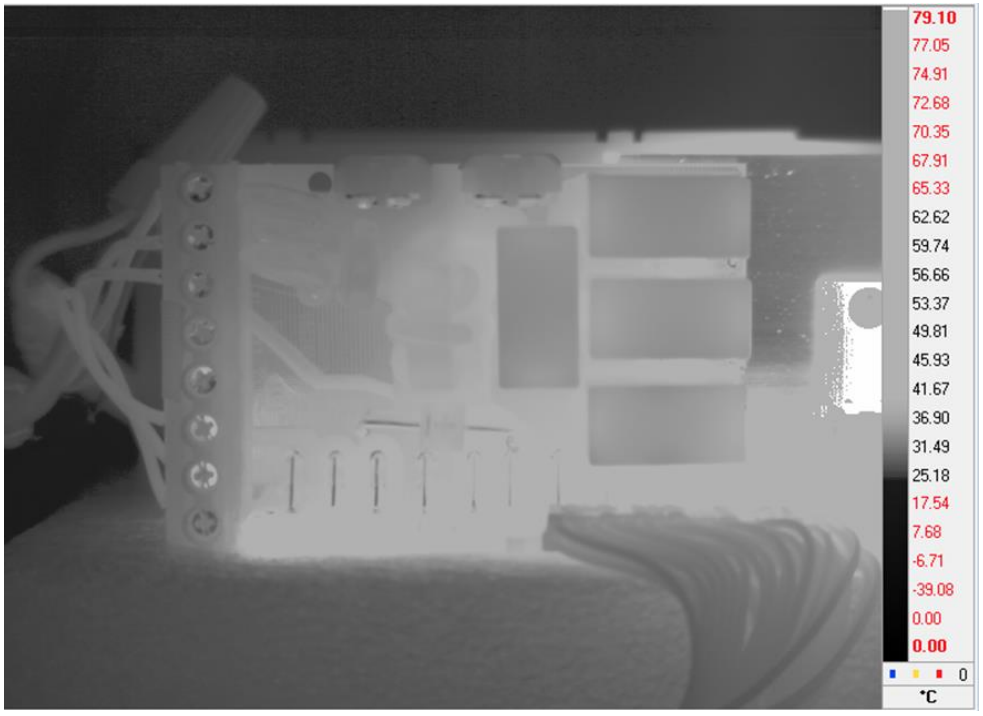

Figure 95 Appendix: IR connector board load

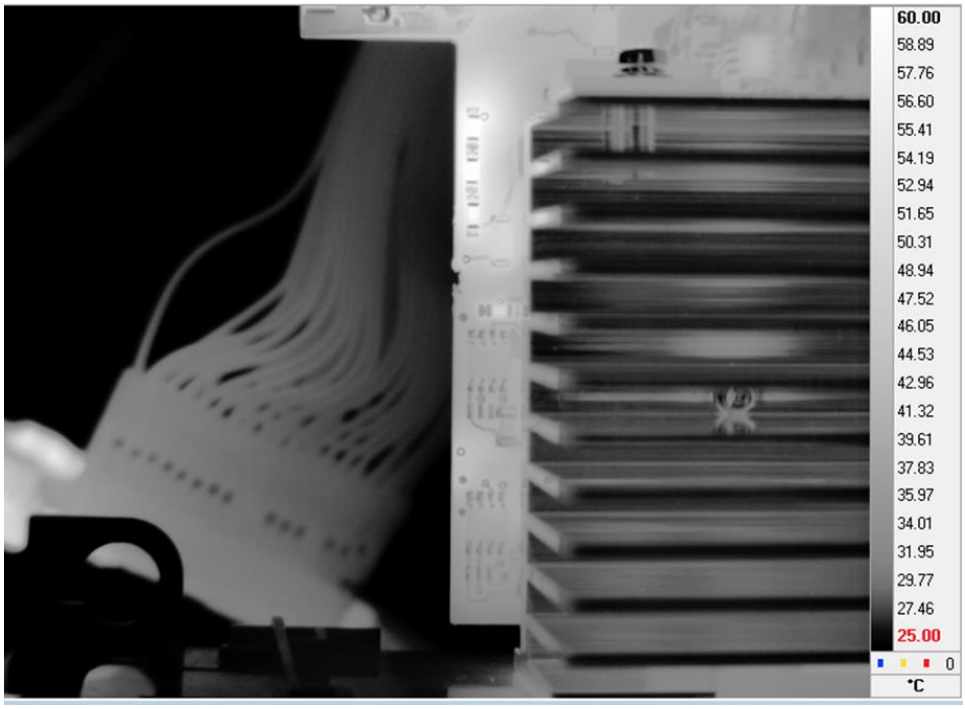

Figure 96 Appendix: IR power board idle IGBT side passives

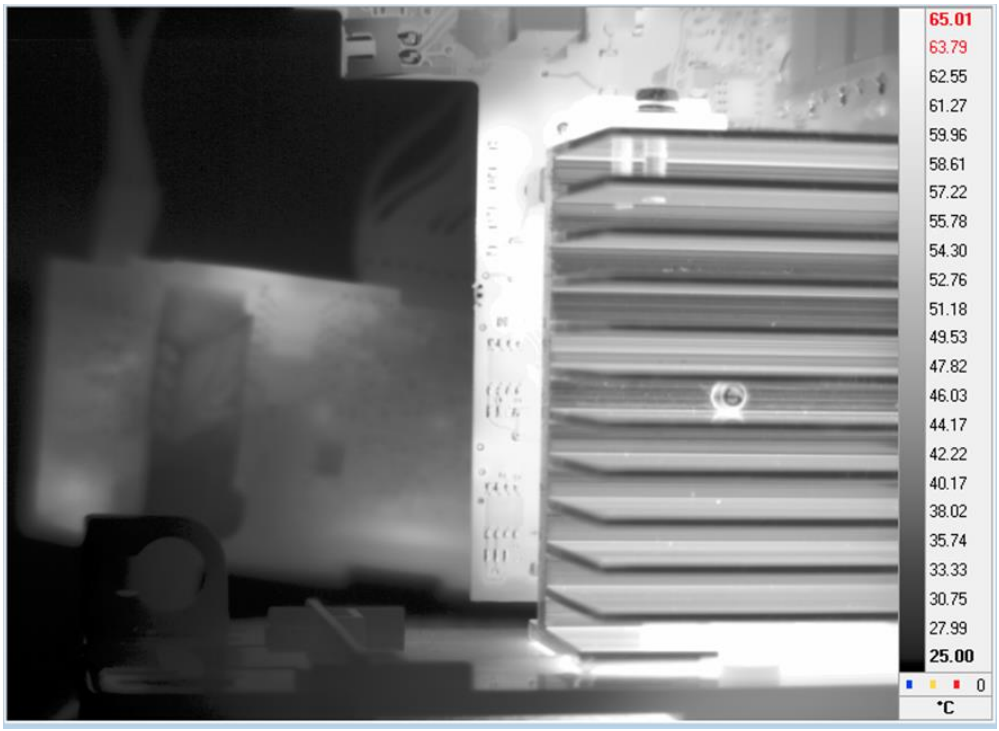

Figure 97 Appendix: IR power board load IGBT side passives

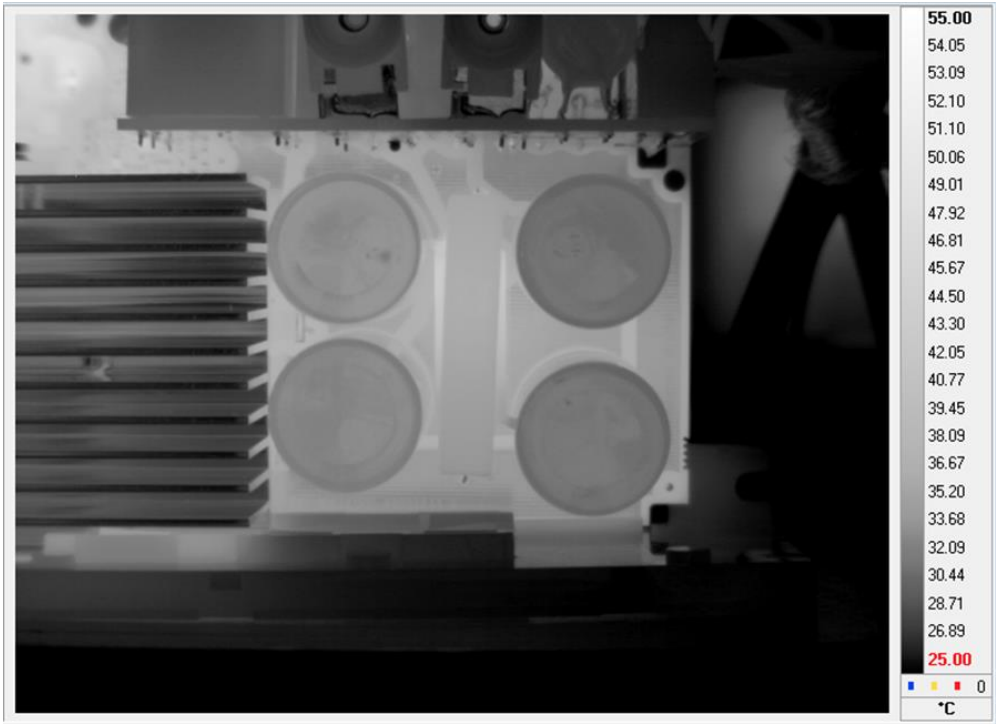

Figure 98 Appendix: IR power board idle electrolytic capacitors

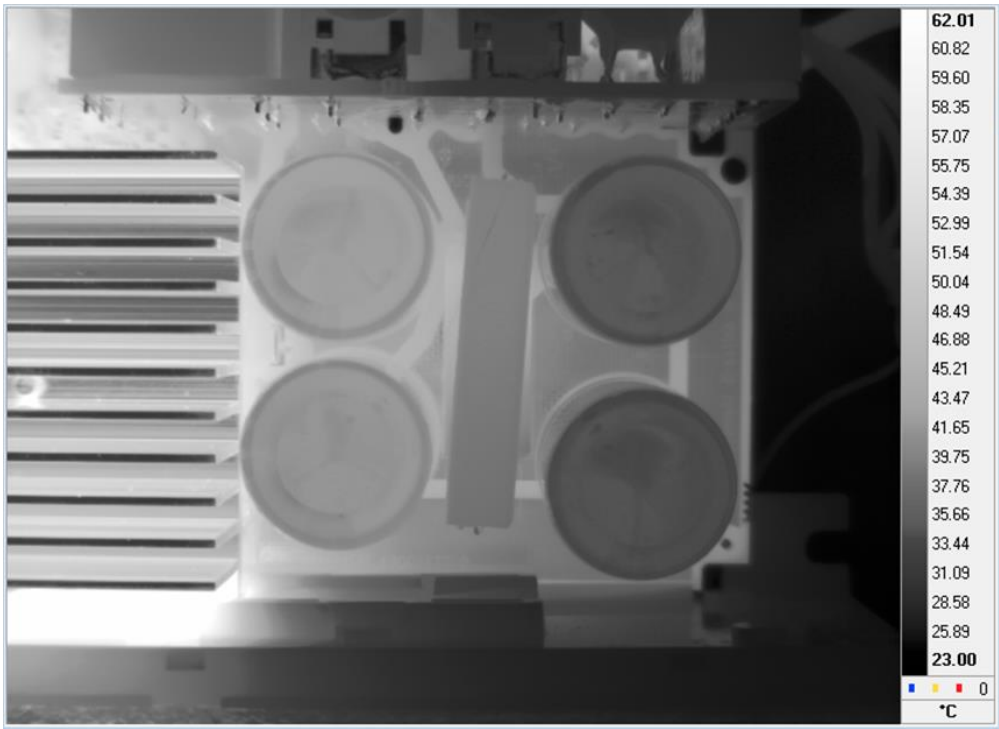

Figure 99 Appendix: IR power board load electrolytic capacitors

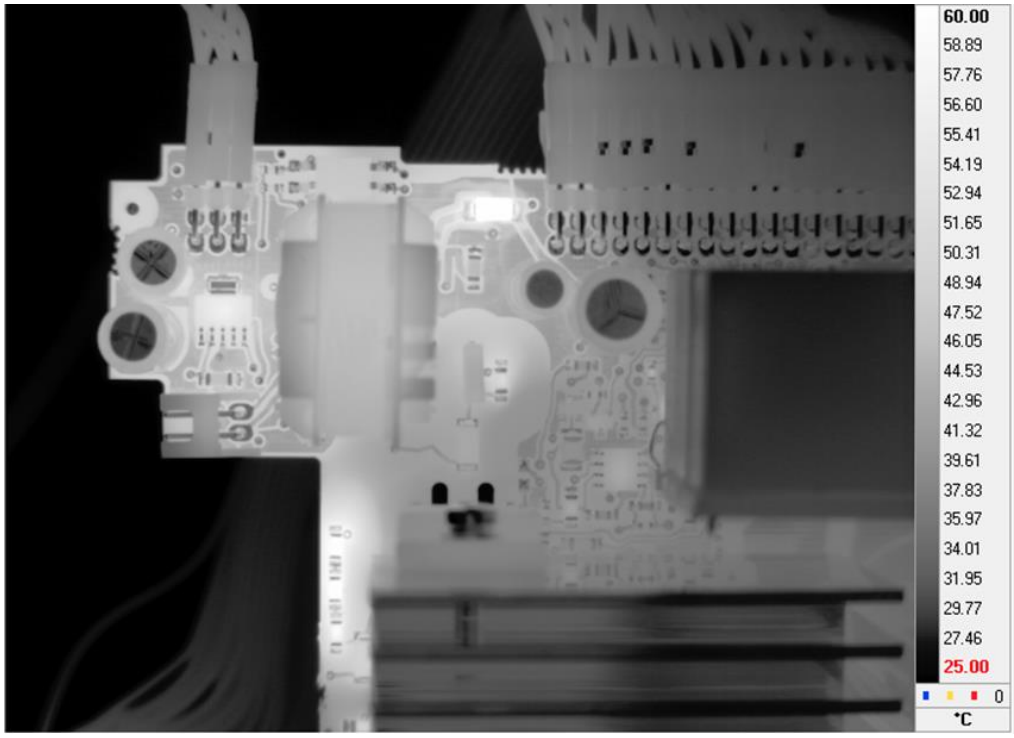

Figure 100 Appendix: IR power board idle front upper left

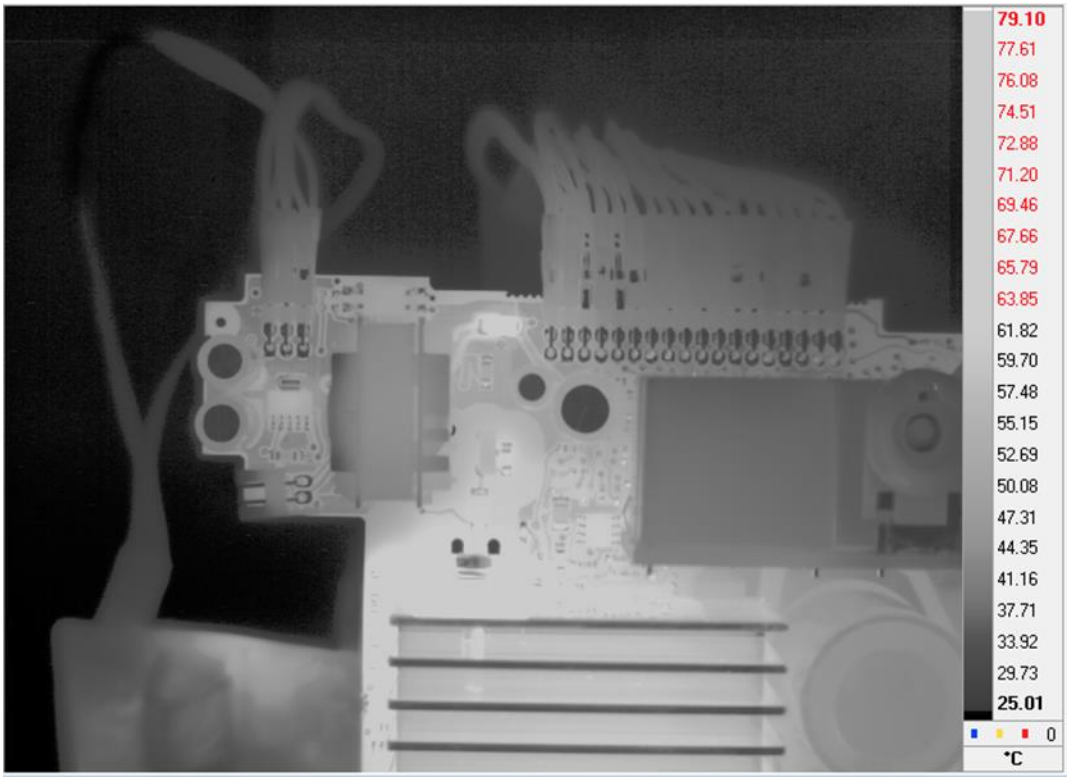

Figure 101 Appendix: IR power board load front upper right

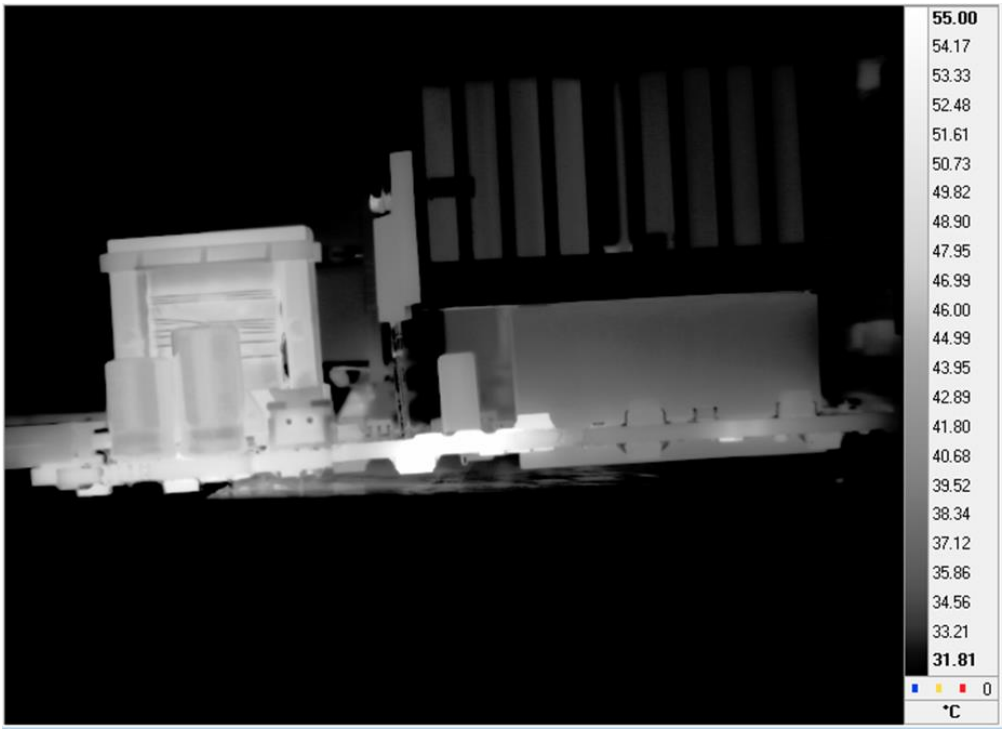

Figure 102 Appendix: IR power board idle IGBT side view

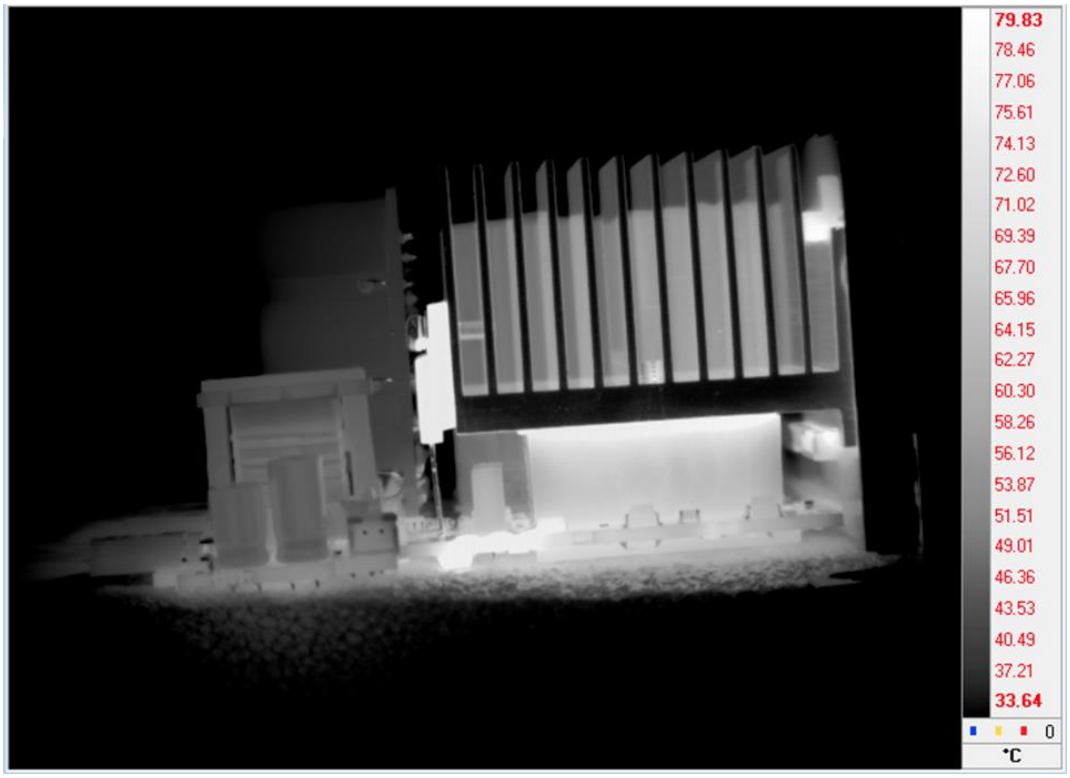

Figure 103 Appendix: IR power board load IGBT side view

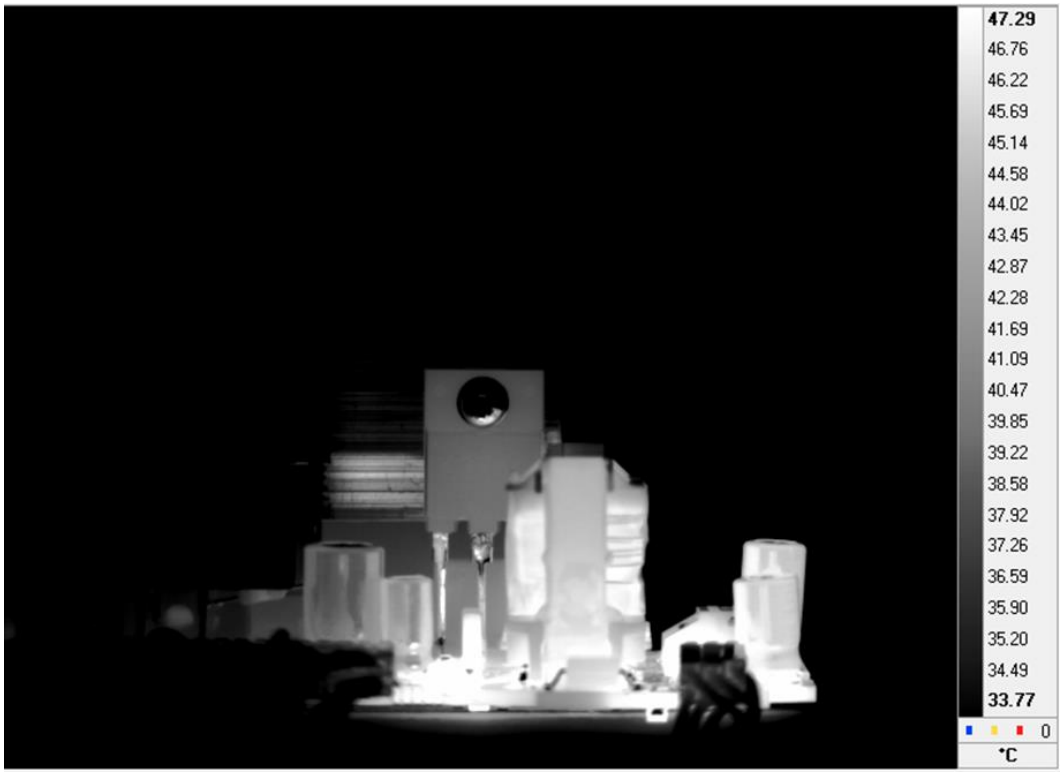

Figure 104 Appendix: IR power board idle MOSFET and inductor

Figure 105 Appendix: IR power board idle front upper right

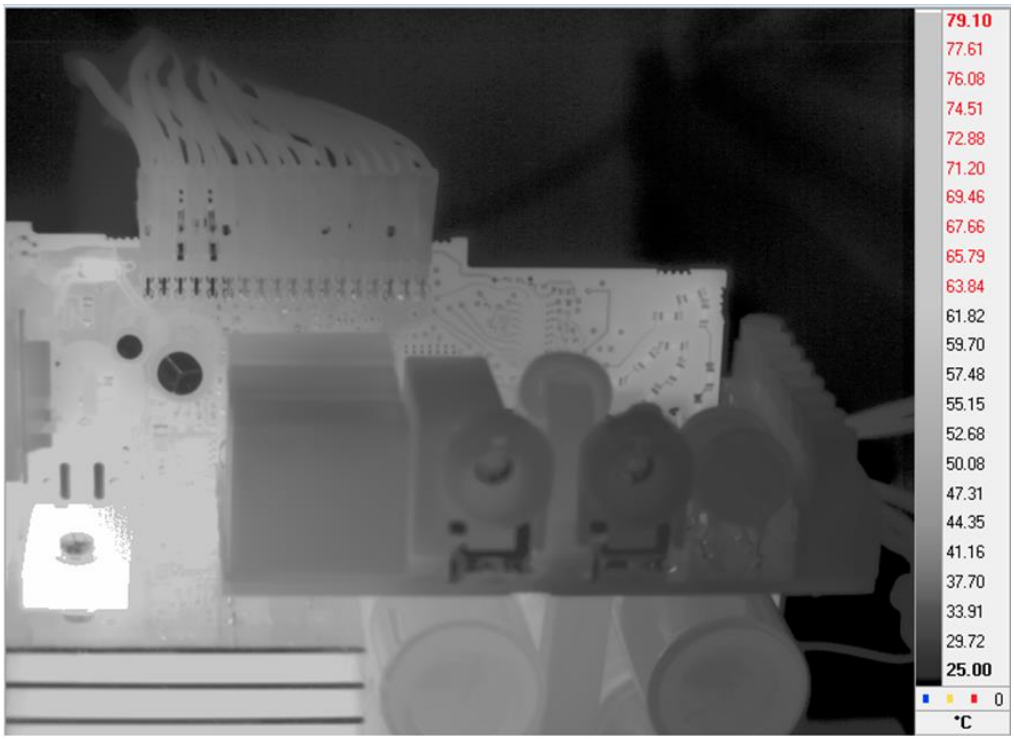

Figure 106 Appendix: IR power board load front upper right

Natural Convection Thermal Profiles

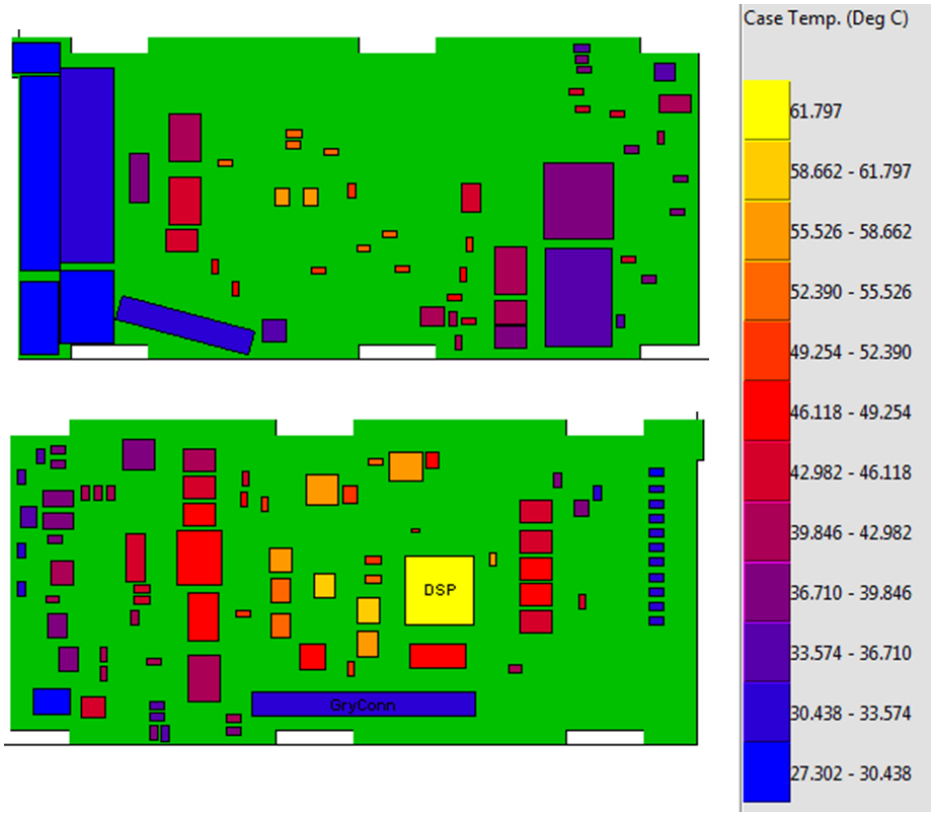

Figure 107 Appendix: thermal profile control board natural convection

Table 33 Appendix: simulation parameters for thermal profile - natural convection control board

Analysis Type	Conduction with Natural Convection
Max Iterations	1000
Ambient / Surrounding Temperature	27.0°C
Space Above Top Surface	10 mm
Space Below Bottom Surface	20 mm
Nodes in X-Direction	50
Nodes in Y-Direction	50

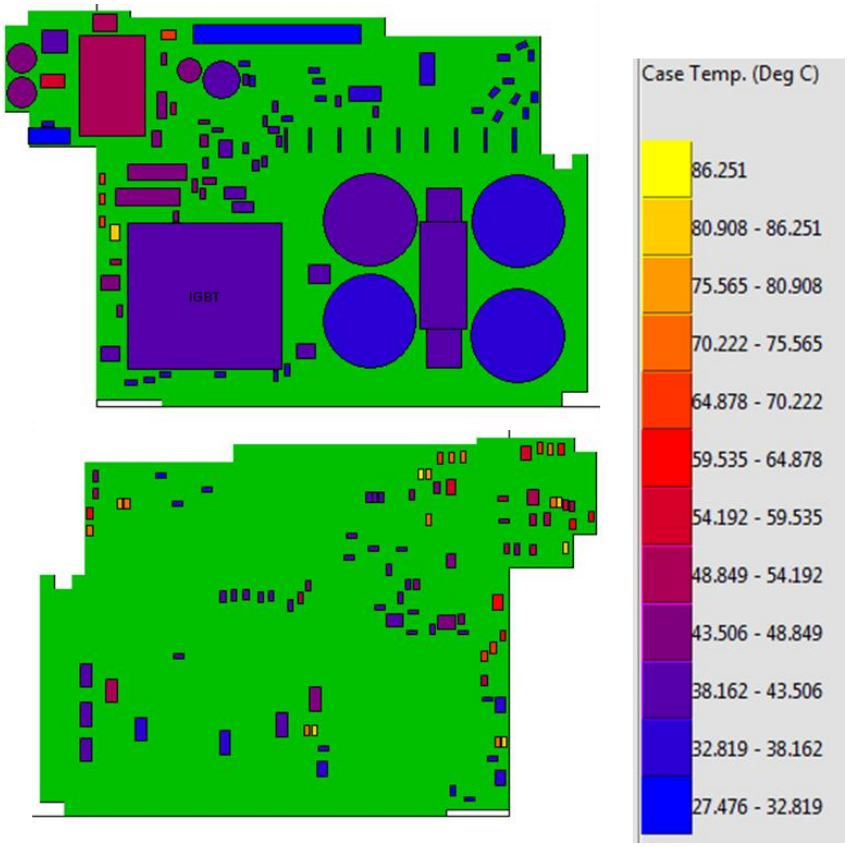

Figure 108 Appendix: thermal profile power board natural convection idle

Table 34 Appendix: simulation parameters for thermal profile - natural convection power board idle

Analysis Type	Conduction with Natural Convection
Max Iterations	1000
Ambient / Surrounding Temperature	26.2°C
Space Above Top Surface	5 mm
Space Below Bottom Surface	50 mm
Nodes in X-Direction	50
Nodes in Y-Direction	50

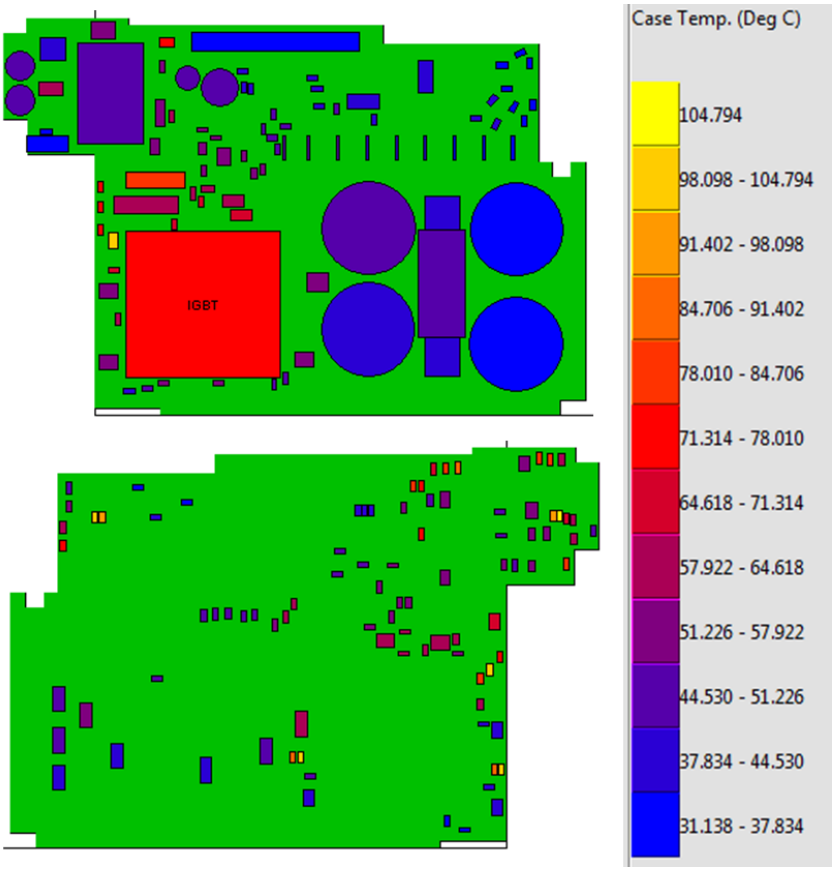

Figure 109 Appendix: thermal profile power board natural convection load

Table 35 Appendix: simulation parameters for thermal profile - natural convection power board load

Analysis Type	Conduction with Natural Convection
Max Iterations	1000
Ambient / Surrounding Temperature	28.0°C
Space Above Top Surface	5 mm
Space Below Bottom Surface	50 mm
Nodes in X-Direction	50
Nodes in Y-Direction	50

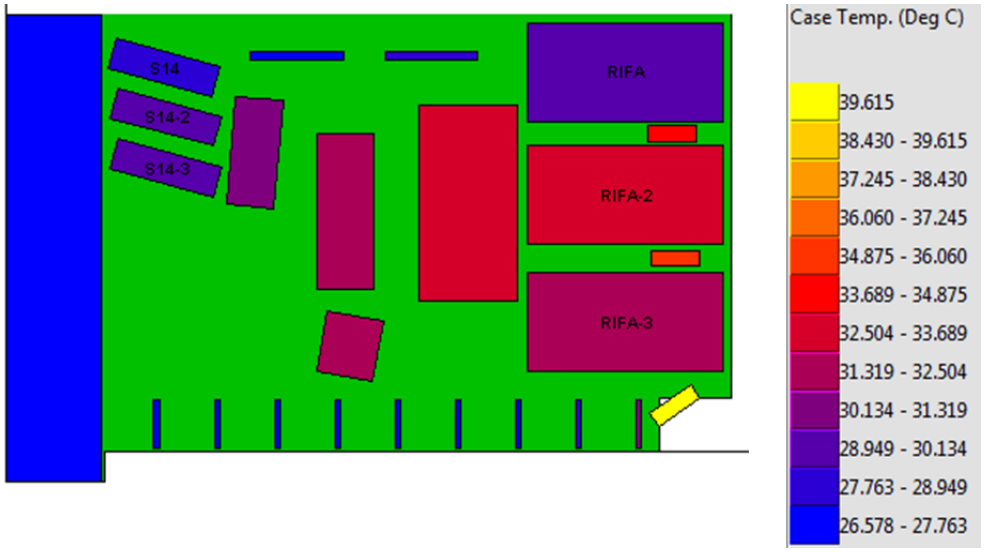

Figure 110 Appendix: thermal profile connector board natural convection idle

Table 36 Appendix: simulation parameters for thermal profile - natural convection connector board idle

Analysis Type	Conduction with Natural Convection
Max Iterations	1000
Ambient / Surrounding Temperature	26.2°C
Space Above Top Surface	25 mm
Space Below Bottom Surface	10 mm
Nodes in X-Direction	50
Nodes in Y-Direction	50

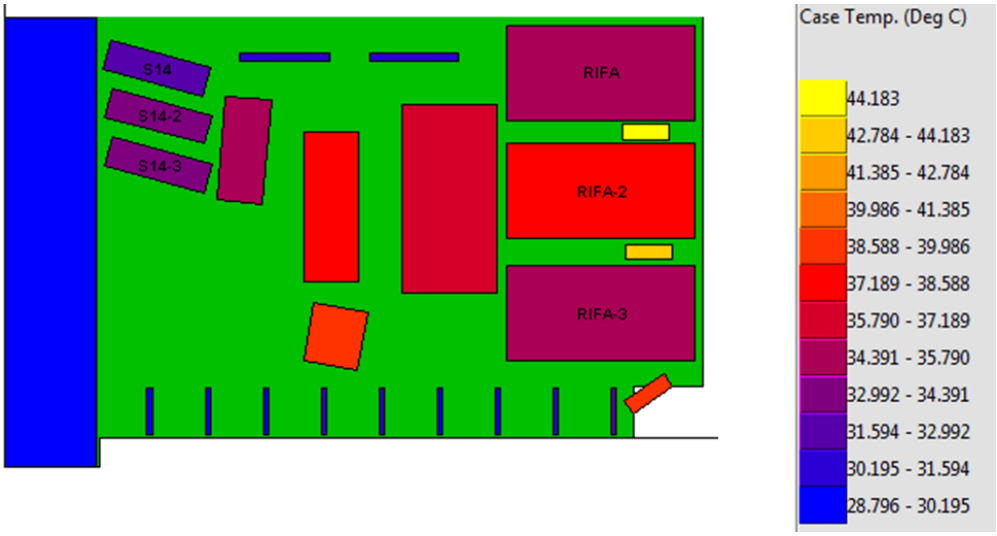

Figure 111 Appendix: thermal profile connector board natural convection load

Table 37 Appendix: simulation parameters for thermal profile - natural convection connector board load

Analysis Type	Conduction with Natural Convection
Max Iterations	1000
Ambient / Surrounding Temperature	26.2°C
Space Above Top Surface	25 mm
Space Below Bottom Surface	10 mm
Nodes in X-Direction	50
Nodes in Y-Direction	50

References

[1] Bose, Bimal K. *Modern Power Electronics: Evolution, Technology, and Applications*. New York: Institute of Electrical and Electronics Engineers, 1992. Print.

[2] Rashid, Muhammad H. *Power Electronics Handbook*. San Diego: Academic, 2001. Print

[3] Krein, P.T. *Elements of Power Electronics*. New York: Oxford UP, 1998. Print.

[4] Bose, Bimal K. *Power Electronics and Motor Drives: Advances and Trends*. Amsterdam: Elsevier/Academic, 2006. Print.

[5] Yantao Song; Bingsen Wang, "Survey on Reliability of Power Electronic Systems," *Power Electronics, IEEE Transactions on* , vol.28, no.1, pp.591,604, Jan. 2013

[6] Ristow, A.; Begovic, M.; Pregelj, A.; Rohatgi, A., "Development of a Methodology for Improving Photovoltaic Inverter Reliability," *Industrial Electronics, IEEE Transactions on* , vol.55, no.7, pp.2581,2592, July 2008

[7] Smater, S.S.; Dominguez-Garcia, A.D., "A unified framework for reliability assessment of wind energy conversion systems," *Power and Energy Society General Meeting, 2010 IEEE* , vol., no., pp.1,4, 25-29 July 2010.

[8] "Variable-Frequency Drive." California Energy Commission, n.d. Web. <http://www.energy.ca.gov/process/pubs/vfds.pdf>.

[9] "Mechanical Speed Adjustment." *Machine Design*. N.p., n.d. Web. 28 Aug. 2013. <http://machinedesign.com/mechanical-drives/mechanical-speed-adjustment>.

[10] Van Wyk, J.D.; Lee, F.C., "On a Future for Power Electronics," *Emerging and Selected Topics in Power Electronics, IEEE Journal of* , vol.1, no.2, pp.59,72, June 2013

[11] Power Switching Module Datasheet <http://www.semikron.com/products/data/cur/assets/SKiiP_11NAB065V1_25230230.pdf>

[12] Eighth International Conference on Power Electronics and Variable Speed Drives: 18-19 September 2000 : Venue, IEE, Savoy Place, London, UK. London: IEE, 2000. Print.

[13] Michael Pecht, Diganta Das, Arun Ramakrishnana, The IEEE standards on reliability program and reliability prediction methods for electronic equipment, Microelectronics Reliability, Volume 42, Issues 9–11, September–November 2002, Pages 1259-1266

[14] Pecht, M.; Dasgupta, A., "Physics-of-failure: an approach to reliable product development," *Integrated Reliability Workshop, 1995. Final Report., International* , vol., no., pp.1,4, 22-25 Oct. 1995

[15] Hornberger, J.; Lostetter, A.B.; Olejniczak, K.J.; McNutt, T.; Lal, S.M.; Mantooth, A., "Silicon-carbide (SiC) semiconductor power electronics for extreme high-temperature environments," *Aerospace Conference, 2004. Proceedings. 2004 IEEE* , vol.4, no., pp.2538,2555 Vol.4, 13-13 March 2004

[16] Cyril Buttay, Dominique Planson, Bruno Allard, Dominique Bergogne, Pascal Bevilacqua, Charles Joubert, Mihai Lazar, Christian Martin, Hervé Morel, Dominique Tournier, Christophe Raynaud, State of the art of high temperature power electronics, Materials Science and Engineering: B, Volume 176, Issue 4, 15 March 2011, Pages 283-288

[17] I.S. Mehdi, A.E. Brockschmidt, K.J. Karimi, Proceedings of the High Temperature Electronics Conference (HiTEC), IMAPS, Santa Fe, NM (2006)

[18] Van Wyk, J.D.; Lee, F.C., "Power electronics technology at the dawn of the new millenium-status and future," *Power Electronics Specialists Conference, 1999. PESC 99. 30th Annual IEEE* , vol.1, no., pp.3,12 vol.1, Aug 1999

[19] Lee, F.C.; Van Wyk, J.D.; Liang, Z.X.; Chen, R.; Wang, S.; Lu, B., "An integrated power electronics modular approach: concept and implementation," *Power Electronics and Motion Control Conference, 2004. IPEMC 2004. The 4th International* , vol.1, no., pp.1,13 Vol.1, 14-16 Aug. 2004

[20] McCluskey, P., "Reliability of Power Electronics Under Thermal Loading," *Integrated Power Electronics Systems (CIPS), 2012 7th International Conference on* , vol., no., pp.1,8, 6-8 March 2012

[21] Siepe, D., Bayerer, R., Roth, R., “The Future of Wire Bonding is? Wire Bonding!,” CIPS 2010

[22] Guth, K., Siepe, D., Gorlich, J., Torwesten, H., Roth, R., Hille, F., Umbach, F., “New Assembly and Interconnects beyond Sintering Methods,” PCIM 2010

[23] Bailey, C.; Lu, H.; Tilford, T., "Predicting the Reliability of Power Electronic Modules," *Electronic Packaging Technology, 2007. ICEPT 2007. 8th International Conference on* , vol., no., pp.1,5, 14-17 Aug. 2007

[24] Hua Lu, Chris Bailey, Chunyan Yin, Design for reliability of power electronics modules, Microelectronics Reliability, Volume 49, Issues 9–11, September–November 2009, Pages 1250-1255

[25] Lorenz, R.D., "The future of electric drives: where are we headed?," Power Electronics and Variable Speed Drives, 2000. Eighth International Conference on (IEE Conf. Publ. No. 475) , vol., no., pp.1,6, 2000

[26] Wikstrom, P.; Terens, L.A.; Kobi, H., "Reliability, availability, and maintainability of high-power variable-speed drive systems," *Industry Applications, IEEE Transactions on* , vol.36, no.1, pp.231,241, Jan/Feb 2000

[27] Bazzi, A.M.; Dominguez-Garcia, A.; Krein, P.T., "Markov Reliability Modeling for Induction Motor Drives Under Field-Oriented Control," *Power Electronics, IEEE Transactions on* , vol.27, no.2, pp.534,546, Feb. 2012

[28] CalcePWA Documentation <http://www.calce.umd.edu/software/>

[29] CalcePWA Documentation <http://www.calce.umd.edu/software/calcePWA-040406.pdf >

[30] Suppa, M.; Schauer, C., "Thick film coating materials and fast conformal coating processes - a contradiction?," *Polymers and Adhesives in Microelectronics and Photonics, 2002. POLYTRONIC 2002. 2nd International IEEE Conference on* , vol., no., pp.165,171, 2002

[31] http://www.panasonic.com/industrial/components/pdf/AOA0000CE1.pdf

[32] Gulbahce, M.O.; Kocabas, D.A.; Habir, I., "Finite elements analysis of a small power eddy current brake," *MECHATRONIKA, 2012 15th International Symposium* , vol., no., pp.1,5, 5-7 Dec. 2012

[33] Schmitt, Ron. *Electromagnetics Explained: A Handbook for Wireless/RF, EMC, and High-speed Electronics*. Amsterdam: Newnes, 2002. Print.

[34] Magnetic Brake System Documentation <http://www.magbrakesystems.com/outline/MB_OUTLINE.pdf >

[35] NassaR, A.; NassaR, E., "An experimental study of ultrasonic vibration-assisted grinding," *Advances in Computational Tools for Engineering Applications (ACTEA), 2012 2nd International Conference on* , vol., no., pp.289,291, 12-15 Dec. 2012

[36] Induction Motor Documentation <http://www.grainger.com/Grainger/static/rc_nameptdatakey.html>

[37] "Service Factor." *Engineering Toolbox*. N.p., n.d. Web. <http://www.engineeringtoolbox.com/service-factor-d_735.html>.

[38] "JEDEC." *JEDEC*. N.p., n.d. Web. 11 Nov. 2013. <http://www.jedec.org/>.

[39] Siegel, Robert, and John R. Howell. *Thermal Radiation Heat Transfer*. Washington: Hemisphere Pub., 1981. Print.

[40] C.A. Balaras, A.A. Argiriou, Infrared thermography for building diagnostics, Energy and Buildings, Volume 34, Issue 2, February 2002, Pages 171-183

[41] Bo Chen, Jeffrey Oliver, Soumak Dutta, Grady H. Rylander III, Sharon L. Thomsen, and Ashley J. Welch, "Corneal minimal visible lesion thresholds for 2.0 μm laser radiation," J. Opt. Soc. Am. A 24, 3080-3088 (2007)

[42] Ho, H.-N.; Jones, L.A., "Infrared Thermal Measurement System for Evaluating Model-Based Thermal Displays," *EuroHaptics Conference, 2007 and Symposium on Haptic Interfaces for Virtual Environment and Teleoperator Systems. World Haptics 2007. Second Joint* , vol., no., pp.157,163, 22-24 March 2007

[43] Ball, M., and H. Pinkerton (2006), Factors affecting the accuracy of thermal imaging cameras in volcanology, J. Geophys.

[44] "Real Time Emissivity Measurement for Infrared Temperature Measurement." *Pyrometer.com*. N.p., n.d. Web. <http://www.pyrometer.com/pyro_technology.html>.

[45] Clausing, L. Terry. "Emissivity: Understand the Difference between Apparent, Actual IR Temps." *Reliable Plant*. Fluke Corporation, n.d. Web. <http://www.reliableplant.com/Read/14134/emissivity-underst-difference-between-apparent,-actual-ir-temps>.

[46] Nelson, Wayne. *Accelerated Testing: Statistical Models, Test Plans, and Data Analysis*. New York U.a.: Wiley, 1990. Print.

[47] Caruso, H.; Dasgupta, A., "A fundamental overview of accelerated-testing analytic models," *Reliability and Maintainability Symposium, 1998. Proceedings., Annual* , vol., no., pp.389,393, 19-22 Jan 1998

[48] Hu, J. M.; Barker, D.B.; Dasgupta, A.; Arora, A.K., "Role of failure-mechanism identification in accelerated testing," *Reliability and Maintainability Symposium, 1992. Proceedings., Annual* , vol., no., pp.181,188, 21-23 Jan 1992

[49] Engelmaier, W. (1983) "Fatigue Life Of Leadless Chip Carriers Solder Joints During Power Cycling", *IEEE Trans. CHMT*, Vol. CHMT-6, pp. 232-237.

[50] Engelmaier, W. (1993). "Generic Reliability Figures of Merit Design Tools for Surface Mount Solder Attachments, *IEEE Trans. CHMT*, Vol 16, No. 1., pp. 103-112.

[51] Technical Note, CalcePWA Documentation, 1st Order thermal Fatigue Model for Leadless Packages, "calcePWA_1st_tf_ll.doc"

[52] Gully, A. M., "Failure mechanisms in film-based power capacitors," *Dielectric Materials, Measurements and Applications, Seventh International Conference on (Conf. Publ. No. 430)* , vol., no., pp.358,363, 23-26 Sep 1996

[53] Joon Yeob Lee; Tae Kyung Hwang; Jin-young Kim; Min Yoo; Eun Sook Sohn; Ji-Young Chung; Dreiza, M., "Study on the Board Level Reliability Test of Package on Package (PoP) with 2nd Level Underfill," *Electronic Components and Technology Conference, 2007. ECTC '07. Proceedings. 57th* , vol., no., pp.1905,1910, May 29 2007-June 1 2007

[54] Kral, J., and E. K. Matthews. "Pyrolaser & Pyrofiber Infrared Temperature Measurement With Automatic Emissivity Correction." *Pyrometer.com*. N.p., n.d. Web. <http://www.pyrometer.com/paper0596.htm>.

[55] "Solving the Emissivity Problem in Real World Infrared Thermometer Temperature Measurements." *Pyrometer.com*. N.p., n.d. Web. <http://www.pyrometer.com/Tech/emissivity_technology.html>.